SEARCH FOR COLORFUL QUANTUM BLACK HOLES DECAYING TO AN ELECTRON-JET FINAL STATE WITH THE ATLAS EXPERIMENT

by

ANDREAS D. W. REINSCH

A DISSERTATION

Presented to the Department of Physics
and the Graduate School of the University of Oregon
in partial fulfillment of the requirements
for the degree of
Doctor of Philosophy

June 2012

DISSERTATION APPROVAL PAGE

Student: Andreas D. W. Reinsch

Title: Search for Colorful Quantum Black Holes Decaying to an Electron-Jet Final State with the ATLAS Experiment

This dissertation has been accepted and approved in partial fulfillment of the requirements for the Doctor of Philosophy degree in the Department of Physics by:

Dr. Eric Torrence	Chair
Dr. David Strom	Advisor
Dr. Stephen Hsu	Member
Dr. Jens Nöckel	Member
Dr. Michael Kellman	Outside Member

and

Kimberly Andrews Espy	Vice President for Research & Innovation/ Dean of the Graduate School

Original approval signatures are on file with the University of Oregon Graduate School.

Degree awarded June 2012

DISSERTATION ABSTRACT

Andreas D. W. Reinsch

Doctor of Philosophy

Department of Physics

June 2012

Title: Search for Colorful Quantum Black Holes Decaying to an Electron-Jet Final State with the ATLAS Experiment

A search for quantum black holes with color charge decaying to one electron and one quark has been performed using data collected by the ATLAS Experiment at the Large Hadron Collider corresponding to $2.29\,\mathrm{fb}^{-1}$. No excess over the expected Standard Model interactions has been observed. Limits are set on the production cross section for events with one electron and one jet resulting from new physical phenomena. Models with a combined invariant mass of the electron and jet larger than or equal to 2.5 TeV and a cross section above 2.6 fb are excluded at the 95% confidence level. This allows the exclusion of a significant part of the parameter space of quantum black hole models.

CURRICULUM VITAE

NAME OF AUTHOR: Andreas D. W. Reinsch

GRADUATE AND UNDERGRADUATE SCHOOLS ATTENDED:

University of Oregon, Eugene, Oregon
Fernuniversität Hagen, Hagen, Germany
Ruprecht-Karls-Universität Heidelberg, Heidelberg, Germany

DEGREES AWARDED:

Doctor of Philosophy, Physics, 2012, University of Oregon
Vordiplom, Betriebswirtschaftslehre, 2006, Fernuniversität Hagen
Master of Science, Physics, 2005, University of Oregon
Vordiplom, Physik, 2004, Ruprecht-Karls-Universität Heidelberg

AREAS OF SPECIAL INTEREST:

Experimental Searches for Physics Beyond the Standard Model
Trigger Algorithms in High Energy Physics Experiments
Aggregate Market Valuations of Stocks, Bonds and Real Estate and Long-Term Investment Strategies

PROFESSIONAL EXPERIENCE:

Graduate Research Assistant,
University of Oregon, 2007 – 2012
Graduate Teaching Fellow,
University of Oregon, 2005 – 2007

PUBLICATIONS:

G. Aad et al. (The ATLAS Collaboration), Search for strong gravity signatures in same-sign dimuon final states using the ATLAS detector at the LHC, *Phys. Lett. B* **709**, 322 (2012).

G. Aad et al. (The ATLAS Collaboration), Observation of $W \rightarrow \tau\nu_\tau$ Decays with the ATLAS Experiment, Tech. Rep. ATLAS-CONF-2010-097, CERN, Geneva (2010).

A. Reinsch for the ATLAS Collaboration, The Tau Trigger at the ATLAS Experiment, *Proceedings of Science, EPS-HEP 2009* (Scuola Int. Sup. Studi Avan., Trieste, Italy, 2009), pp. 409.

ACKNOWLEDGEMENTS

First of all, I would like to thank my adviser Prof. David Strom for his support and guidance during my years of research leading to this dissertation. Despite having many responsibilities at the ATLAS Experiment, he always found time to meet and discuss all issues in his positive and friendly manner. With his quick understanding of my questions, problems and ideas, he was able to offer thoughtful advice and solutions to my problems.

Next, I would like to thank Dr. Mansoora Shamim. Sharing the same office with me at CERN, she was always available for a quick chat or a profound discussion about the details of problems in experimental High Energy Physics. With her dedication to detail and accuracy, she helped me improving my own work habits considerably. I also very much enjoyed her occasional dinner invitation, where I was able to enjoy her cooking of Pakistani dishes.

I'm also very thankful to Dr. Olya Igonkina. I arrived at CERN during her post-doctoral research for the University of Oregon. During my first months at CERN, she helped me not only to get acquainted with life at CERN, but to extend my knowledge of the tau trigger and improve my programming skills notably. With her help and support I was able to make quick contributions to the ATLAS Tau Trigger group.

I would like to thank the entire high energy physics group at the University of Oregon for the open, friendly and supportive atmosphere. The feedback I received for my presentations in our weekly group meetings helped me to improve the analysis described in this dissertation significantly.

I would also like to thank all other collaborators with which I had the pleasure to work, including Hugo Beauchemin, Massimiliano Bellomo, Maarten Boonekamp, Sourabh Dube, Ian Hinchliffe, Brian Martin, Jason Nielson, Matthias Schott, Peter Steinbach and Alessandro Tricoli.

During my four years of research at CERN, I have also received great mental support by my girlfriend Eugénie Stebler, with whom I was able to share all my thoughts and problems. I am grateful for all the patience she had and the sacrifice she made during the time I wrote this dissertation. I'm especially thankful to my parents, Elisabeth Schneider-Reinsch and Heinz Reinsch, for the help and support they gave me in so many ways. They always encouraged and motivated me to do what I wanted to do most. I'm grateful to them for giving me the opportunity and the means to follow my interests for more than 30 years. I would also like to mention my sister Christine Reinsch, who gave birth to a healthy boy named Eliah Reinsch during my stay at CERN. This was a particular happy moment in my life.

Last, but not least, I would like to thank Jörg Mechnich, Elizabeth Ptacek, Peter Radloff, Mary Robinson and Jacob Siercy with whom I spend many good moments.

TABLE OF CONTENTS

Chapter Page

Chapter Page

LIST OF FIGURES

Figure Page

Figure Page

LIST OF TABLES

Table Page

Table Page

CHAPTER I

INTRODUCTION

The search for the building blocks of the observable matter in the universe has been of interest to philosophers and scientists for centuries. The first modern idea has been the proposal of the existence of fundamental constituents (atoms) which dates back to at least the 6th century BCE. However, the systematic study of fundamental particles began only with the experimental confirmation of the atomic theory in the 19th century. The development of the Standard Model of Particle Physics (SM) [1] in the 1970s has been the latest major step toward an understanding of the behavior of subatomic particles. The discovery of the bottom quark in 1977 [2], the top quark in 1995 [3] [4] and the tau neutrino in 2000 [5] as predicted by the SM, has added further support to the model. However, some inconsistencies with observations have been identified, resulting in the need for an extended model. In addition some theoretical arguments, including the Hierarchy Problem, have been raised disfavoring the SM as a final theory.

In order to further improve the understanding of fundamental particles and their interactions, the Large Hadron Collider and its four experiments [6] have been developed and built at the European Organization for Nuclear Research (CERN).

With a significant higher center-of-mass energy than the Tevatron [7], the LHC is opening up a new energy regime for studying the behavior of known SM particles and the search of new phenomena. Since the start of collisions in 2010, the LHC and its experiments have produced a large number of new insights, including the search for the Higgs-boson and new phenomena at the TeV energy scale, many of which have been excluded over a large parameter space.

At the ATLAS experiment, several searches for black holes and other new phenomena have been performed. However, most of the searches have concentrated on signatures with large multiplicities (as predicted by decays of semi-classical black holes) or on generic searches for new phenomena in the di-jet or di-lepton invariant mass spectrum. The analysis described here will perform a search for new phenomena in events with one high energetic electron and one high energetic jet. The signature is predicted by several theories including theories with extra dimensions. Corresponding to $2.29\,\mathrm{fb}^{-1}$, the analyzed data has been collected by the ATLAS Experiment between March and August 2011 in proton-proton collisions with a center-of-mass energy of 7 TeV. Signal-like events are selected using multiple variables. The number of observed and expected events with a combined electron and jet invariant mass above a set of thresholds have been recorded. Each threshold is optimized for models of black holes with a given minimum mass. The background is divided into contributions from events dominated by the strong interaction (QCD events) and events not dominated by the strong interaction (non-QCD events). The

QCD background is estimated using a data driven technique while the non-QCD background is calculated using Monte Carlo simulated events normalized to data in a signal-free control region. No excess over SM expectations is observed and upper limits are set on the cross section times branching fraction of events originating from new phenomena.

In this first chapter, the system of units is defined and selected definitions of quantities used in the analysis are given. In the second chapter, the theory of the SM and the models of extra dimensions are introduced. The CERN Large Hadron Collider and the ATLAS Experiment are described in chapter three and four. In chapter five, the reconstruction and identification algorithms developed by the ATLAS experiment are presented. The Monte Carlo simulated samples and their characteristics are described in chapter six. In chapter seven, all objects used in the search for quantum black holes are defined and the selection criteria for various regions are explained. The signal acceptance calculation is shown in chapter eight, while the technique to estimate the background is described in chapter nine. The estimate of the background at very high invariant mass is shown in chapter ten. Using the systematic uncertainties described in chapter eleven, the observed and expected limits together with the exclusion region of quantum black hole models are derived in chapter twelve. The findings are summarized and the dissertation is concluded in chapter thirteen.

System of Units

In this analysis, energies are given in units of electronvolt (eV). 1 eV is defined to be the energy gained by an electron moving across an electric potential of 1 Volt. 1 eV is equal to 1.6×10^{-19} J. The fundamental constants, the speed of light c and the reduced Planck constant $\hbar$, are assumed to be unity. Hence, related quantities as momentum, mass, distances and lengths can be expressed in eV and eV^{-1}. All electric charges are given in units of the elementary charge e.

The integrated luminosity is reported in units of barns (b). One barn is defined in SI units to be $100\,\mathrm{fm}^2$ which is equal to $10^{-28}\,\mathrm{m}^2$ or about $2.6 \times 10^3\,\mathrm{GeV}^{-2}$.

CHAPTER II

THEORETICAL BACKGROUND

The Standard Model

The Standard Model of Particle Physics (SM) is a collection of theories, which have been developed to describe the properties of fundamental particles and their interactions. All theories are based on quantum field theory [8], which describes the mechanics of objects of atomic and sub-atomic size and at speeds close to the speed of light [1]. According to quantum field theory, the transition rate of a physical process (like decay rates and cross sections) is given by the product of the amplitude (matrix element) squared and its available phase-space (density of final states). The amplitude of a process contains all dynamical information and can be calculated using pictorial presentations developed by Richard Feynman (Feynman diagram) [9] and the corresponding calculation rules (Feynman rules). A Feynman diagram is a representation of one possible path of a physical process. The sum of all Feynman diagrams with the same incoming and outgoing particles is the amplitude of the corresponding physical process. Since each interaction vertex in

the Feynman diagram introduces an additional factor (coupling constant), the final result can be approximated by only considering diagrams with small number of vertices, if the coupling constant is much smaller than one. The phase-space is purely kinematic and depends on the mass, energy and momentum of the particles involved. The allowed range of kinematic variables of the outcoming particles is limited by restrictions like momentum and energy conservation. The larger the phase-space, the higher the transition rate of a given process.

Elementary Particles

Elementary particles are the point-like constituents of the physical world with no substructure [10] to which several physical properties such as mass and electric charge can be ascribed. There are three kind of elementary particles: leptons, quarks and mediator particles. Leptons and quarks naturally fall into three generations. First generation particles (up-quarks, down-quarks and electrons) make up the visible matter of the universe. The set of known elementary particles can be divided into fermions (leptons and quarks), having a half-integer spin, and bosons (the mediator particles) with an integer spin. According to the Pauli exclusion principle [11], two fermions are excluded from occupying the same quantum state. In addition to the three generations, all particles have a partner with the same properties, but with opposite electric charge and color charge (antiparticle). Quarks are the constituents of composite particles (hadrons) like protons and neutrons which form the atomic nucleus. They carry color charge

and therefore participate in the strong interaction. Since all naturally occurring particles are colorless due to color confinement [1], quarks can not be observed in isolation. Three quarks combine to constitute a baryon and one quark and one antiquark combine to a meson. Quarks take part in the electromagnetic interaction by carrying fractional electric charges (see table 2.1.).

generation	name	symbol	mass [MeV]	spin	electric charge	antiparticle
1st	up-quark	u	1.7 to 3.1	1/2	2/3	anti-up-quark ($\bar{u}$)
	down-quark	d	4.1 to 5.7	1/2	-1/3	anti down-quark ($\bar{d}$)
2nd	charm-quark	c	1.29×10^3	1/2	2/3	anti charm-quark ($\bar{c}$)
	strange-quark	s	80 to 130	1/2	-1/3	anti strange-quark ($\bar{s}$)
3rd	top-quark	t	1.73×10^5	1/2	2/3	anti top-quark ($\bar{t}$)
	bottom-quark	b	4.19×10^3	1/2	-1/3	anti bottom-quark ($\bar{b}$)

Table 2.1. Overview of quarks and their properties [12].

Leptons don't take part in the strong interaction, since they don't carry color charge. They can be subdivided into charged or electron-like leptons and neutral leptons or neutrinos. There are three generations of leptons with similar properties, but different masses: electronic leptons, muonic leptons and tauonic leptons (see table 2.2.).

generation	name	symbol	mass [MeV]	spin	elec. charge	antiparticle
1st	electron	e^-	0.51	1/2	-1	antielectron (e^+)
	electron neutrino	ν_e	$< 2 \times 10^{-6}$	1/2	0	electron antineutrino ($\bar{\nu}_e$)
2nd	muon	μ	106	1/2	-1	antimuon ($\bar{\mu}$)
	muon neutrino	ν_μ	$< 0.19 \times 10^{-6}$	1/2	0	muon antineutrino ($\bar{\nu}_\mu$)
3rd	tau	τ	1777	1/2	-1	antitau ($\bar{\tau}$)
	tau neutrino	ν_τ	$< 18.2 \times 10^{-6}$	1/2	0	tau antineutrino ($\bar{\nu}_\tau$)

Table 2.2. Overview of leptons and their properties [12].

In the SM, there are five types of elementary bosons: four types of gauge bosons

and the Higgs boson. Each gauge boson is the carrier of a fundamental force with which it can be associated (see table 2.3.). All gauge bosons have been observed in various experiments [12]. The Higgs boson is a new doublet of complex scalar fields, which gives mass to the W- and Z-boson. As of the writing of this dissertation, the Higgs boson has not been discovered, but there are indications to its existence observed both at the ATLAS and CMS experiment at the LHC [13] [14].

In the SM, there is a total of 4 different types of mediator bosons, the Higgs boson and 24 different fermions: 6 quarks and 6 leptons with their corresponding anti-particle each.

name	symbol	mass [GeV]	spin	elec. charge	lifetime [s]	corresponding force
photon	γ	0	1	0	stable	electromagnetic
gluon	g	0	1	0	stable	strong interaction
W-boson	W^+/W^-	80.4	1	+1/-1	$\sim 3 \times 10^{-25}$	weak interaction
Z-boson	Z	91.2	1	0	$\sim 3 \times 10^{-25}$	weak interaction
Higgs boson	H	unknown	0	0	unknown	-

Table 2.3. Overview of elementary bosons and their properties [12].

Fundamental Interactions

Four fundamental interactions have been observed in nature: electromagnetic, weak, strong and gravitational interactions. In the SM, they are modeled with the exchange of bosons (carrier particles). The relative strength of the four forces depends on the energy scale, but indicative values are give in table 2.4.

name	carrier particle	relative strength
Strong	gluon	10
Electromagnetic	photon	10^{-2}
Weak	W-boson/Z-boson	10^{-13}
Gravity	graviton	10^{-42}

Table 2.4. Overview of fundamental interactions and their relative strength. The values for the relative strength are indicative, since the strength is energy dependent [1].

Quantum Electrodynamics

The theory of quantum electrodynamics (QED) describes the interaction between fermions that carry electric charge with the photon as carrier particle. The only allowed interaction is between two fermions of the same type and a photon (see figure 2.1. for the Feynman diagram). All more complex electromagnetic phenomena can be reduced to this process. With a photon mass of zero, the range of the interaction is not restricted. The coupling constant depends weakly on the momentum transfer of the interaction. At zero momentum transfer, it is equal to the fine structure constant $\alpha = \frac{e^2}{\hbar c} \approx \frac{1}{137}$. Due to the small value of the coupling constant, most electromagnetic processes can be approximated by the sum of Feynman diagrams with a small number of vertices only. QED is thought to be among the most accurate physical theories yet invented and confirmed by a large range of observations. This includes the measurement of the hydrogen $1s - 2s$ transition, which has been determined with a relative uncertainty of 10^{-14} [15].

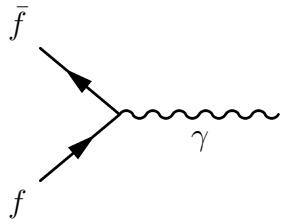

Figure 2.1. Fundamental electrodynamic vertex.

Weak Interaction

The weak interaction between all quarks and all leptons is mediated by the neutral Z-boson and the positively and negatively charged W-bosons. All three carrier particles are massive, limiting the range of the weak interaction. The fundamental vertex in neutral weak interactions connects two fermions of the same type and the Z-boson (see figure 2.2.(a)). Hence, there is no lowest order flavor changing neutral weak interaction. The charged weak interaction is the only interaction to change the flavor of particles. For leptons the vertex connects a lepton, a neutrino of the same flavor and a W-boson (figure 2.2.(b)). For quarks, the charged current couples to two different quarks of the same generation (figure 2.2.(c)). However, these are not the flavor eigenstates described in table 2.1. The W-boson couples the pairs (u, d'), (c, s') and (t, b'). The Cabbibo-Kobayashi-Maskawa matrix gives the relationship between the quark states of negative charge that take part in the weak interaction by exchange of a W-boson and the quark

flavor eigenstates:

$$\begin{pmatrix} |d'\rangle \\ |s'\rangle \\ |b'\rangle \end{pmatrix} = \begin{pmatrix} V_{ud} & V_{us} & V_{ub} \\ V_{cd} & V_{cs} & V_{cb} \\ V_{td} & V_{ts} & V_{tb} \end{pmatrix} \begin{pmatrix} |d\rangle \\ |s\rangle \\ |b\rangle \end{pmatrix} \tag{II.1}$$

By definition, the Cabbibo-Kobayashi-Maskawa matrix is unitary and very close to the identity matrix. However, experiments show that there are non-zero entries outside the main diagonal [12]:

$$\begin{pmatrix} V_{ud} & V_{us} & V_{ub} \\ V_{cd} & V_{cs} & V_{cb} \\ V_{td} & V_{ts} & V_{tb} \end{pmatrix} = \begin{pmatrix} 0.97428 \pm 0.00015 & 0.2253 \pm 0.0007 & 0.00347^{+0.00016}_{-0.00012} \\ 0.2252 \pm 0.0007 & 0.97345^{+0.00015}_{-0.00016} & 0.0410^{+0.0011}_{-0.0007} \\ 0.00862^{+0.00026}_{-0.00020} & 0.0403^{+0.0011}_{-0.0007} & 0.999152^{+0.000030}_{-0.000045} \end{pmatrix} \tag{II.2}$$

In addition to the described couplings above, the weak interaction also includes direct vertices between W-bosons and Z-bosons as long as electric charge is conserved. The W-boson can also couple to photons.

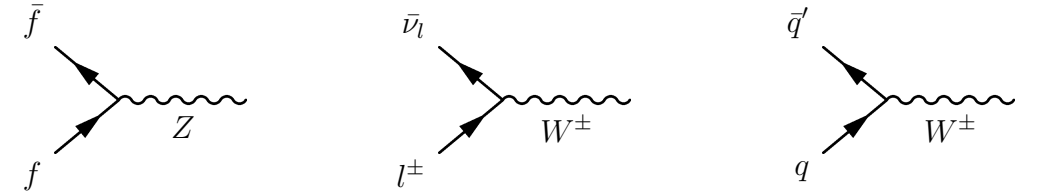

(a) neutral weak interaction

(b) charged weak interaction (leptons)

(c) charged weak interaction (quarks)

Figure 2.2. Fundamental vertices of the weak interaction. The vertices are shown for the neutral and charged interaction. For the charged interaction, the diagrams are separated for leptons and quarks.

One of the important decays in nature due to weak interaction is the beta decay of a neutron ($n \rightarrow p + e^- + \bar{\mu}_e$). A down quark inside the neutron decays to a negatively charged W-boson and an up quark. The up quark combines with the

other up quark and the second down quark of the neutron to build a proton, while the W-boson decays to an electron and an electron neutrino (see figure 2.3.).

The weak and the electromagnetic interactions can both be explained by the same fundamental interaction. They can be combined into a common electroweak (EW) force (EW unification).

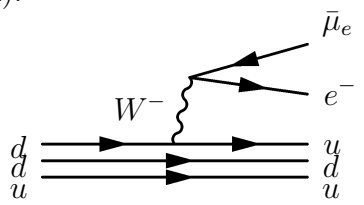

Figure 2.3. Beta decay of a neutron.

Strong Interaction

Quantum Chromodynamics describes the strong interactions between quarks and gluons, mediated by the exchange of gluons. The force is responsible for holding the quarks together inside the hadrons (including the proton and neutron). The allowed vertex connects two quarks of the same type and one gluon (see figure 2.4.). In addition, gluon fusion to one gluon and gluon fusion to two gluons is allowed. There exist three kinds of color (colloquially called red, green and blue), which are conserved in the strong interaction. All quarks carry one color charge (color triplet), while gluons are bicolored with one positive and one negative unit of color (anticolor), combining to a color octet of gluons. The coupling constant α_s for the strong interaction depends on the distance between the two

interaction particles. However, in contrast to the electromagnetic interaction, the coupling increases for larger distances (or equivalent lower energies). This results in two effects: First, for quarks and gluons inside a proton the coupling is small and they move approximately freely (asymptotic freedom). Second, for small energies, the coupling constant is large and the calculation of amplitudes can not be approximated by only considering Feynman diagrams with a small number of vertices. Hence, the calculation of matrix elements at low energy and therefore the simulation of events with soft jets carry large uncertainties. For high p_T jets, the coupling constant becomes smaller and allows the calculation of amplitudes with much smaller uncertainties.

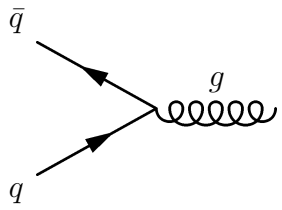

Figure 2.4. Fundamental vertex of the strong interaction.

Other Aspects of the Standard Model

One consequence of the interaction rules is that several properties are conserved. Energy, momentum, angular momentum, electric charge and color charge are conserved in all type of interactions. However, the model allows for virtual particles that are off-shell and carry a different mass than real particles. Virtual particles are only allowed internally in interactions, but can not be observed directly. Another constant is the number of quarks minus antiquarks. Hence,

assigning a baryon number of +1 to all baryons and -1 to all antibaryons, the baryon number is conserved in any interaction. In addition, the number of leptons minus antileptons (lepton number) is constant for each individual flavor and therefore for the total number of leptons. Quark flavor is conserved in all interactions except for the charged weak interaction, where the states coupling to the W-boson are not flavor eigenstates, which allows the change of quark flavor.

In the SM, all particles decay to particles with lower mass if allowed by any of the fundamental interactions and not kinematically forbidden. Due to different coupling strength for different interactions, the average lifetime for particles that decay to lower particles depends on the allowed interaction. Table 2.5. shows typical lifetimes for the different interactions.

interaction type of decay	typical lifetime range
strong interaction	$\sim 10^{-23}\,\mathrm{s}$
electromagnetic interaction	$\sim 10^{-16}\,\mathrm{s}$
weak interaction	$10^{-13}\,\mathrm{s}$ - $15\,\mathrm{min}$

Table 2.5. Typical lifetimes of particles according to decay type [1].

Factorization of Proton-Proton Interactions

The cross section of a physical process involving the interaction of two protons can be expressed as the product of a probability function and a cross section of a hard scattering [16]:

$$\sigma_{pp} = \sum_{i,j} \sigma_{ij} \cdot f_{i/p}(x_1, Q^2) \cdot f_{j/p}(x_2, Q^2) \tag{II.3}$$

where σ_{pp} is the cross section of a process with two initial protons, σ_{ij} the hard scattering including two hadrons of type i and j (gluons or quarks) and Q is the momentum transfer of the hard scattering process. The parton distribution function (PDF) $f_{i/p}(x, Q^2)$ describes the probability to find a parton of type i with momentum $x \cdot \vec{P}$ in a proton of momentum $\vec{P}$. The hard scattering cross section is perturbative and can formally be calculated for any given process, while the PDF is process independent and non-perturbative and needs to be extracted from data. Hence, most new physical phenomena are expected to change the hard scattering cross section only.

PDFs are derived from a global analysis of a large number of physical processes meassured in different experiments. Among the processes are deep inelastic scattering, jet production and lepton pair production. A fit to the cross sections is found by minimizing a likelihood function with respect to a number of fitting parameters. One example of a PDF (CTEQ6.6) used throughout this analysis is calculated by the Coordinated Theoretical Experimental Study of QCD (CTEQ) [17] [18], which considered 2714 experimental data points in order to retrieve about 30 theoretical parameters. For each parameter that is retrieved, a confidence interval is obtained by allowing an increase of the goodness of the fit χ^2 from its minimal value. This results in one central PDF and 44 eigenvector PDFs which can be used to calculate the uncertainty of the cross section calculation.

Problems of the Standard Model

The SM has been very successful in explaining various experimental results. However, there are several weak points where it is either seen as add-hoc or where it is in disagreement with observation. Hence, the SM can not be the final theory and can only be considered a good approximation.

One of the problems of the SM is that the gravitational force is not incorporated into the model. At present, no model has been proposed which describes the behavior of quantum gravity and which has been confirmed by observation. There is currently no way of describing the theory of general relativity [19] [20] in terms of quantum field theory [8]. In addition, gravitational effects at the particle level are hard to observe in a controlled environment due to its weak couplings compared to other fundamental interactions.

There is a large difference between the relative strength of the weak force in the SM (10^{-13}) and the gravitational force (10^{-42}) at low energies. Going to higher energies, the relative strength of gravity increases. Quantum effects become important for objects of mass m with a size at the order of their reduced Compton wavelength $\lambda_C/2\pi = \hbar/m$, where $\hbar$ is the reduced Planck constant. The Schwarzschild radius of a black hole [20] with mass m is $r_S = 2 \cdot G \cdot m$, G being the gravitational constant. The gravitational force becomes strong, when the reduced Compton wavelength of an object is of comparable size than its Schwarzschild

radius: $r_S \sim \lambda_C/2\pi$. This energy scale is called the Planck mass m_{Pl}:

$$m_{Pl} = \sqrt{\frac{\hbar}{2G}} \sim 10^{19}\,\text{GeV} \tag{II.4}$$

Hence, the Planck mass is 10^{17} times larger than the weak scale of $\sim 10^2\,\text{GeV}$ and is currently far out of reach for any controlled experiment.

Renormalization [21] is a method used in Quantum Field Theory to redefine physical quantities when calculating matrix elements in order to absorb divergent terms. Without renormalization, the calculations often give non-finite matrix elements. Assuming that no new physical phenomena exists between the weak scale and the Planck scale, the cut-off for the renormalization of the Higgs mass is the Planck scale. Hence, following its renormalization, the physical Higgs mass m_H takes the following form:

$$m_H^2 = m_{H_0}^2 + \frac{kg^2\Lambda^2}{16\pi^2} \tag{II.5}$$

where m_{H_0} is the bare mass of the Higgs boson, g the electromagnetic coupling, k a constant at of $\mathcal{O}(1)$ and Λ the cut-off scale for new physics [12].

The physical Higgs mass parameter determines the Higgs field's potential energy and strength, which is related to the mass of the W-boson and the Z-boson. Since their masses are well measured, the physical Higgs mass is required to be at the order of 250 GeV. If Λ is much larger than the electroweak scale, the two unrelated contributions to the physical Higgs mass are required to cancel in order to arrive at the much lower Higgs mass (Hierarchy Problem). Since there is no mechanism in

the SM that explains the cancellation, an unnatural fine-tuning of the parameters is required. Many theories have been proposed to avoid the fine-tuning problem, including theories of super-symmetry [22] and theories of extra dimensions [23].

Consisting of the particles described by the SM, the visible part of the universe (stars, planets, dust, etc.) only accounts for 4% of its energy. The remaining 96% of the energy is in a form that does not emit electromagnetic radiation. This part can be subdivided into dark matter, contributing $\sim 23\%$ to the total energy, and dark energy, which consists of $\sim 73\%$ of the universe's energy [24]. Dark matter is composed of massive particles of unknown type. A small part of the dark matter is expected to be baryonic, but emitting little or no electromagnetic radiation and therefore remaining undetected. However, the overwhelming contribution to dark matter is non-baryonic [25], including contributions from neutrinos and possible hypothetical particles. In order to explain the non-baryonic dark matter, many particles have been proposed, including the stable lightest supersymmetric particle [26]. However, none of the candidates has been observed at controlled collider experiments [27]. Currently, the class of weakly interacting massive particles (WIMPs) is considered to be the most promising candidate of dark matter [28]. As a result, most of the matter in the universe might not be included in the SM. The dark energy is homogeneously distributed througout the universe. It has mainly no local gravitational effect, but causes the acceleration of the

expansion of the universe. This can be observed via an increase of the rate of expansion described by Hubble's law [29].

Finally, the SM has a total of 18 numerical parameters which are arbitrary and not explained by theory [30]. However, different values of these variables could change the observed universe significantly. Currently, the determination of these constants is left to experimental observation. An extended version of the SM should preferably be able to explain the value of these variables.

Models of Extra Dimensions

The Hierarchy Problem of the SM originates in the huge discrepancy between the electroweak scale and the Planck scale. One of the assumptions for the existence of the Hierarchy Problem is that Newton's law of gravitation [31] is unchanged over ~ 28 orders of magnitude. However, due to the weakness of gravity, its effects have only been measured at distances much larger than the Planck length of $\sim 10^{-33}$ cm. The smallest upper limit from direct measurement of the inverse-square law of the gravitational force has been set at a distance of $56\,\mu$m [32]. Hence, a Planck length much larger than 10^{-33} cm and correspondingly a much smaller Planck mass can not be ruled out. Several mechanisms to reduce the Planck scale have been proposed. Among them is the existence of extra dimensions [33] [34] or a large number of hidden particles [35]. Two fundamental types of models with extra dimensions

have been proposed. In the model by Arkani-Hamed, Dimopoulos and Dvali (ADD model) [33, 36, 37], the known four dimensional spacetime is embedded in a (4+n) dimensional space with n compact dimensions (ADD-type extra dimensions). The second type of model has been proposed by Randall and Sundrum (RS model) [34]. It assumes the existence of one warped extra dimension in addition of the known four dimensional spacetime (RS-type extra dimensions).

ADD-type Extra Dimensions

In the ADD model, the four known dimensions (brane) are embedded in a higher dimensional space with (4+n) dimensions. The n extra dimensions (bulk) are spatial and compact of size R. Since at weak scale distances no deviation from the SM has been observed, the SM particles are assumed to be confined to the brane. Only gravity, which has not been tested at the weak scale, is allowed to enter the bulk.

The gravitational force in four dimensions between two masses m_1 and m_2 at a distance r in the four-dimensional spacetime can be derived from Gauss law [38], using the relationship between Planck mass M_{Pl} and the gravitational constant G (see equation II.4):

$$V(r) \sim \frac{m_1 m_2}{M_{Pl(4)}^2} \frac{1}{r^2} \qquad \text{for all } r > 0 \tag{II.6}$$

In the ADD-model, the potential is modified [33]:

$$V(r) \sim \frac{m_1 m_2}{M_{Pl(4+n)}^{n+2}} \frac{1}{r^{n+2}} \qquad \text{for } r \ll R \tag{II.7}$$

$$V(r) \sim \frac{m_1 m_2}{M_{Pl(4+n)}^{n+2} R^n} \frac{1}{r^2} \qquad \text{for } r \gg R \tag{II.8}$$

For distances smaller than the size of the extra dimensions R, the gravitational flux penetrate the additional dimensions and the force decreases with $1/r^{n+2}$. For larger distance, the flux can only penetrate the extra dimensions up to their size R, so that Newton's inverse-square law is recovered. The effective four dimensional Planck mass $M_{Pl(4)}$ is related to the (4+n) dimensional fundamental Planck mass $M_{Pl(4+n)}$[1] in the following way:

$$M_{Pl(4)}^2 \sim M_{Pl(4+n)}^{2+n} R^n \tag{II.9}$$

Using this equation, it is possible to estimate the size R of the extra dimensions for which the (4+n) dimensional Planck mass is reduced to the electroweak scale ($M_{Pl(4+n)} \sim m_{EW}$):

$$R \sim 10^{\frac{30}{n}-17}\text{cm} \, (\frac{1\,\text{TeV}}{m_{\text{EW}}})^{1+\frac{2}{n}} \tag{II.10}$$

Table 2.6. shows the estimated required size of the extra dimensions as a function of the total number of extra dimensions. The models with one or two extra dimensions have certainly been disproven. However, the required size of the extra dimensions for more than two additional dimensions is much smaller than the resolution of gravitational experiments and can therefore not be ruled out.

However, there are a number of other analyses with indirect constraints on the Planck mass. Table 2.7. gives an overview over selected experiments and

[1] In the literature, the fundamental (or reduced) (4+n)-dimensional Planck mass is also noted as M_D. For simplicity, the subscript (4+n) will be dropped and the fundamental Planck mass will be prescribed as M_{Pl}

number n of extra dimensions	size R (indicative) [m]
1	2×10^{12}
2	6×10^{-4}
3	1×10^{-8}
4	4×10^{-11}
5	1×10^{-12}
6	2×10^{-13}
7	3×10^{-14}
8	1×10^{-14}
9	4×10^{-15}

Table 2.6. Size requirement of ADD-type extra dimensions which reduces the fundamental Planck scale to the electroweak scale as a function of the number n of extra dimensions.

their limits. As one can see, there are strong indications that models with a fundamental Planck mass of less than 1 TeV have been excluded for all number of dimensions. However, for Planck masses above 1 TeV and models with a high number of additional dimensions, the constraints are much weaker.

Experiment/Analysis	Limit on M_{Pl} $(n = 2)$	Limit on M_{Pl} $(n \geq 3)$
Overclosure of universe [39]	8 TeV (n=2)	
Supernovae cooling rate [40–43]	30 TeV (n=2)	2.5 TeV (n=3)
Non-thermal production of KK modes [44]	35 TeV (n=2)	3 TeV (n=6)
Diffuse gamma-ray background [39, 45, 46]	110 TeV (n=2)	5 TeV (n=3)
Thermal production of KK modes [46]	167 TeV (n=2)	1.5 TeV (n=5)
Neutron star cone halo [47]	500 TeV (n=2)	30 TeV (n=3)
Time delay coming from photons from GRB's [48]	620 GeV (n=2)	
Neutron star surface temperature [47]	700 TeV (n=2)	0.2 TeV (n=6)
BH absence in neutrino cosmic ray showers [49]		1-1.4 TeV (n≥5)

Table 2.7. Constraints on the size of ADD-type dimensions from different experiments for a selected number of extra dimensions [50].

RS-type Extra Dimensions

In a model proposed by Randall and Sundrum, the four dimensional brane is

embedded in a five dimensional spacetime [34]. The new additional dimension (RS-type) is denoted by the coordinate ϕ with $0 \leq \phi \leq \pi$. All SM particles are constraint to a three dimensional visible plane, located at $\phi = \pi$ and to the additional hidden brane, located at $\phi = 0$. This results in a warped extra dimensions with the following metric:

$$ds^2 = e^{-2kr_c|\phi|}\eta_{\mu\nu}dx^\mu dx^\nu + r_c^2 d\phi^2 \tag{II.11}$$

where k is at the order of the Planck scale and x^μ are coordinates of the four dimensional spacetime. r_c is a parameter which sets the size of the interval of ϕ, typically assumed to be small, but larger than $1/k$.

Any mass parameter m_0 on the visible mass corresponds to a physical mass m of

$$m = e^{-kr_c\pi}m_0 \tag{II.12}$$

If the warp factor is at the order of 10^{-15}, the physical Planck mass can be at the order of 1 TeV, while the fundamental mass parameters are at the order of the Planck mass at 10^{19} GeV. Since the warp factor is exponential, this does not require large hierarchies between fundamental parameters.

The advantage of the model is that no fine-tuning between the inverse of the size of the extra dimensions and the electroweak scale is needed as in the ADD model. In addition, many of the constraints shown in table 2.7. don't apply, so lower fundamental Planck masses are possible.

Model of a Large Hidden Sector

As another explanation for a lower Planck mass, a model with a large hidden sector has been proposed by Calmet, Hsu and Reeb [35]. It does not require the existence of additional dimensions, but assumes a large number of new particles which couple only gravitationally with SM particles. This leads to a running of Newtons constant, which results in a Planck mass that decreases with increasing energy. For 10^{32} hidden particles (scalars or fermions), the Planck mass at an energy of 1 TeV is $\sim$ 1 TeV, which would be observable at the LHC. This model has not been used explicitly in this analysis.

Semi-Classical Black Holes

In all three models presented above, the fundamental Planck mass M_{Pl} might be as low as 1 TeV, which is an energy scale accessible by the CERN Large Hadron Collider. This could lead to the production of black holes (BH) [51]. A black hole is one of the implications of Einstein's field equations [20]. It describes a region of spacetime in which there is no point that is connected with infinity via a timelike path. The event horizon is the separation between these points and the points that are connected with infinity via a timelike path. Hence, no particle inside a black hole can escape it.

At the fundamental Planck scale, by definition gravity becomes comparable in

strength to the four other interactions. A theory of quantum gravity is required to explain the behavior of BHs at this scale. Unfortunately, no such theory is available at the time of writing. However, it is possible to make predictions about the behavior of BHs with masses much larger than the fundamental Planck scale (semi-classical black holes). In the following, ADD-type extra dimensions are assumed, but similar results are obtained from other proposed models.

Semi-Classical Black Hole Formation

The most general assumption is that BH could be formed if the following two requirements are met:

- The energy of the colliding partons E is larger than the fundamental Planck mass ($E > M_{Pl}$).
- Following the Hoop Conjecture [52], the impact parameter b of the colliding partons is required to be smaller than the Schwarzschild radius r_H of the BH with energy E of the colliding partons ($b < r_H(E)$).

In n dimensions, the Schwarzschild radius is given by [50]:

$$r_H \sim \frac{1}{M_{Pl}}\left(\frac{M_{BH}}{M_{Pl}}\right)^{\frac{1}{n+1}} \tag{II.13}$$

From the geometrical assumption that $b < r_H(E)$ follows that the cross section of BH production from two partons is

$$\sigma_{ij\to BH} \sim \pi r_H^2(E) \sim \frac{\pi}{M_{Pl}^2}\left(\frac{E}{M_{Pl}}\right)^{\frac{2}{n+1}} \tag{II.14}$$

where E is the sum of the energies of the colliding partons. Hence, the cross section increases with the energy of the colliding partons.

There are several potential modifications to this simple model which can change the result significantly. Each of them introduces a threshold M_{TH} only above which BHs can be produced. This can be expressed in terms of $x_{min} = \frac{M_{TH}}{M_{Pl}}$:

- The fraction of energy of colliding partons that is trapped in the black hole has been assumed to be one. However, detailed calculations have shown that this fraction can be much smaller than one due to energy radiated by gravitational waves during the production process (inelasticity). The fraction of energy available for the BH is particularly small when the impact parameter is close to the Schwarzschild radius [53]. In addition to raising x_{min}, this effect also lowers the cross section depending on the number of extra dimensions [54].

- In order for the black hole to decay thermally (see below), it can be assumed that the Compton wavelength must lie within the Schwarzschild radius: $\lambda = \frac{2\pi}{E/2} \leq r_H$. This results in stricter requirements on x_{min} (see table 2.8.).

- The lifetime can be required to exceed the Schwarzschild radius for thermal BHs in order to allow the BH to re-equilibrate before decaying. In ADD models, this requires $x_{min} > 3$ [54].

These additional requirements increase the energy needed to create a BH at a given mass and therefore reduce the production cross section of BHs. The total

production cross section for BHs in proton-proton collisions $\sigma^{\mathrm{pp\to BH}}_{\mathrm{production}}$ is [51]:

$$\sigma^{\mathrm{pp\to BH}}_{\mathrm{production}}(\tau_m, s) = \sum_{ij} \int_{\tau_m}^{1} d\tau \int_{\tau}^{1} \frac{dx}{x} f_i(x) f_j(\frac{\tau}{x}) \sigma^{ij\to \mathrm{BH}}_{\mathrm{production}} \qquad \text{(II.15)}$$

where $\tau = x_i x_j$ is the product of the momentum fractions of the interacting partons, $\sqrt{s}$ is the center-of-mass energy, $\sqrt{\tau_m s}$ is the minimum energy for which black holes can be produced and $f_i(x)$ and $f_j(x)$ are the parton distribution functions (PDF) [55]. The sum is over all possible combinations of parton types i and j. $\sigma^{ij\to \mathrm{BH}}_{\mathrm{production}}$ is the BH production cross section from two colliding partons of type i and j. Due to the rapidly falling parton distribution functions, the cross section falls rapidly with increasing BH mass. If only BHs above a minimum BH mass (M_{TH}) are allowed, most of the BHs are produced at or slightly above M_{TH}. Hence, the total BH production cross section of all masses depends strongly on $x_{min} = \frac{M_{TH}}{M_{Pl}}$.

number of dimensions	minimal M_{BH}/M_{Pl}
n = 2	8.0
n = 3	9.5
n = 4	10.4
n = 5	10.9
n = 6	11.1
n = 7	11.1

Table 2.8. Constraints on x_{min} from Compton wavelength requirement [50].

Semi-Classical Black Hole Decay

Since no theory of quantum gravity is known, only an approximation of the decay behavior of BHs with a mass well above the Planck scale can be given. It

is assumed that the effects on quantum gravity become smaller as the mass of the BH increases. Hence, in the limit of infinite masses, the classical theory of black holes describes the full behavior of BHs. Therefore, for black hole masses well above the fundamental Planck scale, the decay can be approximated by classical considerations. This is typically expected for BH masses at least four times larger than the fundamental Planck mass ($M_{BH} > 4 \cdot M_{Pl}$). In this energy regime the BH decay can be divided into four phases [51]:

- Balding phase: The BH loses all its asymmetries and quantum numbers via the emission of particles (except for mass, electromagnetic charge and angular momentum).
- Spin-down phase: The angular momentum that was acquired through the colliding partons is lost via the emission of Hawking radiation [56].
- Schwarzschild phase: The BH loses its mass via thermal Hawking radiation.
- Planck phase: The mass M_{BH} approaches the fundamental Planck mass M_{Pl}. Unknown quantum effects start to become significant. Proposals have been made for a complete evaporation or the formation of a stable remnant.

The two main phases during which most of the decay particles are produced is the spin-down phase and the Schwarzschild phase. In these phases, the particle

emission is characterized by the Hawking temperature T_H of the black hole:

$$T_H = \frac{n+1}{4\pi r_H} \tag{II.16}$$

Hence, higher number of extra dimensions correspond to higher Hawking temperatures at a given mass. Using the Hawking temperature, the average number of particles can be approximated by [57]:

$$< N >=< \frac{M_{BH}}{E} >= \frac{M_{BH}}{2T_H} \sim \frac{2\pi}{N+1}(\frac{M_{BH}}{M_{Pl}})^{\frac{n+2}{n+1}} \tag{II.17}$$

If the mass of the BH is well above the Planck mass, the particle multiplicity of BH decays is much larger than one. For BH masses close to the Planck mass, the above approximation is no longer valid and the energy of the decay products is determined by decay kinematics, i.e. $E \approx M_{BH}/2$, which leads to very small particle multiplicities.

The average lifetime of a BH is given by

$$\tau = \frac{1}{M_{Pl}}(\frac{M_{BH}}{M_{Pl}})^{\frac{n+3}{n+1}} \tag{II.18}$$

With a typical lifetime of $\sim 10^{-26}$ s, the BH can be assumed to decay instantaneously. Since BH couple gravitationally to all quantum states of the SM particles, the emission probability is proportional to the number of degrees of freedom of each particle. Hence, particles which carry color charge (quarks+gluons) have the highest relative emissivity due to their larger number of degrees of freedom (see table 2.9.). Other particles with a high relative emissivity are charged leptons, neutrinos and W-bosons.

Particle type	quark	gluon	charged lepton	neutrino	photon	Z-boson	W-boson	Higgs boson
Rel. emissivity	63.9	11.7	9.4	5.1	1.5	2.6	4.7	1.1

Table 2.9. Relative emissivity of SM particles by black holes [50].

The emission spectrum can be further influenced by the charge and angular momentum of the BH. For charged BHs, there is a small bias towards charged particles of the same charge as the BH, while particles with larger spin are more likely to be produced in decays of BHs with higher angular momentum.

Quantum Black Holes

Due to inelasticity and other effects mentioned above which increase the value of x_{min}, it is unlikely that semi-classical BHs are produced at the LHC with a center-of-mass energy of 7 TeV [54]. Since fundamental Planck scales below 1 TeV have been mostly excluded by the D0 and CDF experiments at the Tevatron [58, 59], the BH masses need to be close to the center-of-mass energy of the LHC in order to decay semi-classically. Taken into account the rapidly falling PDF [55], it seems unlikely that a significant number of semi-classical BHs will be produced at the LHC. Therefore, if BHs are produced at the LHC, most of them will be produced with a mass close to the Planck scale (quantum BHs). However, unknown quantum effects will play a significant role in the production and decay of these quantum BHs. Due to the lack of a theory of quantum gravity, it has been suggested to extrapolate

the semi-classical behavior into the mass region close to the Planck scale [60]. This is not expected to give precise results, but rather to give an indication of how quantum black holes will behave. As discussed above, the main difference to the semi-classical decay is the much smaller multiplicity.

In this analysis, the assumption is made that the quantum BHs have a mass so close to the Planck scale that they decay to two particle final states only. In addition, a minimum BH mass M_{TH} is defined below which no black hole production is assumed. Due to their short lifetime, BHs can carry color charge without violating confinement of the strong interaction. In addition, BHs are allowed to carry electromagnetic charge. The notation of the quantum BHs used in the following is:

$$\mathrm{QBH}^{\text{electric charge}}_{\text{color charge}}. \tag{II.19}$$

These assumptions result in a number of interesting BH decay signatures, some of which have a very low background at proton-proton colliders (see table 2.10.). For some decays, a mechanism must be assumed to disable these interactions at lower energies. Otherwise, gravitational interactions would permit flavor-changing lepton decays and other processes through the exchange of virtual BHs, which have not been observed [61]. Table 2.11. shows typical cross sections for quantum BH events, calculated with the QBH generator described in [60].

For quantum BH decays, the di-jet decay channel has the highest branching fraction and would therefore seem to be the prefered signature for a broad search for quantum BHs. However, the background to this channel in proton-proton colliders

quantum state of BH	decay channels	violates conservation rule
QCD singlet, electric neutral	$pp \to QBH_1^0 \to e^+e^-$	
	$pp \to QBH_1^0 \to e^+\mu^-$	
	$pp \to QBH_1^0 \to q\bar{q}$	
QCD triplet, electric charged	$pp \to QBH_{\bar{3}}^{1/3} \to qg$	
	$pp \to QBH_{\bar{3}}^{1/3} \to g\gamma$	lorentz invariance
	$pp \to QBH_{\bar{3}}^{1/3} \to qZ$	lorentz invariance
	$pp \to QBH_{\bar{3}}^{4/3} \to qe$	baryon- and lepton-number conservation

Table 2.10. Quantum black hole decay signatures for for different type of BHs. Some decays violate Standard Model conservation laws.

Production cross section [fb]	n=2	n=5	n=7
Excluding inelasticity effects			
$M_{TH} = 2\,\text{TeV}$	1.9×10^5	9.0×10^5	1.5×10^6
$M_{TH} = 4\,\text{TeV}$	4.5×10^2	1.8×10^3	3.0×10^3
$M_{TH} = 6\,\text{TeV}$	2.4×10^{-3}	9.7×10^{-3}	1.6×10^{-2}
Including inelasticity effects			
$M_{TH} = 2\,\text{TeV}$	1.6×10^3	1.8×10^3	1.7×10^3
$M_{TH} = 3\,\text{TeV}$	2.1	0.63	0.35
$M_{TH} = 4\,\text{TeV}$	4.9×10^{-6}	3.9×10^{-10}	–

Table 2.11. ADD-type quantum black hole cross sections as a function of the number of extra dimensions with and without inelasticity effects. The center-of-mass energy is fixed at 7 TeV and the fundamental Planck mass at 1 TeV. Cross-section are shown for three values of the minimum BH mass M_{TH}. Calculations are based on [60].

such as the Large Hadron Collider is very large and can overwhelm the signal even at high invariant mass. Additionally, many beyond the SM theories predict an excess in the di-jet invariant mass distribution, which would make the source of an observed excess hard to isolate. With a smaller cross section, the lepton+jet decay channel would give a clear indication of new physics. Dominated by events with a W-boson produced in association with one or more jets, the background to this

channel is signficantly smaller than for di-jet events. Finally, the di-lepton decay channel has an even lower branching fraction. In the case of non-observation of any events at high invariant mass, this would reduce the exclusion region of the black hole production cross section compared to the electron+jet signature. In addition, di-lepton events have a irreducable background from $Z \rightarrow \tau^+\tau^-$. Hence, BHs decaying to one lepton and one jet have been studied in this dissertation. However, the search is kept generic in order to allow for resonances originating from other new physics phenomena.

Limits from Collider Experiments

No indication of black holes or extra dimensions has been observed in any collider experiment. The most stringent limits on the fundamental Planck scale M_{Pl} has been set by experiments at the Tevatron [7] and the CERN Large Hadron Collider [62] (see table 2.12.).

At the Tevatron, results have been published by the CDF Collaboration [58] and the D0 Collaboration [59]. CDF reports lower limits on M_{Pl} in ADD models between 0.9 TeV and 1.1 TeV depending on the number of extra dimensions, while D0 finds lower limits on M_{Pl} between 884 GeV and 778 GeV in ADD models. In addition, the D0 experiment gives an upper limit on the cross section of events with a photon and missing transverse energy between 24 fb and 28 fb.

experiment	analysis	cross section limit [fb]	Planck mass limit [TeV]	
CDF	photon/jet + MET [58]		1.4 (n=2)	0.9 (n=6)
D0	photon + MET [59]	24 - 28	0.9 (n=2)	0.8 (n=6)
CMS	di-lepton (electron, muon) [63]	1.4	3.7 (n=2)	2.4 (n=7)
CMS	di-photon [64]		3.3 (n=2)	2.3 (n=7)
ATLAS	monojet + MET [65]		3.2 (n=2)	2.0 (n=6)
ATLAS	di-jet [66]		3.3 (n=2)	3.8 (n=7)
ATLAS	photon + jet [67]	5 ($M_{Pl} > 2$ TeV)		
ATLAS	di-muon [68]	18		

Table 2.12. Selected cross section limits from recent collider experiments. In addition, limits from collider experiments on the fundamental Planck mass in ADD models are shown.

The most stringent limits are currently set by the ATLAS experiment [69] and the CMS experiment [70] at the CERN Large Hadron Collider. At the ATLAS experiment, a search for extra dimensions using events with one jet and large missing transverse energy has resulted in a lower limit of the Planck scale in ADD models between 2.0 TeV (n=6) and 3.2 TeV (n=2), depending on the number of extra dimensions [65]. In addition, from the analysis of di-photon events at the ATLAS experiment a lower limit on the mass of the lightest RS graviton has been set between 0.79 and 1.85 TeV [71]. In a di-jet mass distribution analysis, no excess over the SM background has been found and limits are set between 3.3 (n=2) and 3.8 (n=7) on the fundamental Planck mass M_{Pl} [66].

Based on the di-photon analysis at the CMS experiment, the lightest RS graviton is excluded below 0.86 - 1.84 TeV [64] and a lower limit between 2.3 TeV (n=7) and 3.3 TeV (n=2) is set for the fundamental Planck scale in ADD models. Events with two isolated electrons or muons have also been studied at CMS [63].

The combined upper limit on the signal cross section times branching fraction is found to be 1.4 fb. This corresponds to a lower limit of the Planck mass in ADD models between 2.4 TeV (n=7) and 3.7 TeV (n=2).

An analysis of photon plus jet events recorded by the ATLAS experiment has excluded all Gaussian shaped signal cross section times branching fraction above 5 fb at a 2 TeV mass [67]. In addition, same-sign di-muon final states have been studied at the ATLAS experiment [68]. A model independent limit on the production cross section times branching fraction of 18 fb has been set.

CHAPTER III

THE LARGE HADRON COLLIDER

Introduction

The Large Hadron Collider [6] (LHC) is a roughly circular particle accelerator and storage ring, designed to produce proton-proton and Pb-Pb collisions at high energy and high luminosity [62]. Constructed 50 - 175 m underground in the tunnel that formerly housed the Large Electron-Positron Collider (LEP) near Geneva, Switzerland, the LHC has a total circumference of 26.7 km and a diameter of about 8 km (see figure 3.1.). The particles are stored and accelerated in two parallel beam pipes with a diameter of 6.3 cm each. The two counter-rotating beams are brought to collisions at four interaction points (IP), where different detectors have been built to record the resulting particles: ATLAS and CMS as general purpose detectors, optimized for proton-proton collisions, Alice, designed to study events with high track multiplicities as observed during Pb-Pb collisions, and LHCb, built to investigate B-physics phenomena.

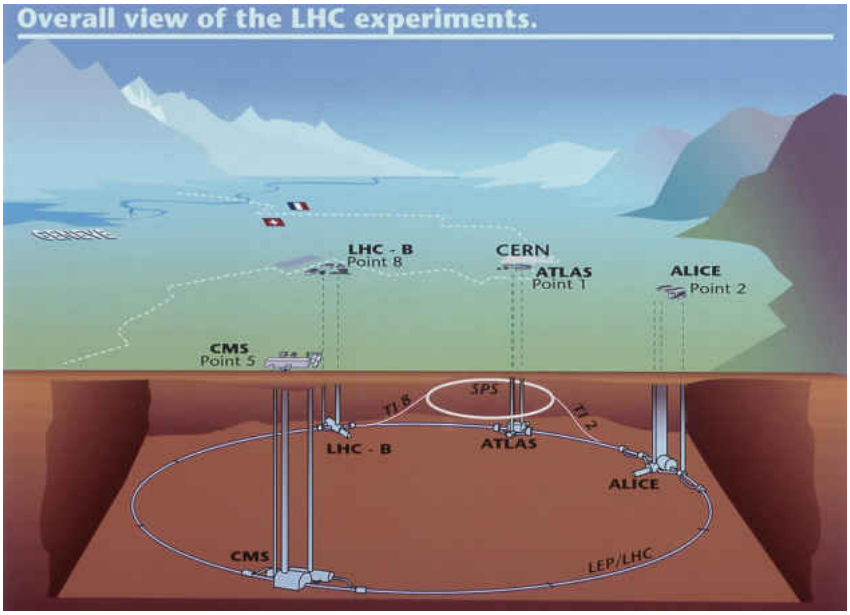

Figure 3.1. Layout of the Large Hadron Collider and its experiments [72].

The LHC Parameters

The LHC contains a total of 9300 magnets in order to manipulate the path of the particles in the beam. Dipole magnets are used to bend the beam onto its circular path inside the beam pipes, while quadrupoles are used for focusing. In addition, eight radio-frequency (RF) cavities per beam are installed, which accelerate the beam from the injection energy of 450 GeV to the maximum beam energy of 7.0 TeV in about 20 minutes. The cavities oscillate with a frequency of 400 MHz, creating buckets of 2.5 ns spacing. Since only 1 out of 10 buckets is filled with particles (bunch), the resulting minimum bunch spacing is 25 ns (see table 3.1.). The particles in the two beams are brought to collision at a design crossing angle

of 28.5 μrad in order to avoid parasitic collisions outside the IPs. Before arriving at one of the four IPs, the beam is squeezed, reducing its transverse size from several millimeters to 16 μm. With 1.15×10^{11} particles per bunch and 2808 bunches per beam, the LHC has a design luminosity of $10^{34}\,\mathrm{cm}^{-2}\,\mathrm{s}^{-1}$ at a center-of-mass energy of 14 TeV. The maximum luminosity during 2011 was $3.65 \times 10^{33}\,\mathrm{cm}^{-2}\,\mathrm{s}^{-1}$ at 7 TeV center-of-mass energy with a bunch spacing of 50 ns and a maximum of 1.4×10^{11} particles per bunch.

Parameter	Parameter value
Beam injection energy	450 GeV
Beam energy	7.0 TeV
Number of particles per bunch	1.15×10^{11}
Number of bunches per beam	2808
Colliding beam size	16 μm
Circumference	26.7 km
Depth	70-140 m

Table 3.1. Summary of the LHC design parameters [6].

Due to the high luminosity and the fixed number of bunch crossings, the average number of interactions is around 20 per bunch crossing at design luminosity. In 2011, the maximum daily average was 17 interactions per bunch crossing. The particles produced by each of the interactions will transverse the detector at the same time. By extrapolating the particles' tracks, it is possible to determine the coordinates of the primary vertices and to associate them with the decay products.

The design center-of-mass energy of the LHC is 14 TeV. It was decided to run

at a reduced center-of-mass energy of 7 TeV during calender year 2010 and 2011 due to the result of the analysis of an accident which occurred on September 19th, 2008. The accident was caused by an electric fault which produced an electrical arc, resulting in mechanical and electrical damage [73].

At nominal running conditions (center-of-mass energy of 14 TeV), the stored magnetic energy at the LHC is approximately 10.4 GJ, while the energy stored in the beams is about 360 MJ per beam. At the end of a fill or in case of unexpected behavior, the beam is directed into two massive absorbers (beam dump) in order to avoid damage to the machine.

The magnets and RF cavities are operated at an temperature of 1.9 K and 4.5 K, respectively. The cryogenic cooling is done using liquid helium which becomes super-fluid at about 2.17 K, increasing its thermal conductivity significantly. In the dipoles, the magnetic field is generated by niobium-titanium (NbTi) cables which first becomes superconductive at a critical temperature of 9.2 K and can stay superconductive up to a critical magentic field of 14 T at a temperature of 2 K [74].

The LHC Injector Complex

The LHC injector complex consists of multiple acceleration facilities, which are used in sequence in order to provide the LHC injection beam with an energy of 450 GeV:

- the Linear Accelerator (Linac) with a beam energy of 50 MeV.
- the Proton Synchroton Booster (PSB) with a beam energy of 1.4 GeV
- the Proton Synchroton (PS) with a beam energy of 26 GeV
- the Super Proton Synchroton (SPS) with a beam energy of 450 GeV

At the LHC, fast pulsing dipole magnets (kicker) are fired synchronously with the arrival of the beam from the SPS, deflecting the incoming beam onto its path inside the LHC. Collimators are installed close to the beamline behind the kicker to protect the machine in case of missing kicks or when kicks are too strong.

CHAPTER IV

THE ATLAS EXPERIMENT

Overview of the ATLAS Detector

The ATLAS (A Toroidal LHC ApparatuS) Detector [69] is one of the two general purpose detectors for probing p-p and Pb-Pb collisions at the CERN LHC built around interaction point one (IP1). Its goal is to provide new insights into the properties of fundamental particles and their interactions at TeV-scale energies. This includes the precise measurement of the behavior of known Standard Model (SM) particles in the new, high energy regime and the search for new phenomena beyond the SM. Special importance has the search for the Higgs boson as predicted by the SM, which has been used as benchmark during the design process. The detector is built to measure the properties of particles produced during collisions at the interaction point in an environment with high radiation, high interaction rate, high particle multiplicity and high energies. At design luminosity, the LHC has a total interaction rate of $10^9\,\mathrm{s}^{-1}$ with an average of 20 inelastic collisions per bunch crossing.

The ATLAS Detector consists of four major components: The tracking system, the calorimeter system, the Muon System and the magnet system. In addition, the ATLAS Detector has a three level trigger system, which reduces the bunch crossing rate from 40 MHz to an event rate of 200-600 Hz by selecting events of interest. These events are analyzed by object identification and reconstruction algorithms and they are permanently stored on tape. In addition to the subsystems, some of the space inside the detector is occupied by cabling and support structure. Since the additional material can impede the ability to measure the particles' properties, a good understanding of the distribution of additional material is vital to a good performance of the detector.

The forward-backward symmetric, cylindrical detector has a total length of 42 m, a radius of 11 m and a weight of approximately 7000 tonnes (see figure 4.1.).

The Atlas Coordinate System

The reference system of the ATLAS Detector consists of a right-handed coordinate system [69] which is centered at the interaction point. The positive z-axis of the ATLAS Detector is oriented along the LHC beam direction toward interaction point 8 (IP8) [6], while the positive x-axis points to the center of the circle described by the LHC. The positive y-axis points upwards. Two angles have been defined: The right hand rotation around the positive z-axis is described by

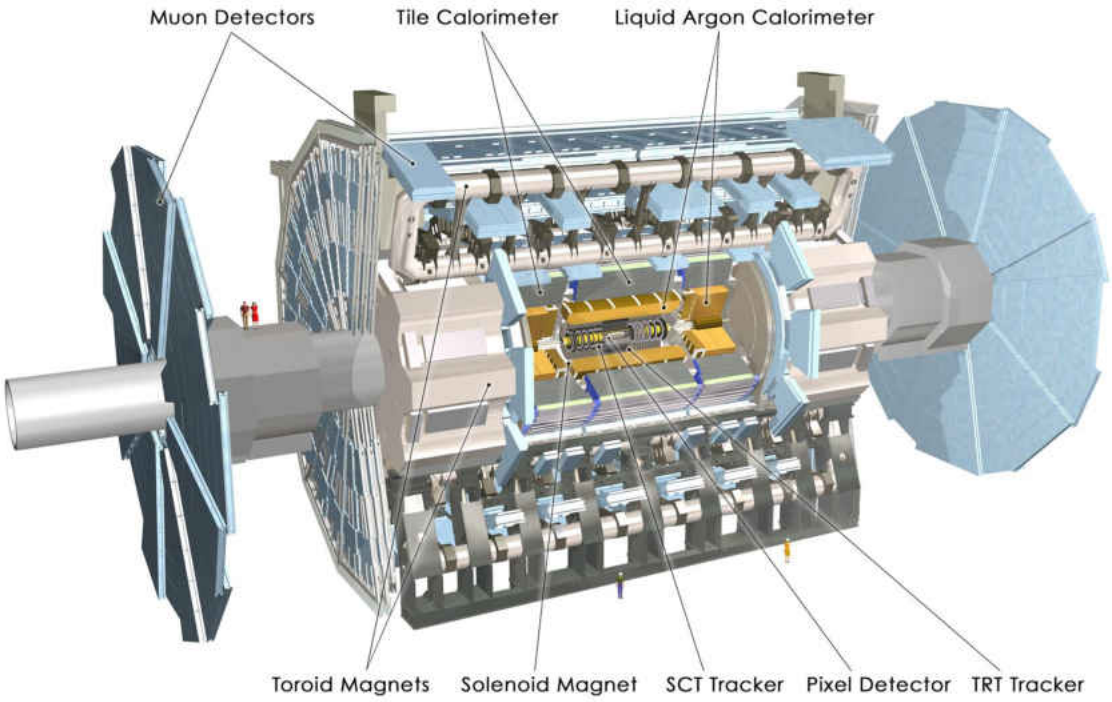

Figure 4.1. Overview of the ATLAS Detector (computer generated image). All four subsystems and their major components are labeled [75].

the angle ϕ with a range of $[-\pi, \pi]$, being zero along the positive x-axis. The second angle θ is zero along the positive z-axis and increases right-handly around the positive y-direction. The pseudorapidity η is defined as

$$\eta = -\log(\tan(\frac{\theta}{2})) \tag{IV.1}$$

The squared radius r is the squared sum of the x and the y coordinate.

The transverse momentum p_T of an object is defined as its momentum transverse to the beam axis and sum p_T is the scalar sum of all transverse momenta in one event. Missing energy is defined as the negative, vectorial sum of all energies

measured in the detector, while transverse missing energy (MET) is the missing energy transverse to the beam axis.

The Inner Detector

The purpose of the Inner Detector (see figure 4.2.) is to measure the direction, momentum and charge of electrically charged particles and to give indications about their identity. Crossing one of the subsystems, a charged particle can liberate a point charge which results in an electric current if a voltage is applied ("hit"). Fitting the various hits produced by a charged particle, tracks can be formed which are associated to the reconstructed particle's path through the Inner Detector. Due to the 2 T magnetic field generated by the super-conducting magnetic Solenoid, the path of a particle describes a curvature inside the Inner Detector from which its momentum can be derived.

For tracking systems, the major conflicting design interest is between maximizing the number of layers and minimizing the dead material. On the one hand, a larger number of layers results in a higher number of hits and better tracking resolution. On the other hand, additional layers increase the dead material in front of the calorimeter which reduces its energy resolution. In ATLAS, the material distribution peaks at 1.5 - 2 radiation length at $\eta \sim 1.5$. Hence, electrons radiate

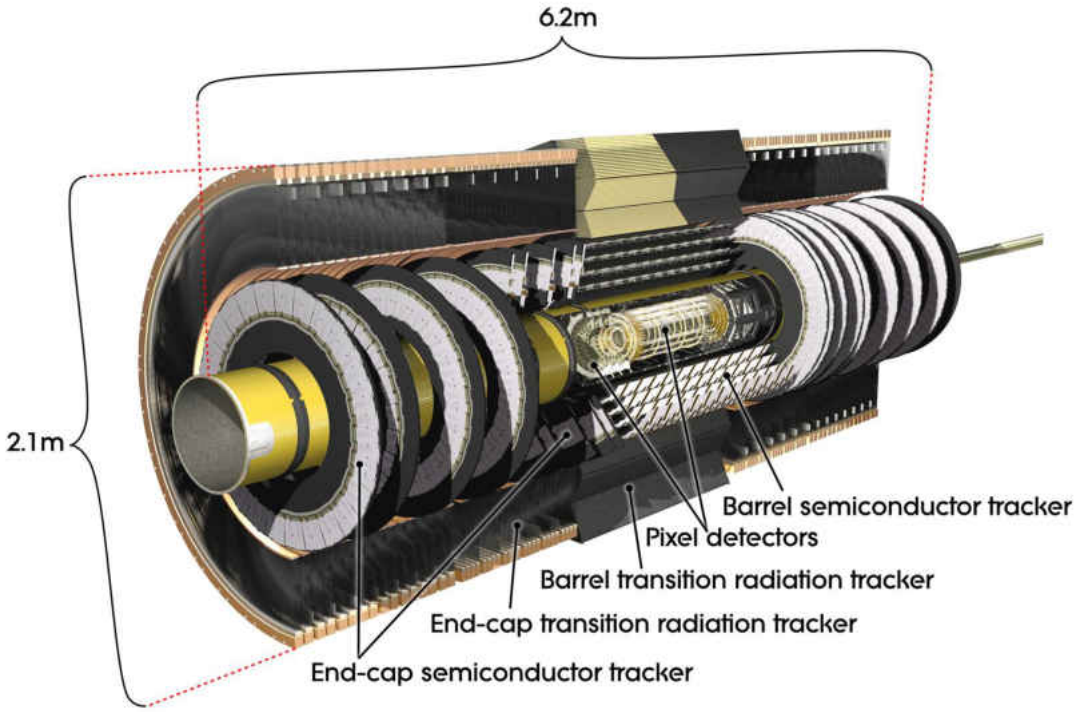

Figure 4.2. The ATLAS Inner Detector (computer generated image). The different tracker subsystems can be seen for both the barrel region and the end-cap. In yellow, the structure that encloses the beam pipe is shown [76].

between 25% and 70% of their energy due to Bremsstrahlung and between 20% and 60% of photons are converted to electron pairs.

Many of the new physics scenarios include the production of b-quark jets and τ leptons decaying hadronically. In order to be able to distinguish them from general QCD jets, a high performance vertex reconstruction capability is needed. This is achieved by the high precision tracking detectors, the Pixel Tracker and the Semi-Conductor Tracker (SCT), covering a range of $|\eta| < 2.5$ with a very high spatial resolution. Since the flux of particles is highest at small radius R, the inner layers are designed to have the smallest cell size. Going to larger radii, the particle

flux falls and the multiple scattering puts a limit on the momentum resolution, which results in a natural limit on the required cell size. The outermost subsystem of the Inner Detector is the lower resolution Transition Radiation Tracker (TRT), which covers a region up to $\eta = 2.0$ (see table 4.1.).

Component	Item	Section	Radial extension [mm]	Extension in η
Overall Inner Detector			$0 < r < 1150$	
Beam pipe			$29 < r < 36$	
Pixel detector	3 cylindrical layers	barrel	$50.5 < r < 122.5$	$\|\eta\| < 1.7$
	2×3 disks	end-cap	$88.8 < r < 149.6$	$1.7 < \|\eta\| < 2.5$
SCT	4 cylindrical layers	barrel	$299 < r < 514$	$\|\eta\| < 1.3$
	2×9 disks	end-cap	$275 < r < 560$	$1.3 < \|\eta\| < 2.47$
TRT	73 straw planes	barrel	$563 < r < 1066$	$\|\eta\| < 0.7$
	160 straw planes	end-cap	$644 < r < 1004$	$0.7 < \|\eta\| < 2.5$

Table 4.1. Summary of the parameters of the Inner Detector[77].

The Pixel Detector

The Pixel Detector is the innermost tracker with the highest granularity. In the barrel region, it consists of three layers in concentric cylinders around the beam axis, with the b-layer being the innermost layer, and of three disks perpendicular to the beam axis on each side as end-cap. Located at a radius of 5 cm around the interaction point, the b-layer and its excellent resolution capability is used to measure secondary vertices. It is mounted directly onto the beam pipe and can be removed after being damaged by hard radiation. Going further out, the distance of the second and third layer to the interaction point is 9 cm and 12 cm, respectively. The end-cap disks have inner and outer radii of 9 cm and 15 cm, respectively. The active components of the Pixel Detector (pixel sensors) are divided into blocks with

a minimal size of of 50 μm in rϕ and 400 μm along the z-axis. All layers in the barrel have the same accuracy per module of 10 μm in rϕ and 115 μm along the z-axis, while the accuracy of the layers in the end-cap is 10 μm in rϕ and 115 μm in r per module in the end-cap. The small pixel size results in a total of about 80 million read-out channels.

The Semi-Conductor Tracker

Located between the innermost Pixel Tracker and the Transition Radiation Tracker, the Semi-Conductor Tracker (SCT) consists of long, narrow microstrips. They are organized on 4 concentric cylinders in the barrel and on 9 disks on each side as end-cap. In the barrel region, which extends to $|\eta| < 1.3$, the strips are directed along the z-axis. This allows the coverage of a larger area compared to the Pixel Detector, while giving a good resolution in rϕ. The layers are numbered from 3 to 6 as a continuation of the three Pixel Detector layers. Each layer consists of two stereo strips of which one is parallel to the beam direction in the barrel, while the second one is installed an an angle of 40 mrad to the beam line. This allows the measurement of the position along the z-axis in addition to the high precision rϕ measurement. The layers are located at radii 30 cm, 37 cm, 44 cm and 51 cm. In the end-cap ($1.3 < |\eta| < 2.47$), for each disk the first set of strips is oriented radially, while a second set is positioned at an angle of 40 mrad. In addition to the determination of the rϕ value and the z-coordinate on the disk, the stereo angle

is used to measure the radial position of the hit. The inner radius of the disks is 27 cm, while the outer radius is 56 cm.

The accuracy of the SCT is 17 μm in rϕ and 580 μm per module along the z-axis in the barrel region. In the end-caps, the accuracy is 17 μm in rϕ and 580 μm in R per module. A track typically crosses four double strip layers, which results in the measurement of eight hits. The total number of readout channels is approximately 6.3 million.

The Transition Radiation Tracker

Positioned outside the SCT, the Transition Radiation Tracker (TRT) consists of parallel drift tubes (straws) of 4 mm diameter filled with a xenon-based gas mixture. Along their centers, the tubes contain gold plated sense wires of 30 μm diameter. The tubes are oriented parallel to the beam line in the barrel and radially in the end-cap. Covering a pseudo-rapidity range of $|\eta| < 2.0$, their length is 144 cm in the barrel and 37 cm in the end-cap. In the barrel at $\eta = 0$, the wires are divided into two halves. The TRT only provides rϕ information with an accuracy of 130 μm per straw. A typical track leaves 36 hits in the TRT, resulting in a much longer track length and a higher number of measurements compared to the Pixel and SCT. This compensates for the lower precision, resulting in a significant contribution of the TRT to the total momentum measurement. There are about 50.000 tubes on each side of the barrel region, while 320.000 tubes are used for the end-caps, resulting in a total of 420 000 read-out channels.

The Transition Radiation Tracker is based on radiation from charged, relativistic particles that cross the boundary of two media with different dielectric constants. It is surrounded by radiating material emitting photons which are measured inside the TRT. The transition radiation intensity depends on the Lorentz factor of the particle, which relates its energy and mass. This allows the distinction of lighter particles with higher Lorentz factors and heavier particles with smaller Lorentz factors. The read-out modules connected to the sense wires can detect two thresholds: low and high. By increasing the ionization, the transition radiation of electrons result in a higher probability of exceeding the high threshold in the straw tube. Hence, an electron can be identified by requiring a high ratio of the number of hits exceeding the high threshold to the number of total hits.

The Calorimeter

In order to measure the position and energy of neutral and charged particles, the ATLAS Detector consists of a calorimeter build around the Inner Detector. It is designed to cover most of the pseudo-rapidity range (up to $\eta = 4.9$) in order to allow precise MET calculations. It is divided in two subsystems, the inner Electromagnetic Calorimeter, optimized for electromagnetic interacting particles, and the outer Hadronic Calorimeter collecting energy deposits of hadrons (see

Fig. 4.3.). Table 4.2. shows the pseudo-rapidity ranges of the different calorimeter subsystems.

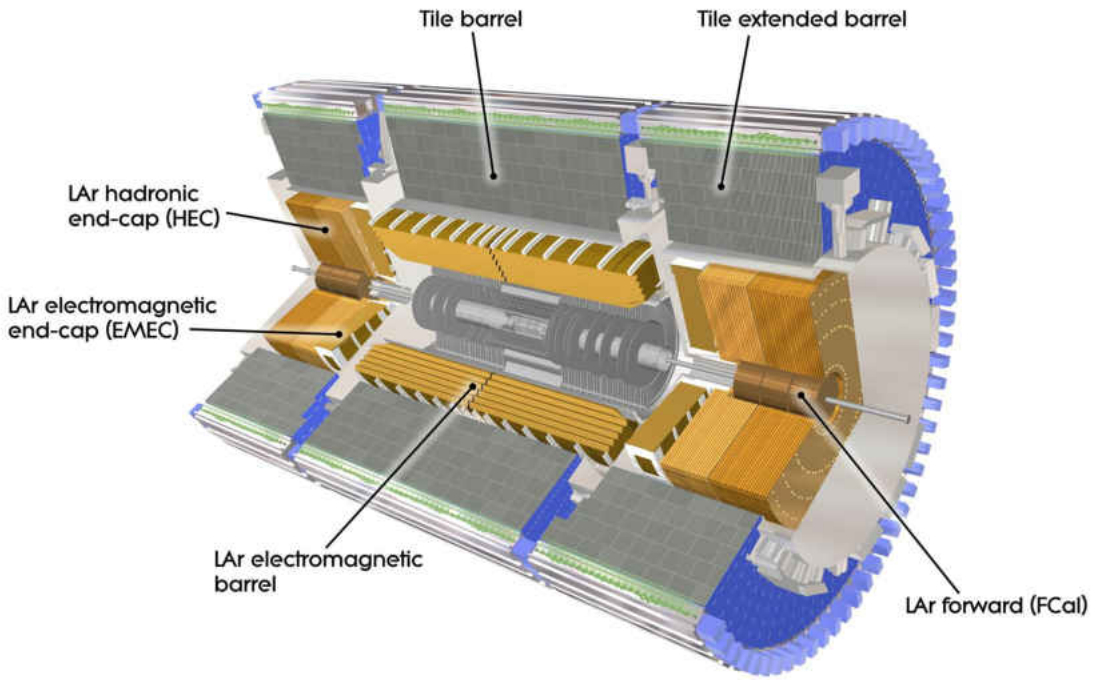

Figure 4.3. The ATLAS Calorimeter (computer generated image). The Electromagnetic Calorimeter and the Hadronic Calorimeter can be seen both in the barrel and in the end-cap. In addition, the LAr Forward Calorimeter is shown [78].

component	section	η range
electromagnetic	barrel	$\lvert\eta\rvert < 1.475$
	end-cap	$1.375 < \lvert\eta\rvert < 3.2$
hadronic	barrel	$\lvert\eta\rvert < 1.6$
	end-cap	$1.6 < \lvert\eta\rvert < 3.2$
	forward	$3.1 < \lvert\eta\rvert < 4.9$

Table 4.2. Pseudo-rapidity ranges of the Calorimeter subsystems[69].

The Electromagnetic Calorimeter

The ATLAS Electromagnetic Calorimeter (EM Calorimeter) uses lead absorber plates and liquid argon (LAr) scintillator in order to measure the energy and position of incoming particles in the region of $|\eta| < 3.2$. LAr is used due to its good energy and spatial resolution in addition to being radiation hard and easy to calibrate [79]. In the barrel region the EM Calorimeter consists of two identical half barrels with a gap of 4 mm at z=0. Two coaxial wheels are installed as end-caps. The inner wheel covers a range of $2.5 < |\eta| < 3.2$, while the outer wheel covers the region with $1.375 < |\eta| < 2.5$. Between the barrel and the end-caps, a small crack exists at $|\eta| \sim 1.47$ which provides space for cables and services (gap-region). Energy reconstruction is known to be poor in this region.

The EM Calorimeter is divided into three longitudinal sections (layers) in the barrel and the outer wheel of the end-cap and two sections in the inner wheel of the end-cap, each with a different spatial resolution.

For $|\eta| < 1.8$, a presampler is installed in addition to the layers in the barrel. It corrects for the energy loss of a particle reaching the EM Calorimeter, which is due to dead material in front of the calorimeter (with a depth of up to 4 X_0). The presampler consists of an active LAr layer of thickness 1.1 cm in the barrel and 0.5 cm in the end-cap region. Its resolution is $\Delta\eta \times \Delta\phi = 0.025 \times 0.1$.

In the barrel, the first layer is used to measure the shower shape of the incoming particles. It has a maximum resolution of $\Delta\eta \times \Delta\phi = 0.0031 \times 0.1$, providing for

an excellent spatial measurement in the η direction. The shower shape in the ϕ direction is distorted by the magnetic field in the Inner Detector resulting in a weaker resolution requirement in ϕ. The amount of showering in η is used to estimate the energy loss which occurred in the dead material in front of the EM Calorimeter. The depth of the first layer is 4 radiation lengths (X_0).

Due to its large thickness of 16 X_0, most of the energy is deposited in the second layer of the EM Calorimeter. It consists of towers of size $\Delta\eta \times \Delta\phi = 0.025 \times 0.025$. The outermost part is a thin, third layer with a thickness between 2 X_0 and 12 X_0 (depending on the η position). It is used to estimate the fraction of electromagnetic energy that escaped the EM Calorimeter ("Hadronic leakage"). Its maximum resolution is about half the resolution in the second layer ($\Delta\eta \times \Delta\phi = 0.05 \times 0.025$).

In total, at the end of the third layer, there is about 24 X_0 of material in the barrel and about 26 X_0 in the end-cap.

The absolute energy resolution of the EM Calorimeter can be approximated by the quadratic sum of the energy uncertainty coming from three different sources:

a - Electronic noise, which is independent of the energy.

b - The intrinsic fluctuation of EM showers, which is proportional to $\sqrt{E}$, where E is the deposited energy.

c - Sources proportional to the deposited energy, like mechanical imperfections of the hardware or incomplete shower containment.

This can be summarized by

$$\frac{\sigma(E)}{E} = \frac{a}{E} \oplus \frac{b}{\sqrt{E}} \oplus c \tag{IV.2}$$

For electrons with an energy between 10 and 245 GeV, the resolution is dominated by the intrinsic fluctuation of EM showers and the local constant term c. The stochastic term b is measured to be around 9.4%, while c is around 0.1% in the barrel region [80].

The angular resolution is

$$\frac{50 - 60\,\text{mrad}}{\sqrt{E[\text{GeV}]}} \tag{IV.3}$$

The Hadronic Calorimeter

The Hadronic Calorimeter is divided into three separate parts, each with a total thickness of about 12 interaction lengths λ (including support structure). In the central region (up to $|\eta| = 1.7$), the Tile Calorimeter uses steel absorber plates and scintillating tiles as active material. The tiles are read-out by wavelength shifting fibers into two photomultiplier tubes. The Tile Calorimeter consists of one central barrel, covering the region of $|\eta| < 1.0$ and two extended barrels in the range of $0.8 < |\eta| < 1.7$. The inner radius of the barrels is 2.28 m, while the outer radius is 4.25 m. The Tile Calorimeter is further subdivided into three longitudinal layers. The thickness of the first, second and third layer is 1.5, 4.1 and 1.8 λ, respectively,

in the barrel and 1.5, 2.6 and 3.3 λ in the extended barrel. The total interaction length is λ of 9.7 at $\eta = 0$ in the barrel and $\lambda = 10$ in the end-cap. The cell size in the Tile Calorimeter is $\Delta\eta \times \Delta\phi = 0.1 \times 0.1$ in the first two layers and $\Delta\eta \times \Delta\phi = 0.2 \times 0.1$ in the third layer.

For $|\eta|$ between 1.5 and 3.1, the hadronic energy is measured using the Liquid Argon Hadronic End-cap Calorimeter (HEC), which uses copper absorber plates filled with liquid argon scintillator. The radiation hard liquid argon is the preferred material in this high radiation region of $|\eta| > 1.5$. The HEC consists of two wheels on each side overlapping slightly with the inner electromagnetic calorimeter and the outer LAr Forward Calorimeter in order to compensate for the lower material thickness in the transition region. Each wheel is composed of 32 identical modules in two layers of absorber plates, resulting in a total of four layers on each side. The thickness of the absorber plates in the second layer is 25 mm in the inner wheel and 50 mm in the fourth layer at the outer wheel. The first plate on each wheel has half the thickness of the second plate.

Used for both electromagnetic and hadronic energy measurement in the region of $4.9 > |\eta| > 3.2$, the Liquid Argon Forward Calorimeter consists of three modules on each side with a depth of about 10 λ (including 1.5 λ of support structure). Due to the large thickness, only a small fraction of hadronic interacting particles pass through the detector into the Muon System (punch-throughs). Optimized for electromagnetic measurements, the first module on each side uses copper as

absorber, while in the second and third modules, which are optimized for hadronic energy measurement, the absorber is made of tungsten. Each module consists of a set of metal rods in parallel to the z-axis, which is embedded into a block of metal. For each layer, there is a gap between the rods and the tubes, which is filled with LAr used as sensitive material. The gap size is 250 μm, 375 μm and 500 μm for the first, second and third layer, respectively.

The energy resolution of the Hadronic Calorimeter depends on the energy deposit and the η position. It has a similar parameterization as the resolution of the EM Calorimeter described by equation IV.2. The measured values for hadrons with energy between 3 GeV and 350 GeV in the Tile Calorimeter is 52.9% for the stochastic term b and 5.7% for the constant term c. Uncertainties due to electronic noise are negligible [81].

For reconstructed jets from the energy deposition in the Tile Calorimeter, the resolution depends also on the cone size of the jet reconstructed. The optimal cone size regarding energy resolution depends therefore on the luminosity, the detector occupancy and the jet energy.

The Muon Spectrometer

The Muon System together with the Toroid is the largest subsystem of the ATLAS Detector and occupies most of its volume. It consists of aluminum drift

tubes which are used to measure the track of the muon. The drift tubes are 30 mm in diameter and filled with a gas mixture of 93% argon and 6% CO_2. In the barrel region, the tubes are arranged in three cylindrical layers (chambers) around the beam line and in layers perpendicular to the beam line in the end-cap region. Each muon interacts on average with three layers.

The precises measurement of the track over most of the η region is done by Monitored Drift Tubes (MDT). They cover the range of $|\eta| < 2.7$ ($|\eta| < 2.0$ for the innermost layer). For larger pseudo-rapidities ($2.0 < |\eta| < 2.7$), Cathode strip chambers (CSC) with higher granularity is used for the innermost plane, due to better tolerance to higher rates and more challenging background condition (see figure 4.4.).

For the Trigger System, which covers a range of $|\eta| < 2.4$, Resistive Plate Chambers (RPC) are used in the barrel and a Thin Gab Chambers (TGC) for the end-cap (see table 4.3.).

component	η range
Monitored Drift Tubes	$\|\eta\| < 2.7$ ($\|\eta\| < 2.0$ for the innermost layer)
Cathode Strip Chambers	$2.0 < \|\eta\| < 2.7$
Resistive Plate Chambers	$\|\eta\| < 1.05$
Thin Gap Chambers	$1.05 < \|\eta\| < 2.7$

Table 4.3. Pseudo-rapidity ranges of the Muon Spectrometer [69].

Very stringent alignment requirements of layers within the muon chambers and between muon chambers are necessary in order to ensure a high precision muon

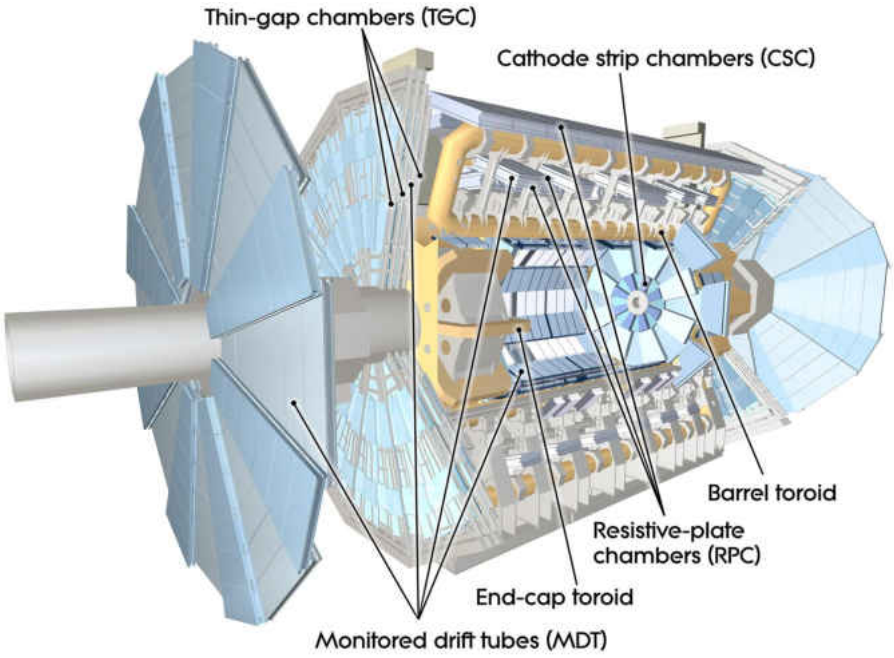

Figure 4.4. The ATLAS Muon Spectrometer (computer generated image) [82]. The Monitored Drift Tubes, the Cathode Strip Chambers, the Resistive Plate Chambers and the Thin Gab Chambers can be seen. In addition the Toroid Magnets are shown.

tracking. An accuracy of about 30 μm is achieved by precision mechanical-assembly techniques in addition to the usage of an optical alignment system. By studying the muon tracks during early running in 2010, the alignment was further improved.

The Magnet System

There are two magnet systems in ATLAS: The Solenoid, which bends the trajectory of charged particles inside the Inner Detector, and the Toroid, which deflects muons inside the Muon Spectrometer.

The Solenoid, placed directly behind the Inner Detector, provides a 2 T axial field to bend charged particles in the tracking system. Its length is 5.3 m and the inner and outer diameters are 2.46 m and 2.56 m, respectively. By sharing a vacuum vessel with the LAr calorimeter, the material thickness of the Solenoid was minimized to be about 0.66 X_0. The total stored energy amounts to 40 MJ, which in case of a quench is absorbed by the enthalpy of the cold mass increasing the temperature to 120 K from a nominal value of 4.5 K.

The Toroid consists of large superconducting air-core toroid magnets. An iron core is not used inside the magnet, as it would increase multiple scattering of muons, degrading their tracking resolution. The disadvantage of not having an iron core is a decrease of the maximal achievable strength, which decreases the bending power. The lack of an iron core is partially compensated by the large size of the Muon System.

The Toroid is divided into two parts: A large barrel toroid, covering $|\eta| < 1.4$ and two smaller end-cap magnets on each side for the region of $1.6 < |\eta| < 2.7$ (see figure 4.4.). In the transition region between the toroids, the magnetic field is a combination of the barrel and the end-cap toroid field. Each toroid consists of eight coils that are positioned radially around the beam axis. In the end-cap, the coils are placed at an angle of 22.5 ° to the barrel coils. This ensures radial overlap of the two systems and is the result of optimizing the bending power in the

transition region. In the barrel, the coils are housed in individual cryostats, while in the end-cap, an aluminum allay is used for housing.

The bending power of the Toroid is described by the integral $\int B_{\perp} dl$, where $B_{\perp}$ is the magnetic field perpendicular to the muon direction. The integral is computed over the trajectory of a muon with infinite momentum between the innermost and outermost chamber of the Muon System. In the barrel toroid, the bending power is between 1.5 and 5.5 Tm, while it is between 1 and 7.5 Tm in the end-cap region. The bending power in the transition region is lower and varies significantly along η.

The Trigger and Data Acquisition System

The ATLAS Trigger and Data Acquisition system (TDAQ) is designed to select events in three steps and store them permanently. The 40 MHz bunch crossing rate is reduced to 75 kHz by the hardware based Level 1 trigger (L1), which has a decision time of $\sim 2.5\,\mu$s. Based only on information from the calorimeter and the muon spectrometer, it identifies Region of Interests (RoIs) in η-ϕ-space for the higher level trigger systems. Using the full granularity of the detector, the software based Level 2 trigger (L2) further analyzes the RoIs with a latency of ~ 40 ms to reduce the rate to a few kHz. The Level 3 trigger or Event Filter (EF) takes the final decision, using the full detector information, and reduces the event rate to

up to 600 Hz. The maximum latency of the EF is 4 s. All events passing the EF are sorted into different streams, depending on the trigger signature that has been found. After being further analyzed by the object identification and reconstruction software, the events are permanently stored.

Instantaneous Luminosity Measurement

The ATLAS Detector has several independent methods to measure the instantaneous luminosity. The absolute luminosity can be calculated from the parameters of the LHC machine, which are published to the experiments. It can also be derived by measuring the production rate of either the W-boson or the Z-boson decaying to a lepton plus a neutrino or two leptons, respectively, or two photons decaying to two muons with opposite charge. The cross section of these processes is well established by previous experiments, so that the luminosity can be calculated with high precision. In addition, two dedicated detectors have been installed: LUCID (Luminosity measurement using Cerenkov Integrating Detector) and ALFA (Absolute Luminosity for ATLAS). LUCID is used to measure the relative luminosity, which can be scaled to give the absolute luminosity, while ALFA is designed to give the absolute luminosity directly. During 2011 data taking, LUCID has been the primary source of luminosity information. In the following, the detector and the calibration during 2011 is briefly described.

LUCID

LUCID Luminosity measurement using Cerenkov Integrating Detector consists of 200 aluminum tubes filled with C_4F_{10} at atmospheric pressure. Placed at $|z| = 17\,\text{m}$ at both sides in the forward region, it measures the number of inelastic proton-proton scattering using Cerenkov radiation. Due to the excellent linear relationship range between the number of detected particles and the luminosity over a large range, the relative instantaneous luminosity can be calculated with high precision.

2011 Luminosity Callibration

The instantaneous luminosity during data taking can be derrived by measuring the visible interaction rate per bunch crossing μ_{vis} [83]:

$$L = \frac{\mu n_b f_r}{\sigma_{\text{inel}}} = \frac{\mu_{\text{vis}} n_b f_r}{\sigma_{\text{vis}}} \tag{IV.4}$$

where L is the luminosity, μ is the average interaction rate per bunch crossing, n_b is the number of colliding bunches and f_r is the machine revolution frequency. The visible cross section σ_{vis} is equal to the total inelastic cross section multiplied by the detector and algorithm efficiency:

$$\sigma_{\text{vis}} = \epsilon \cdot \sigma_{\text{inel}} \tag{IV.5}$$

Because only μ_{vis} can be measured by LUCID during data taking, the visible cross section σ_{vis} has to be known in order to calculate the instantaneous luminosity. σ_{vis} is measured during dedicated von der Meer scans [83] [84], in which the beam seperation in both the x and y direction is varied. This allows the determination

of the transverse effective beam sizes and the maximum archievable collision rate $\mu_{\text{vis}}^{\text{max}}$ by fitting the interaction rate as a function of the beam seperation. Using the effective transverse beam size σ_{ix} and σ_{iy} of beam i $(i = 1, 2)$, the instantaneous luminosity is [85]:

$$L = \frac{n_b f_r n_1 n_2}{2\pi\sqrt{(\sigma_{1x}^2 + \sigma_{2x}^2) \cdot (\sigma_{1y}^2 + \sigma_{2y}^2)}} \tag{IV.6}$$

where n_1 and n_2 are the bunch intensities (number of protons per bunch). Hence, the visible cross section can be derived from equation IV.4:

$$\sigma_{\text{vis}} = \mu_{\text{vis}}^{\text{max}} \frac{2\pi\sqrt{(\sigma_{1x}^2 + \sigma_{2x}^2) \cdot (\sigma_{1y}^2 + \sigma_{2y}^2)}}{n_1 n_2} \tag{IV.7}$$

Using the visible interaction rate μ_{vis} measured by LUCID, the instantaneous luminosity during data taking can be calculated using equation IV.4. The total relative uncertainty of the luminosity measurement for the data used in this analysis is 3.7% [86] [83].

CHAPTER V

EVENT RECONSTRUCTION AND OBJECT IDENTIFICATION

The data that is recorded by the ATLAS Detector is analyzed using a set of standard object reconstruction and identification algorithms. They are designed to identify specific objects with high efficiency while rejecting fake signatures at a high rate. In this chapter, the Sliding Window Clustering and tracking algorithms are described first, since their output is the input for most of the other algorithms. Electrons, jets and photons are used extensively in this analysis and their reconstruction and identification algorithm is described in detail. A short overview of the algorithms for muons and hadronically decaying taus is given, as they are used only indirectly in the calculation of MET, which is described last.

Sliding Window Clustering

In order to find clusters of energies deposited in the Calorimeter, the Sliding Window Cluster Algorithm [87] has been developed. It reconstructs the energy deposit of electrons and photons in the EM Calorimeter and of taus in both the electromagnetic and Hadronic Calorimeter. The cluster algorithm consists of three

steps: tower building, seed finding (pre-clustering) and cluster filling. The output of the tower building algorithm is also used to reconstruct jets.

The tower building algorithm divides the η-ϕ-space into a grid of $N_\eta \times N_\phi$ elements of equal size $\Delta\eta \times \Delta\phi$. The energy of all cells in all longitudinal layers are added in order to calculate the total energy of the tower. The parameters used for electrons/photons and taus are shown in table 5.1.

particle type	electrons/photons	taus
tower type	EM	combined
calorimeters	EMB, EMC	all
$\eta_{\min}$, $\eta_{\max}$	-2.5, 2.5	-5.0, 5.0
N_ϕ, N_η	256, 200	64, 100
$\Delta\phi$, $\Delta\eta$	0.025, 0.025	0.1, 0.1

Table 5.1. Parameters of the Tower Building Algorithm for electrons/photons and taus [87].

The seed finding algorithm calculates the energy of each possible rectangular window with tower size $N_\eta^{\text{window}} \times N_\phi^{\text{window}}$. If the transverse energy of a window is above the given threshold E_T^{thresh}, a pre-cluster is formed. The position of the pre-cluster is the energy weighted average position of all cells inside a window of $N_\eta^{\text{pos}} \times N_\phi^{\text{pos}}$ towers. Using a smaller window for the position calculation of the pre-cluster results in a smaller sensitivity of the position to noise in the Calorimeter. In order to remove duplicates, only the cluster with the highest transverse energy is kept, if the distance in $\Delta\eta$ or $\Delta\phi$ of two clusters is smaller than $\Delta\eta_{\text{dupl}}$ or $\Delta\phi_{\text{dupl}}$, respectively. A summary of the parameters is shown in table 5.2.

Cluster Type	EM	Combined
$N_\eta^{\text{window}} \times N_\phi^{\text{window}}$	5×5	5×5
E_T^{thresh} [GeV]	3	15
$N_\eta^{\text{pos}} \times N_\phi^{\text{pos}}$	3×3	3×3
$\Delta\eta_{\text{dupl}}$, $\Delta\phi_{\text{dupl}}$	2, 2	2, 2

Table 5.2. Parameters of the Seed Finding Algorithm [87]. $\Delta\phi_{\text{dupl}}$ and $\Delta\eta_{\text{dupl}}$ are in units of towers defined in table 5.1.

The last step of the Sliding Window Clustering is the cluster filling. The energy of all cells in a region around the position of the pre-cluster is added. This algorithm has changed significantly over time and is differently used by different reconstruction algorithms. The nominal method is to add the energy in a rectangle of either 3×5, 3×7 or 5×5 in $\Delta\eta \times \Delta\phi$. However, in the version used for this analysis, the cluster filling is done after the identification for electrons and photons, so that only the seed of the pre-cluster is used from the Sliding Window Clustering.

Tracks

The track reconstruction algorithm [88] uses the hits as measured in the Inner Detector to create sets of associated hits (tracks). There are two separate algorithms in the track reconstruction that are both executed during track reconstruction: inside-out tracking and outside-in tracking.

Inside-Out Tracking

The goal of the inside-out tracking algorithm is to find tracks seeded by hits

in the two silicon detectors. First, the measurements in the silicon detector are transformed to global three-dimensional representations (spacepoints). The spacepoints in the Pixel Detector are used to find the track seeds by finding pairs of hits from which the z-vertex can be built. In order to further constrain possible associations, a fast primary vertex search is performed on the seeds with three or more spacepoints. From the directional information of the seeds, a road through the Inner Detector is constructed in order to find additional hits that can be associated to the track candidate. This is done using the Kalman fitter-smoother formalism [89]. The hits are successively added to the track candidate fit, updating the track information after each addition. This improves the prediction of the track representation on the next layer. In addition, outliers are detected by large contributions to χ^2 of the track. After all potential track candidates are reconstructed, ambiguities between them are resolved. Last, each track is extrapolated into the TRT detector to find additional associated hits.

Missed and misidentified tracks from the inside-out tracking algorithm can be caused by one of the following problems:

- Large number of hits may shadow track seed.
- Tracks from secondary vertices, which may not have enough silicon hits, may not be found.

- Substantial energy loss of the particle due to bremsstrahlung may prevent the association of TRT hits to tracks.

In order to find the missed tracks, a second sequence of track reconstruction is used, the outside-in tracking.

Outside-In Tracking

The outside-in tracking starts with the information retrieved from the TRT drift tubes. Since they don't supply the position coordinate in the direction of the tube, the hits are projected onto a plane: R-ϕ-plane in the TRT barrel and R-z-plane in the TRT end-cap. On both planes the tracks describe a straight line from the primary interaction region, which can be reconstructed using the Hough Transform [90]. The measured coordinate space is transformed into the Hough space, whose two dimensions are the two parameters of a straight line fit. Each point on one line is transformed into a curve in Hough space, whose points represent various straight lines through the point in the image space. As a consequence, the track finding problem is equivalent of finding local maxima in the two-dimensional Hough histogram. This is done for several slides in η to remove overlaying track segments. Due to the missing coordinate information along the TRT tubes, each hit can be used in different η slices. This ambiguity is resolved by maximizing the number of straw hits found per track candidate. After all track candidates are found in the TRT, they are extrapolated back into the silicon detector in order to associate the remaining hits.

Tracks from both tracking algorithms are used in particle reconstruction algorithms and in further analyses.

Electrons

A typical electron is expected to leave a track in the Inner Detector and to deposit energy in the EM Calorimeter. Hence, the electron reconstruction algorithm usually requires an energy deposit that is matched to a track. In ATLAS, there are three electron reconstruction algorithms for different types of reconstructed electrons. The default algorithm reconstructs a standard electron which is optimized for high p_T isolated electrons. The standard electrons are seeded by a cluster reconstructed in the EM Calorimeter which is matched to a track. The second algorithm is optimized for very low p_T electrons and electrons inside jets. It is seeded by a track in the Inner Detector which is matched to an energy deposit in the EM Calorimeter. The third algorithm reconstructs electrons in the forward region from clusters in the Calorimeter. No track matching is required for this type of reconstructed electrons, since there is no Inner Detector information in this region.

For this analysis, standard reconstructed electrons are used which are described in more detail below.

Standard Reconstructed Electrons

A standard reconstructed electron [91] is seeded by a cluster in the EM Calorimeter found by the Sliding Window Clustering. For each layer in the Calorimeter, the barycenter of the energy deposit is calculated. All shower shape variables used in the identification process are derived with respect to this barycenter. The reconstructed cluster is matched to a track using the η and ϕ position of the barycenter. For tracks with hits in the Pixel Detector or the SCT, the η and ϕ of each track is compared to the position of the cluster. They are considered to match if $\Delta\eta < 0.05$ and $\Delta\phi < 0.1$. For matched tracks, the track trajectory is extrapolated to each compartment of the Calorimeter and $\Delta\eta$ and $\Delta\phi$ are calculated. The information of $\Delta\eta$ and $\Delta\phi$ taken in the second layer of the EM Calorimeter is used as the distance between the track and the cluster. All tracks are attached to the electron, ordered by their distance to the calorimeter deposition. The best match is defined as the track with the smallest distance to the cluster. For tracks with no hits in the Pixel Detector or the SCT, only the ϕ coordinate is considered, since no measurement of η is made. All other requirements remain unchanged.

Electron Identification

The ratio of rates of isolated electrons to QCD jets is around 10^{-5} at the LHC (in a p_T range of 20-50 GeV). In order to acquire pure samples of electrons, as needed by a large number of analyses, ATLAS requires an excellent electron

identification performance. This is achieved by a cut-based method which depends on calorimeter-based variables, tracking variables and variables that combine information from the Calorimeter and the Inner Detector. Other methods for identifying electrons have been studied and implemented, but they are currently not recommended for physics analyses by the ATLAS experiment.

The variables derived from calorimeter information that are used in the cut-based method rely mostly on the shower shape of electrons. In order to reject jets containing π^0 with high energy and a wide shower, three calorimeter-based variables are used:

- The hadronic leakage defined as the transverse energy in the first sampling of the Hadronic Calorimeter behind the reconstructed cluster.
- The lateral shower shape in the second sampling of the EM Calorimeter (where most of the energy of the electron is deposited). It is defined as the ratio of the energy deposited in two rectangles of 3×7 and 7×7 in $\eta \times \phi$ around the seed.
- The lateral width, which is the width of the energy distribution in the second sampling.

After selecting electrons based on these variables, the main remaining QCD objects which can fake an electron are jets with muons and π^0. The second type of jets often produces two maxima in the energy distribution. This can be detected

using the high granularity of the first layer of the EM Calorimeter. If $\eta < 2.35$ and the energy fraction in the first layer is more than 0.5% of the total energy in both calorimeters, a search for a second maximum in the energy distribution is performed in a window of $\Delta\eta \times \Delta\phi = 0.125 \times 0.2$. If a second maximum is found, the following two variables are used to reject jets containing π^0s:

- The ratio of the energy of the second maximum and in the strip with the lowest energy located between the two maxima.
- The energy of the second maximum as a fraction of the total transverse energy.

In addition, the shower width in η can be used to improve the jet rejection further. As a result, only very narrow showers with no pronounced second maximum pass the selection.

After the selection based on calorimeter variables, most of the fake electrons left come from photon conversions and low multiplicity jets. They can be further rejected by requiring good quality tracks matched to the cluster. The definition of good quality tracks includes:

- A minimum of nine precision hits (in Pixel and SCT).
- At least two total hits in the Pixel Detector.
- At least one of the two hits in the b-layer of the Pixel Detector, which greatly reduces photon conversions.

- An absolute transverse impact parameter below 0.1 cm.

In addition, the TRT detector is used to improve the performance of the electron identification algorithm. Tracks are rejected with a low fraction of high-threshold TRT hits to the total number of TRT hits.

The electron selection is further improved by using variables that combine the information of the Calorimeter and the Inner Detector:

- The difference in η and ϕ between the cluster and the track.

- The energy as measured in the Calorimeter is compared to the momentum measured in the Inner Detector. For electrons the values should match.

In order to facilitate the usage of these selection variables in different analyses, three reference sets have been defined: loose, medium and tight identification. The loose identification uses variables from the second layer of the EM Calorimeter and hadronic leakage. The medium selection adds variables from the first EM layer, track quality cuts and track-cluster matching. The energy ratio between the Calorimeter and the Inner Detector, b-layer hits and TRT identification requirements are added to the medium selection to define the tight identification. This provides for optimized selection for different analysis requirements regarding electron purity and fake electron rejection.

Photons

As neutral particles, photons typically leave no track in the Inner Detector, but deposit energy in the EM Calorimeter. Hence, a reconstructed and identified photon requires an energy cluster in the EM Calorimeter which can not be matched to a track. In addition, photons can convert to two electrons during their flight inside the Inner Detector, which results in one or two tracks (converted photons).

Photon Reconstruction

As in the case for electrons, the photon reconstruction algorithm [92] is seeded by the Sliding Window Clustering Algorithm. In addition, a loose cut on the hadronic leakage is applied in order to reduce the number of reconstructed photons. The barycenter is calculated in each sampling of the EM Calorimeter, which is used for all shower shape calculations.

If photons are converted to electrons inside the Inner Detector, there can be either a secondary vertex with two tracks or one single track found. The single track is required to not have a b-layer hit. For most vertices and tracks, a matching to the cluster reconstructed by the Sliding window clustering is required. The matching is done differently for the three types of track pattern [93]:

- For symmetric double tracks with a ratio of p_T of the higher momentum track to the track with the lower momentum of less than 4: Each track is

extrapolated to the second sampling of the EM Calorimeter and required to match the cluster.

- For asymmetric double tracks, with a ratio of p_T of the higher momentum track to the track with lower momentum of more than 4: A candidate converted photon, calculated from the two tracks, is extrapolated to the second sampling of the EM Calorimeter as neutral particle and required to match the cluster.

- For single-track, the track is extrapolated to the second sampling of the EM Calorimeter and required to match the cluster.

For tracks with at least four silicon hits, the requirement for the matching of track and cluster is $\Delta\eta < 0.05$ and $0.05 < \Delta\phi < 0.1$. The higher distance in $\Delta\phi$ is a result of losses due to bremsstrahlung. For tracks with less than four silicon hits, the precise geometry of the detector is taken into account. This avoids the matching of tracks to clearly inconsistent clusters. For candidate converted photons, the requirement is $\Delta\eta < 0.05$ and $\Delta\phi < 0.05$ for tracks with more than four silicon hits and only $\Delta\eta < 0.05$ otherwise. If neither vertex nor track is matched to the cluster, the cluster is considered an unconverted photon.

From the cluster, the energy and position of the photon are calculated taking into account the different calorimeter response in various η and ϕ regions and the leakage of energy outside the cluster.

Photon Identification

The photon identification algorithms depends on the same calorimeter-based variables as the electron identification:

- Variables based on hadronic leakage.
- Shower shape variables in the second layer of the EM Calorimeter.
- Variables based on a second maximum in the energy distribution and shower shape variables in the 1st layer of the EM Calorimeter.
- Isolation variables.

Jets

Jet Finding Algorithms

The goal of a jet finding algorithm is to group the elements of an input set of four-momenta into different subsets. For each resulting subset, the four-momenta are combined to a final four-momentum (jet). At the ATLAS experiment, jet algorithms are used to reconstruct the energy deposit in the Hadronic Calorimeter of decay products originating from strongly interacting particles. The recombination rule is independent of the jet finding algorithm. If p^k is the four-momentum of the

combination of n four-momenta p^i, then

$$p^k = \sum_{i=1}^{n} p^i \tag{V.1}$$

This conserves energy and momentum, but does not assume zero jet mass as other recombination rules.

There are a large number of different types of jet finding algorithms that have been developed for various reasons. At the ATLAS experiment, two types have been used: A cone-based algorithm, which combines all four-momenta around a seed in a given cone, and the anti-kt clustering algorithm, which combines pairs of objects until certain conditions are met.

Cone Algorithms

The cone-based jet finding algorithms cover a wide range of similar algorithms. A typical algorithm is seeded by a calorimeter tower or a cluster with energy above a certain threshold. The energy of all four-momenta in a cone in η-ϕ-space around each seed is added and a new barycenter for each cone is calculated. This is repeated with the new barycenter as seeds until a set of stable cones are found. The combined four-momentum inside each cone are considered the reconstructed jets. There are two different procedures to remove overlapping cones: The progressive removal, where all the energy of the jet with the highest p_T is removed and the algorithm is re-run, and the split/merge procedure, where overlapping cones are either split into two jets or combined to one. In the split/merge procedure, the jets are combined,

if the fraction of energy in the overlap region out of the total jet energy is larger than a defined threshold. The progressive removal is used by the CMS experiment, while the split/merge procedure is used at the ATLAS experiment. However, the cone algorithm is not recommended to be used in physics analyses at the ATLAS experiment.

Being infrared and collinear unsafe, the classical cone algorithm is not usable in NLO calculations. However, this has been resolved by the Seedless cone algorithm (SISCone) [94], for which no seed is used. The cones are calculated for all possible permutations of the input four-momenta pairs.

Cluster Jet Algorithm

For the clustering jet finding algorithm [95] [96] a distance between two four-momenta is defined, and the two closest input four-momenta are combined using the combination rule described above. This is repeated with the new combined four momentum replacing the two closest four-momenta until a terminal condition is met and the four-momentum is considered to be the final jet. This jet is removed from the list of four-momenta and the procedure is repeated until no four-momenta are left, resulting in a list of final jets. In the following, the cluster algorithms used at the ATLAS experiment are described in detail.

First, for each four-momentum and each pair of four-momenta, the distance is

defined as

$$d_{ij} = min(k_{T_i}^{2p}, k_{T_j}^{2p}) \frac{(\Delta R)_{ij}^2}{R^2} \tag{V.2}$$

$$d_{iB} = k_{T_i}^{2p} \tag{V.3}$$

with $(\Delta R)_{ij} = \sqrt{(y_i - y_j)^2 + (\phi_i - \phi_j)^2}$ and k_{T_i} is the transverse energy of object i.

If the smallest distance is d_{ij}, the algorithm replaces object i and j with the combination of both and recalculates all distances. If the smallest distance is d_{iB}, the jet is removed from the list and added to the set of final jets. This will be repeated, until all four-momenta are removed from the list.

For the cluster algorithm, d_{ij} can be interpreted as distance between two objects and d_{iB} as distance between an object and the beam. R sets the resolution at which jets are resolved from each other. For large resolutions, the jets will become bigger and more energetic, since d_{ij} becomes smaller and more four-momenta will be combined to one reconstructed jet.

In this analysis, the anti-kT algorithm has been used as recommended by the ATLAS experiment. Using $p = -1$, for small distances ($\Delta R < R$), all objects (both soft and hard) are merged to one jet. For $R < \Delta R < 2R$, the energy of two hard objects is shared. Other variations of the cluster jet algorithm are the k_T algorithm with $p = 1$ and the Cambridge/Aachen algorithm with $p = 0$. In the first version, soft objects are handled first, either by merging with a nearby hard object or by being removed from the list as final soft jet. This results in the hardest objects being handled last. In the Cambridge/Aachen version, the k_T value for each object

is irrelevant and nearby objects will be combined first, while the final merging is done for the most distant objects.

Jet Reconstruction

At the ATLAS experiment, both SISCone and anti-kT jet finding algorithms have been used. For the data collected in 2010 and 2011, the anti-kT algorithm has been recommended with the choice of two R-values: 0.4 and 0.6. The jets are built from topological clusters and calibrated using global calibration factors. The clusters energies is reported at electromagnetic scale, which correctly accounts for the energy deposited in the Calorimeter by electromagnetic showers. The transverse momenta of all objects are required to be positive. As output, only final jets with $p_T > 10\,\mathrm{GeV}$ are considered. An alternative procedure at the ATLAS experiment is to use hadronic-calibrated clusters as input to the jet building algorithm (local calibration), without the need for further global calibration after the jet has been built.

For the resulting jets, differences between the energy of the jets as measured in the Calorimeter and jets at hardronic scale have been expected and observed [97]. Several detector effects are responsible for the mismatch, including energy loss in inactive regions (dead material), particles leaving the Calorimeter with non negligable energy (leakage) and energy deposits outside the reconstructed jets. The difference is compensated by the use of jet energy scale (JES) factors, which have been derived using comparisons between observed reconstructed jets and Monte

Carlo simulated truth jets. The systematic uncertainty has been evaluated to be between 2.3% and 5.3% depending on the jet η range for jets with p_T of 200 GeV, with slightly higher systematics for jets with higher transverse momentum. The highest systematic uncertainty between 4.1% and 13.8% has been observed for jets with p_T at 20 GeV.

An alternative procedure of estimating the JES in the low and moderate energy range (50 GeV $<$ jet p_T $<$ 700 GeV) is to consider the p_T balance of events that contain one photon and one jet. The p_T of the photon is well known, so that the jet energy can be estimated with good precision. At the time of writing, this analysis is being done on data collected during 2011. This is expected to reduce the jet energy scale uncertainty to below 1%.

For this analysis, jets from topological clusters with an R-value of 0.4 have been used, while locally calibrated clusters with the same R-value has been used for the jets in the MET calculation.

Muons

The muon reconstruction and identification algorithm is based on information from the muon spectrometer and the Inner Detector [69]. A typical muon leaves hits from which two tracks are reconstructed in each of the two subsystems. To derive the momentum and position of muons used in the calculation of the missing

transverse momentum, the tracks from both subsystems are combined and a global refit is performed.

Hadronically Decaying Taus

With a lifetime of 2.9×10^{-13} s, tau leptons decay before reaching the Inner Detector. 65% of taus decay hadronically, which results in a very similar signature to jets produced by strong interactions: one or three tracks in the Inner Detector and an energy deposit in the Calorimeter. In order to seperate hadronic taus from jets, identification methods based on the shower shape and the tracking characteristics have been developed [98]. They take advantage of the fact that energy deposits of hadronic taus have a low track multiplicity, are isolated and are narrower than energy deposits from QCD jets.

Missing Transverse Momentum

The missing transverse momentum (MET) is the negative vectorial sum of the energy of all particles transverse to the beam line. The sum of the energy is calculated by adding contributions from the Calorimeter cells and the muon tracks [99]. The Calorimeter covers a large range of η, which reduces the number of particles escaping in the forward region.

The calorimeter cells are associated to the reconstructed objects in order to use their calibration which have been determined with high accuracy. If a cell belongs to several objects, only the object of the type with the highest priority as described in the following list is considered: electrons, photons, hadronically decaying taus, jets and muons (decreasing priority). For each of the objects, the x- and y-component of the cells' energy is added separately. The total MET from cells is calculated by adding the energies from each particle type. In this analysis, the cell calibration used in the MET calculation corrects for the energy loss in the cryostat. Hence, during the MET calculations, the energy loss in the cryostat is not considered explicitly.

The contribution from muons is added to the energy of the calorimeter cells. The information from the muon spectrometer and the Inner Detector is combined to calculate the energy of the muon. The energy measured in cells in the Calorimeter which has been associated to a muon is subtracted from the muon's energy in order to avoid double counting.

CHAPTER VI

MONTE CARLO SIMULATION AND EVENT CHARACTERISTICS

At the ATLAS experiment, Monte Carlo (MC) simulations are used in order to make predictions based on various different models including the Standard Model (SM). Due to the large number of random variables in the interaction process, in the following particle decay and in the response of the detector, it is unfeasible to develop a deterministic algorithm describing the probability of all possible observations. However, predictions from theory are nevertheless needed in order to be compared to observations. An approximation of the prediction is produced by running a large number of trial runs (Monte Carlo simulations) using a broad set of random variables as expected in the particle production, the decay processes and the detector response.

The Monte Carlo simulation procedure is divided into the generation of events which includes all the information at the particle level (truth events), including their production and decay, and the simulation of the detector response and the readout electronics [100]. All properties at the particle level are labelled "truth". For the event generation, different generators have been used for both signal and background samples. The detector response is simulated with Geant4 [101], which

is used to simulate the passage of the particles through matter, including the LHC beam pipe and the entire ATLAS Detector. Using the response of the detector, the electronic readout is simulated, resulting in an output similar to the electronics' output for a real observed event. The same ATLAS software release is used for event reconstruction and object identification for MC events as for data.

Most of the samples are produced with the general event generators Pythia [102] and Herwig [103]. Both generators are able to produce a large number of SM processes including processes explained by the electroweak theory and by QCD. They produce the four vectors of the particles involved in the initial hard processes, the underlying event and secondary cascades. All SM particles are known to both generators and can be used in all processes. In addition, several extensions of the SM have been implemented in both generators.

Generators for specific phenomena have been developed, which are only capable of generating four-vectors of particles produced in a small number of specific processes. In order to allow them to take advantage of the large number of SM processes implemented in the more general generators like Pythia and Herwig, an interface has been defined by the Les Houches Accords [104]. It establishes a standard file format which stores the list of particles, including their position and states, produced in each event in order to transfer information between different generators. As a result, the cascade decay of secondary particles (particle shower) can be done in the general event generators.

The detailed list of all MC datasets used in this analysis are shown in appendix A.

Quantum Black Hole Signal Samples

The generator used for producing four-vectors of quantum black holes decaying to two particle final states is the newly developed generator QBH [105]. The particle showering is done in Pythia 8 [106]. Various parameters can be set, including the following:

- Types of the colliding particles (gluon/gluon, quark/quark, quark/gluon, all)
- Electric charge of the BH
- Fundamental Planck mass M_{Pl}
- Minimum allowed BH mass M_{TH}
- Maximum allowed BH mass M_{max}
- Whether or not trapped surface calculation is included. The fact that not all of the energy of the colliding particles is trapped inside the BH may or may not be considered.
- Type of extra dimensions (ADD or RS)
- Total number of ADD-type dimensions

- Center-of-mass energy

All other variables are set to their default values (see [105] for details).

Changes in the Planck mass and in the type and number of extra dimensions do not change the event characteristics of BH events (see figures 6.1. and 6.2.[1]). This includes the $\Delta\phi$ distribution, which peaks strongly at π for any parameter settings of QBH. Therefore, only MC samples with different minimum BH masses (M_{TH}) and electric charges have been produced. The Planck mass is fixed at 1 TeV, the type of extra dimension is set to ADD and the number of total dimensions is assumed to be 10 for all samples. In addition, trapped surface calculations are not considered, since they are associated with a large theoretical uncertainty. The fact that only part of the energy of the colliding partons is trapped inside the BH is only expected to change the cross section and the distribution of the invariant mass, leading jet p_T and leading electron p_T. In figure 6.3. it is shown that the minimum BH mass is higher in events that include the trapped surface calculations, which results in a lower cross section. The selection requirement on the jet and the electron p_T is chosen to be very loose, so that the acceptance for simulated events with trapped surface calculations is expected to remain unchanged for the appropriate final invariant mass selection. The remaining variables used in the selection process are not affected by the trapped surface calculations (see figure 6.4.). Hence, the

[1] All figures in this dissertation showing simulated or observed distributions of physical quantities were produced using the ROOT framework [107].

analysis at higher mass points is sensitive to black holes of lower M_{TH}, produced from two partons which loose part of their energy during the production process.

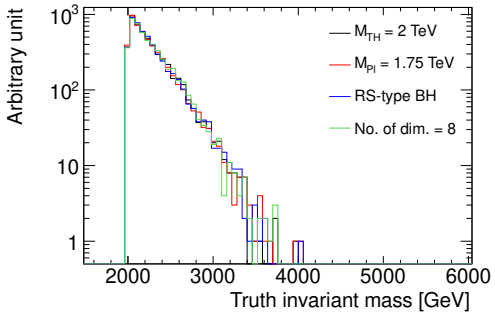

(a) Truth BH invariant mass

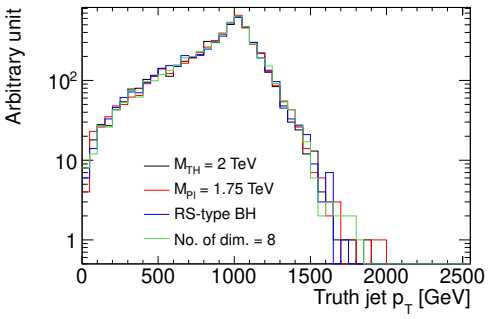

(b) Truth jet p_T

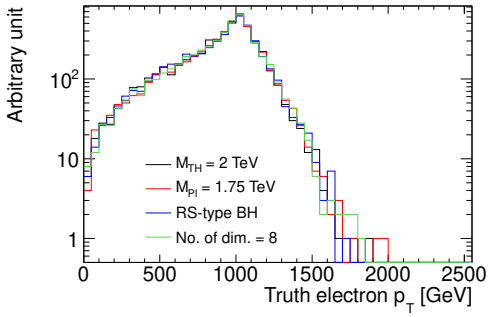

(c) Truth electron p_T

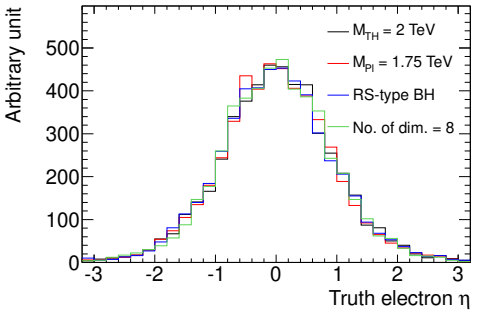

(d) Truth electron η

Figure 6.1. Comparison of different quantum BH models. Truth BH invariant mass, truth p_T of BH decay products (jet and electron) and truth electron η are shown for different variations of the signal parameters. The default distribution with $M_{TH} = 2\,\text{TeV}$ is given in black. The following variations have been studied: Increase of M_{Pl} from 1 TeV to 1.75 TeV (red), change of the type of extra dimensions from ADD to RS (blue) and decrease of the total number of dimensions from 10 to 8 (green). No change in event characteristics is observed. All distributions are normalized to the same number of events.

For black holes with with an electric charge of 4/3, only quark-quark interactions

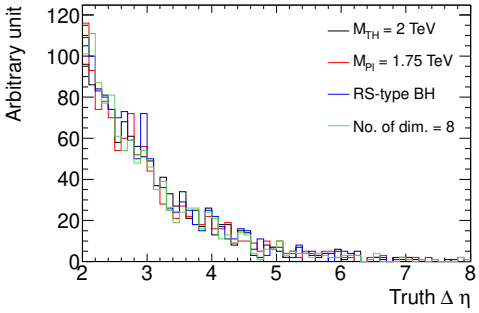

(a) Truth $\Delta\eta$ electron/jet

Figure 6.2. Truth $\Delta\eta$ for different BH signal parameters. $\Delta\eta$ is the absolute difference between η of the leading electron and the leading jet. The default distribution with $M_{TH} = 2\,\text{TeV}$ is shown in black. The following variations have been studied: Increase of M_{Pl} from 1 TeV to 1.75 TeV (red), change of the type of extra dimensions from ADD to RS (blue) and decrease of the total number of dimensions from 10 to 8 (green). No change in event characteristics is observed. All distributions are normalized to the same number of events.

(q-q) are considered as initial state. All other initial states are forbidden by charge conservation. The initial states q-q and quark-gluon (q-g) could both create black holes of charge 1/3. However, from a theoretical point of view, there is no Lorentz invariant operator that can connect the interaction quark+gluon→lepton+quark (three fermions and a gauge boson). Since Lorentz invariance is assumed for this analysis, only the initial state q-q is considered for BHs with charge of 1/3.

For each of the different black hole parameters, one sample has been produced (see table 6.1. for details). Except where explicitly mentioned, all numbers and figures are for a signal sample of charge 4/3 with a minimum mass of $M_{TH} = 2\,\text{TeV}$.

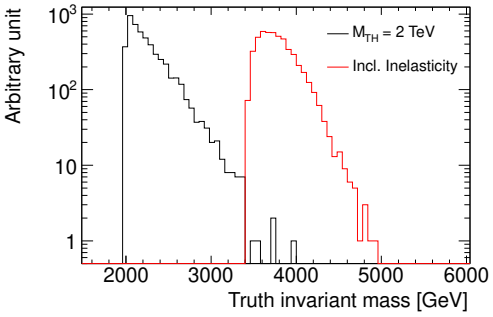

(a) Truth BH invariant mass

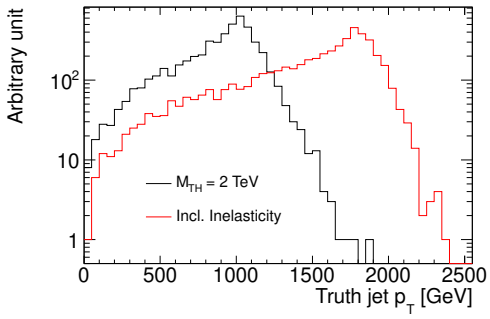

(b) Truth jet p_T

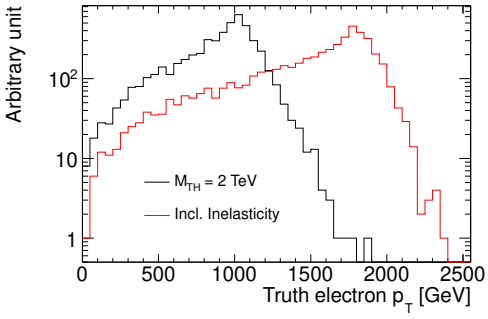

(c) Truth electron p_T

Figure 6.3. Study of trapped surface calculations (1). Truth BH invariant mass and truth p_T of BH decay products (jet and electron) are shown for QBH signal events with and without trapped surface calculations (labelled "Inelasticity"). The minimum BH mass M_{TH} is 2.0 TeV for both samples. All other parameters are set to their default value.

Signal Event Characteristics

The characteristics of BH decays have been studied using the MC samples produced with QBH. The specific properties of the BH decay depends on the

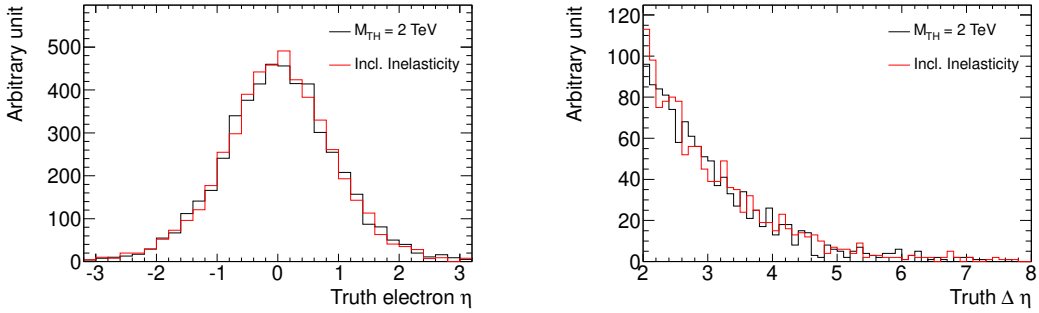

(a) Truth electron η

(b) Truth $\Delta\eta$ electron/jet

Figure 6.4. Study of trapped surface calculations (2). Truth electron η and $\Delta\eta$ distributions are shown for BH signal samples with and without trapped surface calculations (labelled "Inelasticity"). Both distribution are produced with $M_{TH} = 2\,\text{TeV}$. All other parameters are set to their default values.

BH electric charge	M_{TH}	decay channel	cross section	number of events
4/3	1.5 TeV	ss electron+jet	1336 pb	5000
4/3	2 TeV	ss electron+jet	361 pb	5000
4/3	3 TeV	ss electron+jet	28 pb	5000
4/3	4 TeV	ss electron+jet	1.1 pb	5000
4/3	4.5 TeV	ss electron+jet	0.14 pb	5000
4/3	5 TeV	ss electron+jet	0.011 pb	5000
1/3	3 TeV	os electron+jet	14 pb	5000

Table 6.1. List of MC signal samples produced containing events with quantum black holes decaying to electron plus jet (ss - same sign, os - opposite sign). For the cross section calculation, it was assumed that all energy of the colliding partons is trapped inside the BH.

assumption of a minimum BH mass (M_{TH}), but the general event characteristics are similar for a wide range of the parameter space. In this section, distributions are shown for a fundamental Planck mass M_{Pl} of 1 TeV, minimum BH masses

M_{TH} between 2 and 5 TeV and an electric charge of either 4/3 or 1/3, produced in collisions of two up-quarks or one up-quark and one down-quark, respectively.

For this analysis, quantum black holes are assumed to decay to two particle final states only. The electron + jet decay channel results in events with one electron and one jet, both carrying a large transverse momentum. Figure 6.5. shows the distribution of the combined truth mass of the electron and the jet and the truth p_T of each decay product. Due to the rapidly falling PDF, most of the quantum BHs are created close to M_{TH}. For both decay products, the p_T distribution peaks at half the minimum BH mass with a long tail to the left side of the momentum spectrum. Due to its high mass the BHs decay very central, resulting in small pseudo-rapidities as can bee seen in figure 6.6.(a). The boost of BHs is small compared to their high mass. This is observed in large values of $\Delta\phi$, corresponding to back-to-back decays (figure 6.6.(c)). In this analysis, $\Delta\phi$ is defined as:

$$\Delta\phi = \begin{cases} |\phi_{jet} - \phi_{electron}| & \text{if } |\phi_{jet} - \phi_{electron}| \leq \pi, \\ |\phi_{jet} - \phi_{electron} - 2\pi| & \text{else} \end{cases}$$

Finally, the $\Delta\eta = |\eta_{jet} - \eta_{electron}|$ distribution peaks at small values with a tail up to 5 (see figure 6.6.(b)).

Background Sources

Among the main background sources are events that contain at least one high

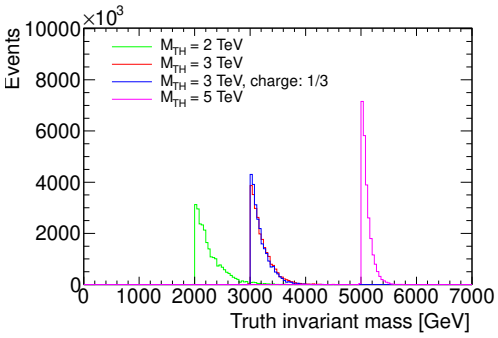

(a) BH invariant mass

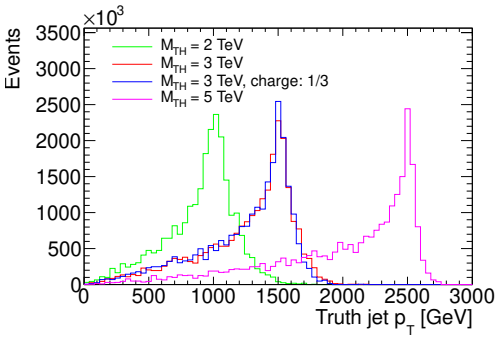

(b) jet p_T

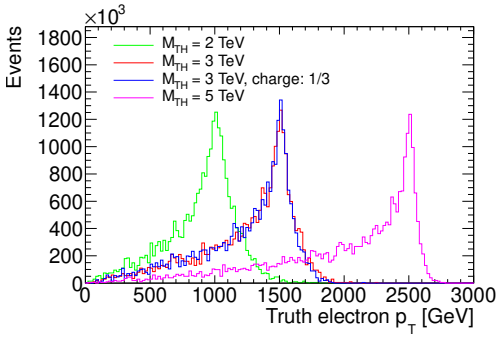

(c) electron p_T

Figure 6.5. Signal MC truth distributions (1). Truth BH invariant mass and truth p_T of BH decay products (jet and electron) are shown for multiple BH signal samples. The distributions are for BHs of charge 4/3, except where mentioned. Trapped surface calculations are not considered. The distributions of $M_{TH} = 3\,\text{TeV}$ with a BH charge of 4/3 and 1/3 overlap for each quantity shown.

p_T electron and one high p_T jet. This includes events with a boosted W-boson or Z-boson produced in association with one or more jets. These events can contribute to the background via direct decays to electrons and via decays to tau leptons which then decay further to electrons (see figure 6.7. for some typical processes).

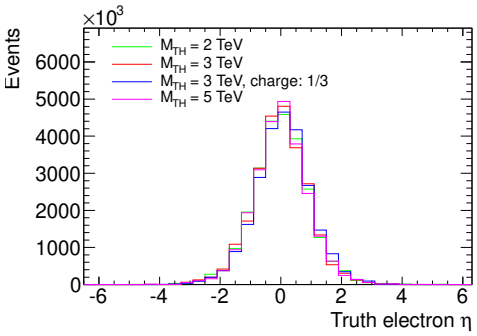

(a) electron eta

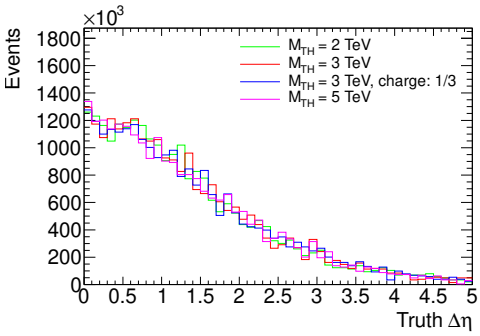

(b) $\Delta\eta$ electron/jet

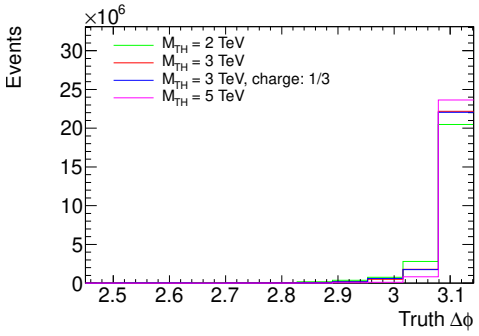

(c) $\Delta\phi$ electron/jet

Figure 6.6. Signal MC truth distributions (2). Truth electron η, $\Delta\eta$ and $\Delta\phi$ distributions are shown for several BH signal samples. The distributions are for BHs of charge 4/3, except where mentioned. Trapped surface calculations are not considered.

In addition, semi-leptonic and full-leptonic $t\bar{t}$ events and single top events decaying leptonically can have a signal-like signature (see figure 6.8.).

QCD events that contain at least two jets, where one jet is misidentified as an electron, are another source of background. This includes light quarks and gluons produced in QCD hard scattering processes and soft gluon radiation. The likelihood

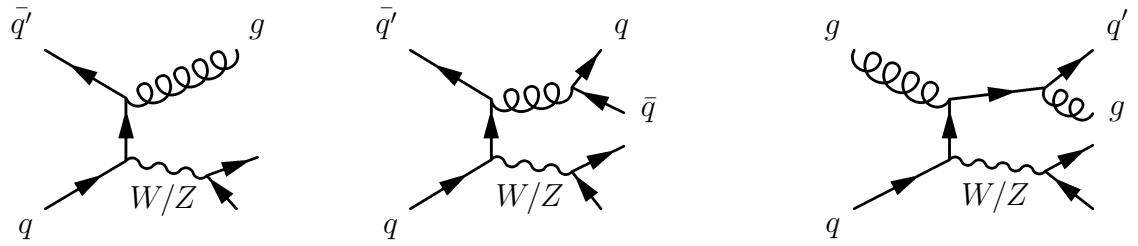

(a) W/Z-boson + 1 jet

(b) W/Z-boson + 2 jet from quark/quark interactions

(c) W/Z-boson + 2 jet from quark/gluon interactions

Figure 6.7. Feynman diagrams for W/Z-boson background processes. The precise type and charge of the quarks involved depends on the production of either an W^+-, W^-- or Z-boson. W-bosons decaying further to an electron/tau and a neutrino and Z-bosons can decaying to two electrons or taus contribute to the background.

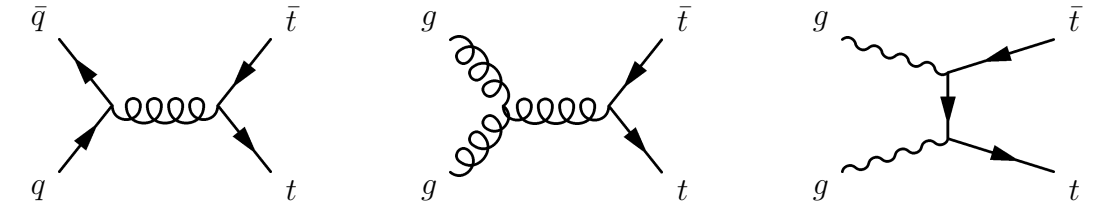

(a) $t\bar{t}$ production via quark-antiquark annihilation

(b) $t\bar{t}$ production via gluon fusion (s-channel)

(c) $t\bar{t}$ production via gluon fusion (t-channel)

Figure 6.8. Feynman diagrams for $t\bar{t}$ background processes (leading order). Each top particle can further decay to a W-boson and a b-quark. The W-boson decays either hadronically to two partons or leptonically to one lepton and one neutrino. All combinations of production and decay channels contribute to the background.

for a given parton jet to be identified as electron is very small, but due to the large jet production cross section QCD events have a significant impact on the final event count. In addition, the cross section decreases much slower with increasing energy compared to other background sources, which results in QCD events becoming the dominate background at very high energies. Another source of high-p_T multi-jet

events which can fake an electron are events with a full hadronically decaying top pair (see figure 6.8.).

The third potential source of background are events with two high p_T electrons, of which one electron is reconstructed as a jet. This includes di-boson events, such as events with two W-bosons, two Z-bosons or one W- and one Z-boson (see figure 6.9.).

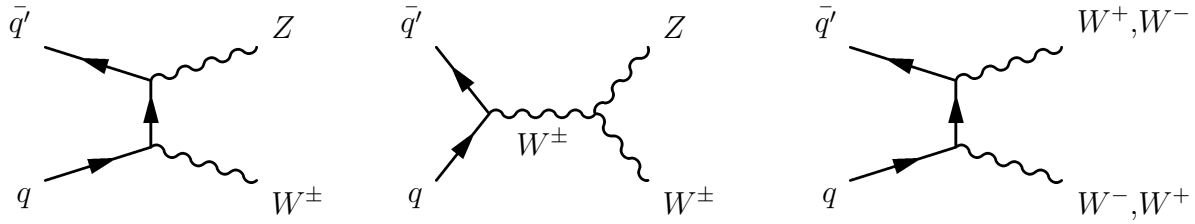

(a) WZ production, t-channel (b) WZ production, s-channel (c) WW production

Figure 6.9. Feynman diagrams for di-boson background processes. Each W-boson can further decay hadronically to two partons or leptonically to one lepton and one neutrino. The Z-bosons can decay to two fermions. All combinations of production and decay channels potentially contribute to the background.

Due to the large uncertainty in MC simulations with events dominated by the strong interaction (QCD events), the QCD background is estimated using a data-driven technique. For all other background sources (non-QCD events), MC simulated events are used which are normalized in a signal-free control region.

Background Samples

Several MC simulated samples have been produced for background studies with various generators.

QCD Events

The contribution of events that are dominated by the strong interactions (QCD events) is estimated using a data-based method. In order to estimate the reconstructed electron η distribution in QCD events, a sample with QCD events has been produced using Pythia with the PDF set MRST2007LO* [108]. The sample is filtered, requiring a reconstructed electron with p_T above 240 GeV.

W/Z + Jets Events

Events containing $W \rightarrow e\nu/\tau\nu$ and a $Z \rightarrow e^+e^-/\tau^+\tau^-$ have been generated with Alpgen [109] interfaced with Herwig [103] and Jimmy [110]. The PDF set CTEQ6L1 [17] has been used. Exclusive samples with events with zero to four additional light partons have been produced. In addition, inclusive samples with five and more light partons for each channel are used in the analysis.

$Z \rightarrow e^+e^-$ Events

In order to estimate the systematic uncertainty for the signal acceptance, an additional, inclusive sample of $Z \rightarrow e^+e^-$ events has been generated with Pythia using the PDF set MRST2007LO*.

$t\bar{t}$ Events

$t\bar{t}$ events have been generated with MC@NLO 3.41 [111] [112] interfaced with Jimmy and Herwig. The top mass is set to 172.5 GeV. Two samples are used: One for hadronic-only decays and one for decays with at least one electron. Both have been produced using the PDF set CTEQ6.6 [18].

Single Top Events

The samples for single top events have been generated with MC@NLO 3.41 interfaced with Jimmy and Herwig [113]. CTEQ6.6 has been used as PDF set. For the electron decay, different samples have been produced and used for the s- and the t-channel.

Di-Boson Events

Samples for di-boson events (WW, ZZ and WZ) have been produced with Herwig using MRST2007LO* as PDF set.

$b\bar{b}$ and $c\bar{c}$ Events

The $b\bar{b}$ and $c\bar{c}$ samples have been produced with Pythia. They are filtered to contain at least one electron with $p_T > 15\,\text{GeV}$ at the generator level. For both samples, the PDF set MRST2007LO* has been used.

CHAPTER VII

OBJECT DEFINITION AND EVENT SELECTION

This chapter describes the selection of events from the set of recorded events and from MC samples. Used throughout the analysis, different objects are defined and corrections to their nominal reconstructed properties are given. In addition, variations to the event weight are described. Finally, various regions used in this analysis are defined, including the signal region and different control regions.

Data Samples

The data that are used in this analysis were collected between March and August 2011 with the ATLAS Detector. They cover the periods B-K of proton-proton collision at a center-of-mass energy of 7 TeV corresponding to $2.29\,\mathrm{fb}^{-1}$. Both data and Monte Carlo simulations have been reconstructed and objects identified with the same release. For an overview over all data and MC samples used in this analysis see appendix A.

Trigger

In all signal and control regions used in this analysis, either one reconstructed electron or photon is required. In order to analyze the full amount of data available, the lowest unprescaled triggers for electrons and photons have been used. At L1, the trigger towers of the EM Calorimeter and the Hadronic Calorimeter are constructed [114]. They are defined to be the sum of all cells over the full depth in each calorimeter in a region of $\Delta\eta \times \Delta\phi = 0.1 \times 0.1$. A Sliding Window Algorithm as described above is used to find local energy maxima of 4×4 towers. The event is accepted by the L1 electron and photon trigger if two requirements are met: The 2×2 core cluster of the 4×4 towers is a local maximum (in order to avoid double counting) and the most energetic 2×1 or 1×2 pair of towers inside the core cluster is above a given threshold. The L2 electron and photon trigger is seeded by the L1 result, where the full granularity of the detector is used inside the region of interest. Using the layers of the EM calorimeter, shower shape variables are used to identify electron and photon candidates. For the electron trigger, tracks are reconstructed in the Inner Detector and a match to the electromagnetic cluster is required. The EF selection is very similar to the offline reconstruction algorithm already described. It includes requirements on the shower shape variables and vetos on hadronic leakage.

All events considered in this analysis are required to either pass an electron

trigger optimized for electrons with a transverse momentum above 22 GeV (EF_e22) or a photon trigger optimized for photons with transverse momentum above 80 GeV (EF_g80). Since the photon trigger does not veto clusters with associated tracks, electrons with a transverse momentum above 80 GeV pass the photon trigger with high efficiency. The trigger is used for all signal and control regions where an electron, loose only electron or photon with a transverse momentum above 85 GeV is required. Since the turn-on curve increases sharply for electrons and photons at 80 GeV, the efficiency of the photon trigger is expected to be close to 100%. For the $Z \rightarrow e^+e^-$ region, which requires electrons with transverse momentum only above 25 GeV, the electron trigger is used, which is expected to be very efficient for the electrons of lower transverse momenta.

The triggers are required both in the observed events and in MC simulated events. Due to small differences between the simulation result and the observed data, difference in efficiency between MC and data are observed. They are corrected by reweighting MC events based on the electron and photon scale factors derived from 2011 data as a function of electron η and photon η, respectively. For electrons, the difference between MC and data due to the trigger selection is between 1.5% and 0.3% depending on the electron η with an average uncertainty of 0.4 pp.

Object Definition

There are a number of objects that are used throughout the analysis. The principle objects are electrons, loose only electrons, photons and jets (see table 7.1. for an overview of the object definitions).

Medium and Loose Only Electrons

Electrons are standard reconstructed electrons passing the medium identification requirements. Most of the electrons in the signal MC pass any of the three default electron identification requirements (loose, medium and tight). However, the usage of tight ID requirement is not optimized for high p_T objects. Hence, in order to allow for a large uncertainty on the detector response for signal events, the medium level identification is used for electron selection. Due to the centrality of the high-mass signal events, only electrons in the barrel region with absolute η smaller than 1.37 are accepted.

Energy scale corrections have been applied at the cell level during the reconstruction of electrons. However, detailed study of the data used in this analysis have shown the need for additional corrections. The correction factors have been determined as a function of electron η in an analysis of $Z \rightarrow e^+e^-$ events [115] [116]. They are up to 0.5% of the electrons energy and are applied to each electron. Figure 7.1. shows the $Z \rightarrow e^+e^-$ invariant mass distribution after the additional energy calibration corrections have been applied.

The energy resolution of electrons in data have not been exactly reproduced in MC simulations. Hence, an additional smearing is applied to the electrons' energy in MC simulations as a function of electron η and p_T, resulting in the same resolution as observed in data. After all corrections, an electron is required to have a transverse momentum above 25 GeV and an absolute η of less or equal 1.37 (barrel region only).

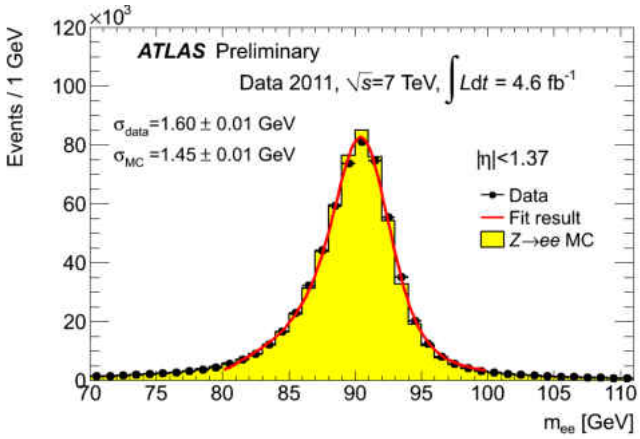

Figure 7.1. $Z \to e^+e^-$ invariant mass distribution after all energy scale corrections have been applied [116]. The method for retrieving the fit is described in [115].

As defined by the detector geometry, for most electrons a b-layer hit is expected. If a b-layer hit is expected, but none is observed, the electron is rejected. This reduces the number of fake electrons coming from photon conversions, which overwhelmingly convert after passing the first layer of the Inner Detector and thus don't leave a hit there. The electrons are then sorted by their transverse momentum. The "leading electron" is the electron with the highest transverse

momentum, while the "second leading electron" is the electron with the second highest transverse momentum.

The requirement for loose only electrons is the same as for electrons with the exception that loose only electrons are required to pass the loose, but are not allowed to pass the medium identification selection. This results in a sample of loose only electrons with no overlap with the default electron sample. In addition, loose only electrons are not required to have a b-layer hit. The loose only electrons are also sorted by their transverse momentum, resulting in a "leading loose only electron" and a "second leading loose only electron".

The efficiency of the electron reconstruction and identification algorithms have been estimated by separate studies at the ATLAS experiment [115]. Due to differences in various quantities between the simulations and the observed data, different efficiencies in data and MC have been observed. In order to correct for them, scale factors have been derived for electrons as a function of electron p_T and electron η. The MC samples have been reweighted using these scale factors for 2011 data. For the reconstruction algorithm, the difference between MC and data is between -0.2% and +0.9% depending on the electron η region with an average uncertainty of 0.7 pp. The difference for the electron identification algorithm depends on both the electron η and p_T. For electrons with $p_T > 45\,\text{GeV}$, as relevant for this analysis, the maximum difference is 2.7%, while the minimum difference is 0.2%. The uncertainty on the scale factors is on average 0.9 pp.

Photons

Photons are defined as standard reconstructed photons passing the loose identification requirement. In addition, photons are required to have an absolute η of less than 1.37 (barrel only) and a transverse momentum larger than 25 GeV. As for electrons, energy scale corrections for photons have been applied to data. The photon energy resolution is corrected for discrepancies in the energy scale between data and MC.

Isolation

As isolation criteria for any of the defined objects (electrons, loose only electrons and photons), the sum of energy depositions in a cone of 0.4 in $\Delta R = \sqrt{\Delta\phi^2 + \Delta\eta^2}$ around the object is used. The energy sum is corrected for leakage of the object's energy into its isolation cone, making the isolation independent of the object's transverse momentum. In order to prevent the signal acceptance to be very sensitive to the electron isolation, an isolated object is defined as having less than 15 GeV energy deposited in the isolation cone.

Jets

A jet is reconstructed by the anti-Kt jet algorithm with a k-value of 0.4 using topological clusters as input. Jets are required to be in the η range between -2.47 and 2.47 and to have a minimum transverse momentum of 25 GeV. If a leading electron, loose only electron or photon exists, a jet is rejected if it is closer than 0.4 in ΔR to the leading object. The distance to the second leading object is

not considered. This is done separately for electrons, loose only electrons and photons, resulting in three different jet collections which are used in combination with the corresponding objects. Finally, jets are rejected that pass a set of rejection requirements which are optimized to remove jets caused by hardware problems, unusual LHC beam conditions, cosmic ray showers and other sources not related to real energy deposits in the calorimeter. The remaining jets are sorted by their transverse momentum in order to obtain a "leading jet", a "second leading jet" and a "third leading jet".

Missing Transverse Energy

The missing transverse energy (MET) is calculated as the negative vectorial sum of the transverse momenta of all reconstructed objects. During some of the data taking, six front end boards (FEBs) of the LAr subdetector were lost, resulting in a hole in the output of the LAr Detector in a small $\eta \times \phi$ region. In affected events, the electrons and photons in the region are ignored for the MET calculation (see below for details of the LAr treatment). Since affected events with a jet in this region are completely rejected, no additional consideration for MET calculations are needed.

Basic Event Selection and Event Reweighting

This section describes the basic selections that are used to produce samples

with clean collision events used throughout the analysis, including for the signal selection, the selection of control samples and for background studies. Any additional selections on top of the basic requirements are described in the relevant sections.

In order to select events for which the full detector information is available, only events are considered for which all necessary detector subcomponents were active and working properly. This is guaranteed by monitoring the different subcomponents during data-taking and by specific controls of the recorded data, both before and after reconstruction and identification algorithms are executed.

In order to get clean events containing particles produced during collisions, only events with at least one reconstructed vertex with at least three associated tracks are considered.

In events recorded with the ATLAS Detector, particles produced in different primary beam particle interactions can cross the detector at the same time or with a time lag smaller than the detector response time (pileup). They are included in the read-out of the detector, which can represent a signficiant background to the physics event of interest. In addition, various meassured quantities can be affected due to the overlapping detector response of particles from different interactions. Pileup can be divided into two categories: in-time and out-of-time pileup. In-time pileup is caused by multiple interactions during the same bunch crossing due to a high instantaneous luminosity. The number of multiple interactions follow a Poisson

distribution with a mean value that depends on the instantaneous luminosity. The instantaneous luminosity changes constantly during data-taking resulting in a constant change of in-time pileup. The out-of-time pileup is a result of interactions in consecutive bunch crossings due to a non-zero detector response time. Out-of-time pileup depends on the precise bunch setup of the LHC which is usually constant over short period of times, but which has been changed several times during the 2011 data taking. The effect of in-time and out-of-time pileup has been simulated during the production of the MC samples, but since the exact running conditions were unknown during production, there is still a significant difference when compared to data. In order to accommodate for the differences, the MC samples have been reweighted such that the distributions of the average number of pileup interactions over all bunch crossings in data and MC agree during short periods of nearly constant instantaneous luminosity.

For data corresponding to an integrated luminosity of $0.95\,\mathrm{fb}^{-1}$, six front end boards (FEBs) of the LAr Detector were not working, which affects the energy measurement of electrons, photons and jets in a particular region of the detector. This has been corrected, by rejecting electrons and photons in the affected η and ϕ region. The MET is calculated without the rejected objects. If a jet with transverse momentum above 40 GeV falls into this region, the whole event is rejected. The MC samples have been divided into two parts corresponding to an integrated luminosity

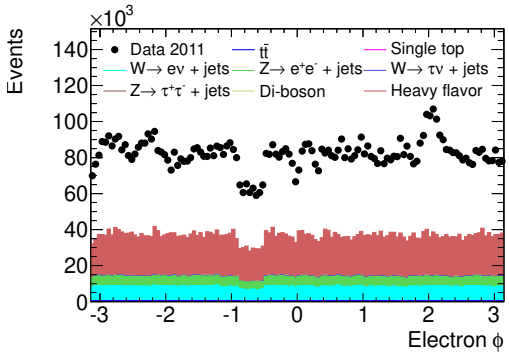

Figure 7.2. ϕ of leading electron after basic event selection (events with one electron and one jet) for data and non-QCD MC. The lower event count in the region of the LAr problem can be observed in data and MC. No MC QCD contribution is shown which results in the difference between MC prediction and observation.

with and without the lost FEBs. In the sample corresponding to data without the six FEBs, the same method as in data is applied (see figure 7.2.[1]).

Region Definition

Different regions have been defined for various tasks. Containing electrons plus jet events with high invariant mass, the signal region is expected to contain most of the potential signal events (see below for a detailed description). The loose only signal region with loose only instead of medium electrons is used to estimate the QCD contribution in the signal region. The signal-free low invariant mass control region and the low loose only invariant mass control region both apply

[1] In all one-dimensional histograms a showing data to MC comparison, the different MC contributions are stacked. If not mentioned explicitly, no QCD contributions are shown, resulting in a discrepancy between simulated and observed distributions.

a lower invariant mass selection of 400 GeV. They are used to estimate the ratio of QCD events with a medium and a loose only reconstructed electron at lower invariant masses. In addition, the non-QCD MC samples are normalized in the low invariant mass region. The systematic uncertainty of the QCD estimation technique is measured with the low loose photon invariant mass control region where the electron requirement in the low invariant mass region is replaced by a loose photon requirement. In order to study events containing medium electrons with high invariant mass, but without potential signal contribution, the sub-signal control region has been defined with invariant masses between 800 GeV and 1 TeV. Finally, for studies on systematic uncertainties related to the signal region selection, the $Z \rightarrow e^+e^-$ control region is used. For an overview of all selection requirements for each region see table 7.2.

Signal Region Selection

In order to select signal-like events, the following selections are made: First, in order to select high-p_T electron+jet events, the leading electron and the leading jet are required to have a transverse momentum of at least 85 GeV and 100 GeV, respectively. In addition, back-to-back events are selected by requiring the absolute difference between ϕ of the leading electron and the leading jet ($\Delta\phi$) to be above $\pi/2$. This removes a significant fraction of events with three or more objects

dominated by QCD events. In order to reject QCD events in high η and high $\Delta\eta$ region, only events with $\Delta\eta$ between the leading electron and leading jet smaller than 1.5 are kept. All events in which the leading electron is not isolated are rejected. The isolation requirement is chosen to be very loose in order to allow for large uncertainties in the signal model. Finally, the leading electron and the leading jet are required to have a combined invariant mass (invariant mass) of 90% of M_{TH} of the model under consideration. Table 7.3. shows the number of observed events passing the various selections. The number of events in each MC sample passing the selection requirements are shown in appendix B. Figures 7.3. and 7.4. show the distribution of variables corresponding to all selection criteria for the signal region before they are applied for data, electroweak MC and signal MC.

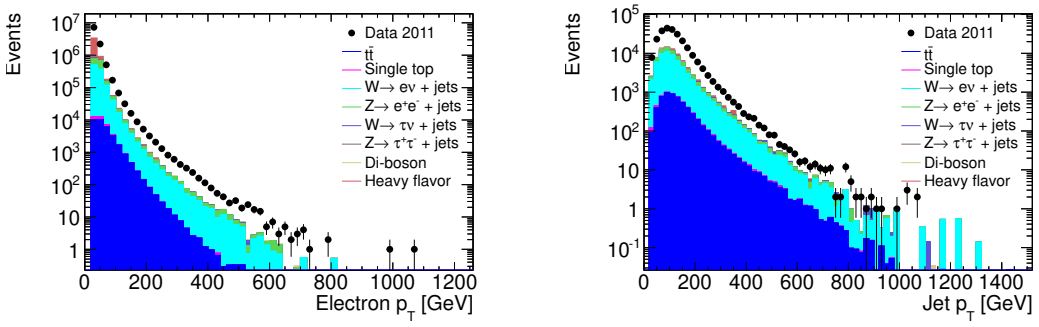

(a) Leading electron $p_T > 85\,\text{GeV}$ (b) Leading jet $p_T > 100\,\text{GeV}$

Figure 7.3. p_T of the leading electron and p_T of leading jet are shown before the corresponding selection criteria are applied. Only events that pass all previous selection criteria are used. Distributions are shown for electroweak MC, signal and data. No MC QCD contribution is shown which results in the difference between MC prediction and observation.

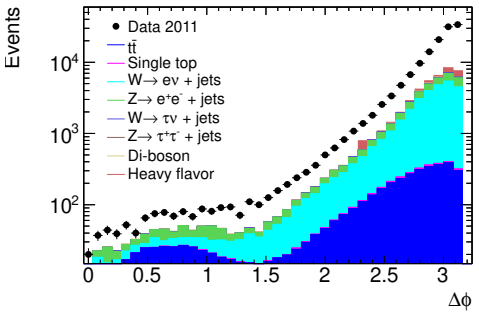

(a) $\Delta\phi$ of leading electron and leading jet

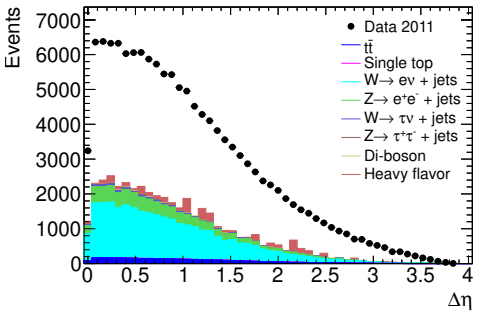

(b) $\Delta\eta$ of leading electron and leading jet

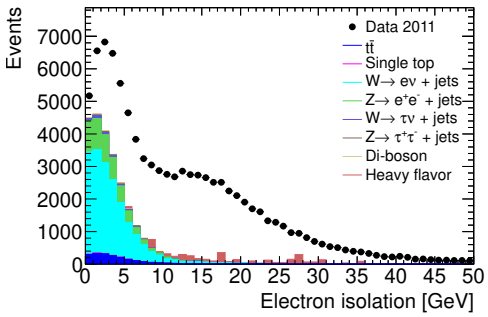

(c) Leading electron isolation

Figure 7.4. $\Delta\phi$, $\Delta\eta$ and electron isolation distributions before the corresponding selection criteria are applied. Only events that pass all previous selection criteria are used. Distributions are shown for electroweak MC, signal and data. No MC QCD contribution is shown which results in the difference between MC prediction and observation.

$\Delta\phi$ Selection

Since BHs only decay to two final particles and due to their high mass, the two decay products are expected to be back-to-back. In signal MC, it can be seen that the events peak strongly at very high $\Delta\phi$ (see figure 6.6.(c)), while for electroweak

events and QCD events with more than two jets, the peak is expected to be less pronounced (see figure 7.4.(a)). However, there is a large uncertainty on $\Delta\phi$ in signal samples that were produced with Pythia (see figure 11.2.(a)). Hence, it was decided to apply a rather loose $\Delta\phi$ cut of $\pi/2$, which results in a slightly larger background than for a tighter cut, but reduces the systematic uncertainty on the signal acceptance significantly.

$\Delta\eta$ Selection

As can be seen in figures 7.4.(b) and 6.6.(b) and table 7.3., the additional improvement in selecting signal events while rejecting background achieved by the $\Delta\eta$ selection is not very large. The selection requirement based on $\Delta\eta$ is nevertheless included due to the bad background estimation result for events with high $\Delta\eta$. In figure 7.5., it can be seen that removing this selection results in a significant underestimation of the QCD background in the signal region at high $|\eta|$. The expected background as shown in these figures is estimated using the technique described in the following chapters. The excess at high $|\eta|$ is especially pronounced when also removing the isolation selection on the leading electron (see figure 7.6.). The same feature can also be seen in Pythia QCD MC events (figure 7.7.), which shows that there is a peak at high electron η both when selection loose only electron plus jet events and for medium electron plus jet events. In addition, it can be seen that the peak is stronger for medium electrons. This results in the underestimation of medium electrons plus jet events using events with loose only electrons. To

confirm that this is also seen in data in non-signal regions, the $\Delta\eta$ vs. electron η distribution has been studied for the following three regions where no signal is expected: A region with a lowered invariant mass cut (800 GeV < invariant mass < 1 TeV) as shown in figure 7.8.(a), the loose only sub-signal region (figure 7.8.(c)) and the loose only signal region (see figure 7.8.(b)). In all three regions, there is an accumulation of events in the high electron η, high $\Delta\eta$ region. Those events pass the medium electron identification algorithm with a higher probability at higher invariant masses, resulting in an underestimation of background events. In order to remove these additional QCD events, $\Delta\eta$ is required to be below 1.5.

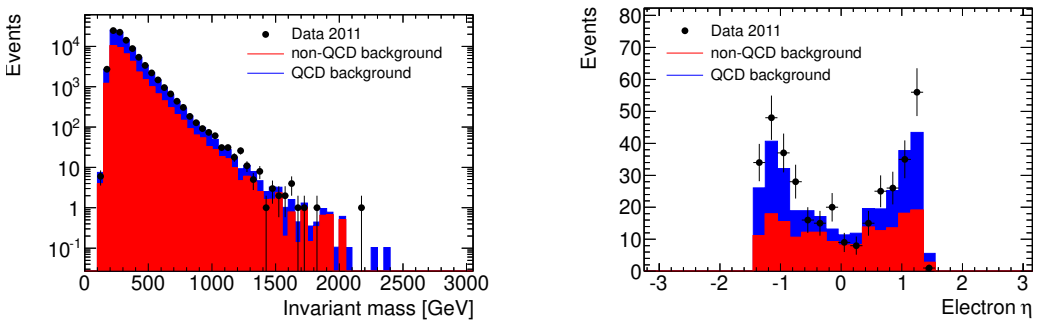

(a) invariant mass of electron/jet

(b) electron η

Figure 7.5. Signal region distributions without $\Delta\eta$ selection. Distribution of electron η and invariant mass of electron and jet in the signal region without selection requirement for $\Delta\eta$ are given. For the plot showing the invariant mass, no invariant mass selection has been made. The electron η distribution only shows events with invariant mass above 900 GeV. The background is estimated using the technique described in the following chapters.

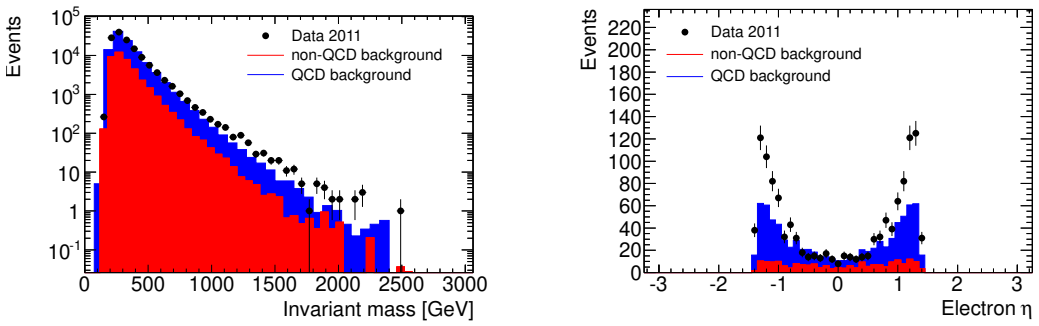

(a) invariant mass of electron/jet

(b) electron η

Figure 7.6. Signal region without $\Delta\eta$ and isolation selection. Distribution of electron η and invariant mass of electron and jet in the signal region are given without any selection requirement for $\Delta\eta$ and electron isolation. For the plot showing the invariant mass, no invariant mass selection has been made. The electron η distribution only shows events with invariant mass above 900 GeV. The background is estimated using the technique described in the following chapters.

Electron Isolation Selection

In order to reject a significant amount of QCD background, a very loose electron isolation is required. The isolation is calculated in a cone of 0.4 around the electron and is corrected for energy of the electron leaking into the cone. Therefore the electron isolation is independent of the electrons' energy. In order to allow for the uncertain behavior of electrons in the very high energy regime (above 1 TeV), a very loose isolation requirement of 15 GeV has been selected. In figure 7.9., one can see the isolation vs p_T for the leading electron in $Z \rightarrow e^+e^-$ events. In this pure sample of electrons, the acceptance of a 15 GeV selection is very high. The correlation between the electron isolation and p_T is either very small or zero, so

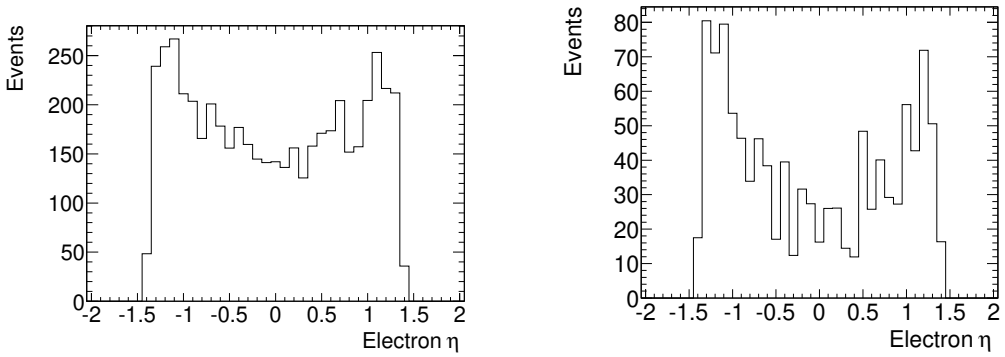

(a) loose only electrons

(b) medium electrons

Figure 7.7. Electron η in Pythia QCD MC events with one electron and one jet. No further selections are made. One can see the peak at high eta both when selecting medium and loose only electrons. The peak is more pronounced in the distribution with medium electrons.

that a similar behavior is expected for electrons with p_T above 1 TeV. In addition, for events in the low loose only invariant mass region, which are dominated by electrons faked by jets produced by the strong interaction, a significant amount of events contain electrons with an isolation above 15 GeV (see figure 7.10.), which are rejected by the isolation cut.

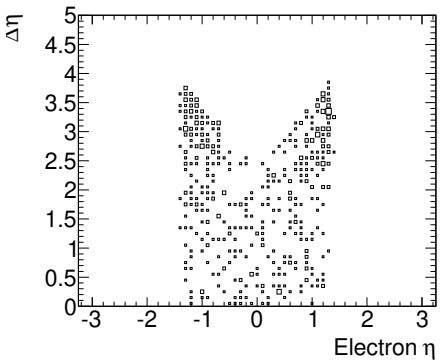

(a) 800 GeV < invariant mass < 1 TeV

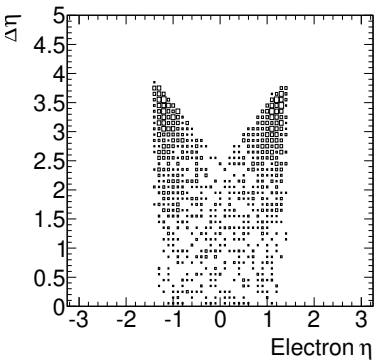

(b) Loose signal region

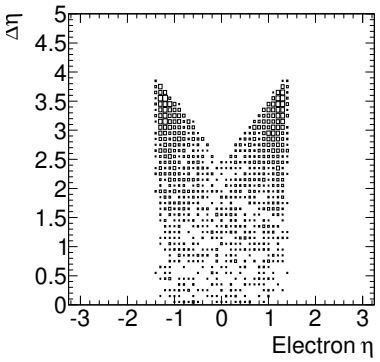

(c) Loose sub-signal region

Figure 7.8. $\Delta\eta$ vs. electron η in non-signal regions. The regions shown are the sub-signal region (with 800 GeV < invariant mass < 1 TeV), the loose only signal and the loose only sub-signal region (using loose only electrons instead of medium ones). One can see the high event number at high $\Delta\eta$ and high η for all three regions.

Electron
standard reconstructed electron
medium electron identification
is not in LAr region with lost FEBs
$\|\eta\| < 1.37$ (barrel region)
b-layer hit > 1, if b-layer hit expected
$p_T > 25\,\text{GeV}$
Loose only electron
standard reconstructed electron
loose, but not medium electron identification
not in LAr region with lost FEBs
$\|\eta\| < 1.37$ (barrel region)
$p_T > 25\,\text{GeV}$
Photon
standard reconstructed photon loose photon identification
not in LAr region with lost FEBs
$\|\eta\| < 1.37$ (barrel region)
$p_T > 25\,\text{GeV}$
Object isolation
Transverse momentum in cone of $0.4 < 15$ GeV
Jet
reconstructed by anti-Kt algorithm with k-value of 0.4
$\|\eta\| < 2.47$
$p_T > 25\,\text{GeV}$
associated to real energy deposits
ΔR to leading electron/photon > 0.4
MET
MET corrected for electrons/photons in
LAr region with lost FEBs

Table 7.1. Object definitions.

Region name	List of selection requirements
signal region	require trigger EF_g80
	medium electron Pt $>$ 85 GeV
	jet Pt $>$ 100 GeV
	$\Delta\phi > \pi/2$
	$\Delta\eta < 1.5$
	electron isolated
	invariant mass (electron, jet) $>$ 90% of M_{TH}
loose only signal region	require trigger EF_g80
	loose only electron Pt $>$ 85 GeV
	jet Pt $>$ 100 GeV
	$\Delta\phi > \pi/2$
	$\Delta\eta < 1.5$
	photon isolated
	invariant mass (electron, jet) $>$ 90% of M_{TH}
low invariant mass control region	require trigger EF_g80
	medium electron Pt $>$ 85 GeV
	jet Pt $>$ 100 GeV
	$\Delta\phi > \pi/2$
	$\Delta\eta < 1.5$
	electron isolated
	invariant mass (electron, jet) $>$ 400 GeV
low loose only inv. mass control region	require trigger EF_g80
	loose only electron Pt $>$ 85 GeV
	jet Pt $>$ 100 GeV
	$\Delta\phi > \pi/2$
	$\Delta\eta < 1.5$
	electron isolated
	invariant mass (electron, jet) $>$ 400 GeV
low loose photon inv. mass control region	require trigger EF_g80
	loose photon Pt $>$ 85 GeV
	jet Pt $>$ 100 GeV
	$\Delta\phi > \pi/2$
	$\Delta\eta < 1.5$
	photon isolated
	invariant mass (photon, jet) $>$ 400 GeV
sub-signal control region	require trigger EF_g80
	medium electron Pt $>$ 85 GeV
	jet p_T $>$ 100 GeV
	$\Delta\phi > \pi/2$
	$\Delta\eta < 1.5$
	electron isolated
	800 GeV $<$ invariant mass $<$ 1 TeV
$Z \to e^+e^-$ control region	require trigger EF_e22
	two electrons with $\eta < 2.47$ (crack region excl.)
	both electrons pass medium with track ID
	both electron p_T $>$ 25 GeV
	66 GeV $<$ invariant mass $<$ 116 GeV
	opposite sign charge
	at least one jet with p_T $>$ 100 GeV

Table 7.2. List of signal and control regions.

Selection	Number of selected events	Signal acceptance
Basic event selection	1.7e+07	100%
One medium electron with $p_T > 85$ GeV	2.6e+05	79%
One jet with $p_T > 100$ GeV	1.4e+05	79%
$\Delta\phi$ of electron/jet $> \pi/2$	1.3e+05	79%
$\Delta\eta$ of electron/jet < 1.5	1.0e+05	57%
leading electron isolated	6.9e+04	56%
Invariant mass > 0.90 TeV	102	56%
Invariant mass > 1.13 TeV	26	56%
Invariant mass > 1.35 TeV	7	56%
Invariant mass > 1.58 TeV	2	55%
Invariant mass > 1.80 TeV	1	52%
Invariant mass > 2.03 TeV	1	-
Invariant mass > 2.25 TeV	0	-
Invariant mass > 2.48 TeV	0	-
Invariant mass > 2.70 TeV	0	-
Invariant mass > 3.60 TeV	0	-

Table 7.3. Cut flow for data and signal MC. The number of events passing each selection requirement in data are displayed. As comparison, the signal acceptance is shown for an example signal MC sample with M_{TH} of 2.0 TeV.

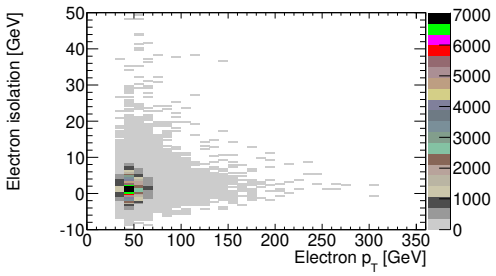

Figure 7.9. Electron isolation vs. p_T in the $Z \to e^+e^-$ region. The leading electron in the events is selected for both variables. Even for high-p_T electrons, the corrected isolation is uncorrelated to the electron p_T.

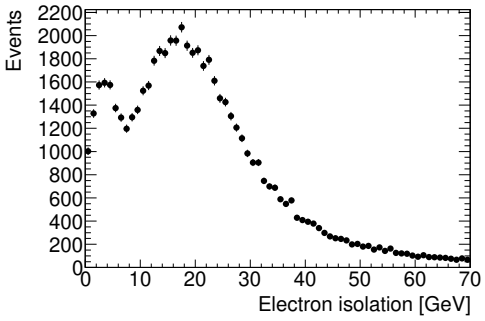

Figure 7.10. Electron isolation in the low loose mass region. Isolation of reconstructed electrons in the loose only low invariant mass region is shown without isolation cut, which is dominated by QCD events. The rejection power of an isolation requirement is large, even when applying a very loose selection of 15 GeV.

CHAPTER VIII

SIGNAL ACCEPTANCE

The acceptance of different MC BH samples has been studied for different values of M_{TH}. A change in most of the BH parameters doesn't change the event topology, but only influences the cross section. Since the invariant mass selection depends on M_{TH}, the acceptance does not change significantly as a function of M_{TH}. The only parameter that changes the event topology is the charge of the BH and therefore the charge of its decay products. In order to study this dependency, samples with a charge of 4/3 and 1/3 have been analyzed for M_{TH}= 3 TeV. Table 8.1. shows a summary of the signal acceptance after each selection for all available QBH MC samples. The difference in acceptance between the samples is not statistically significant, considering a 1.0% - 1.1%. statistical uncertainty. Hence, the acceptance is taken to be (51 $\pm$ 1)% (stat.) for all mass points.

M_{TH} and charge of BH	2.0 TeV, 4/3		3.0 TeV, 4/3		4.0 TeV, 4/3	
Initial number of events	4797	100%	4784	100%	4734	100%
One medium electron with $p_T > 85$ GeV	3792	79%	3743	78%	3775	80%
One jet with $p_T > 100$ GeV	3790	79%	3743	78%	3775	80%
$\Delta\phi$ of electron/jet $> \pi/2$	3790	79%	3743	78%	3775	80%
$\Delta\eta$ of electron/jet < 1.5	2734	57%	2724	57%	2695	57%
leading electron isolated	2683	56%	2669	56%	2635	56%
invariant mass $> 90\%$ of M_{TH}	2512	52%	2499	52%	2446	52%
M_{TH} and charge of BH	4.5 TeV, 4/3		5.0 TeV, 4/3		3.0 TeV, 1/3	
Initial number of events	4743	100%	4678	100%	4762	100%
One medium electron with $p_T > 85$ GeV	3743	79%	3734	80%	3815	82%
One jet with $p_T > 100$ GeV	3743	79%	3734	80%	3805	82%
$\Delta\phi$ of electron/jet $> \pi/2$	3743	79%	3734	80%	3805	82%
$\Delta\eta$ of electron/jet < 1.5	2656	56%	2607	56%	2747	58%
leading electron isolated	2589	55%	2520	54%	2689	56%
invariant mass $> 90\%$ of M_{TH}	2401	51%	2326	50%	2313	49%

Table 8.1. Signal acceptance for different signal QBH MC samples.

CHAPTER IX

BACKGROUND ESTIMATION

Separation of QCD and Non-QCD Contribution in the Low Invariant Mass Region

There are two major types of background to BHs decaying to lepton+jet: events that are dominated by the strong interaction (QCD events), which overwhelmingly don't contain real electrons, and those that are not dominated by the strong interaction (non-QCD events), which mostly contain real electrons. The non-QCD background includes $t\bar{t}$ production decaying semi- or full-leptonically, single top production in the s- and t-channel, di-boson production, Z-bosons decaying to e^+e^- or $\tau^+\tau^-$ and W-bosons decaying to $e\nu$ and $\tau\nu$, both produced in association with zero, one or more jets. Non-QCD events are expected to have a long tail in the missing transverse energy (MET) distribution due to the existence of real high p_T neutrinos. Not containing real neutrinos, QCD events have a much lower probability of causing significant missing transverse energy.

In order to estimate the contribution of both types of backgrounds, a low

invariant mass control region with similar cuts as the signal selection has been defined (see table 7.2.):

- Leading electron $p_T > 85\,\text{GeV}$
- Leading jet $p_T > 100\,\text{GeV}$
- $\Delta\phi$ between the leading jet and leading electron greater than $\pi/2$
- $\Delta\eta$ between the leading jet and leading electron smaller than 1.5
- Combined invariant mass of the leading jet and leading electron greater than $400\,\text{GeV}$

There are both contributions from QCD events ($N_{\text{QCD}}^{\text{lowMass}}$) and non-QCD events ($N_{\text{EW}}^{\text{lowMass}}$) to this region. The detailed number of events in the low mass regions for each MC sample and in data are shown in appendix B.

Using the MET distribution, a template method has been applied. The shape of the distribution from non-QCD events is estimated using the MC samples, while the shape of the distribution of QCD events is approximated by inverting the identification requirement on the leading electron to loose only (using events in the low loose only invariant mass control region). The two distributions are added with the normalization factors (n_{QCD} and $n_{\text{non-QCD}}$) as unknown variables, which are extracted by fitting the resulting sum to data using the maximum-likelihood method. The fit function is denoted with $y(x_i)$, where x_i is the independent variable of bin i and y is the dependent variable.

The two normalization factors are defined as:

$$n_{\text{QCD}} = \frac{N_{\text{QCD}}^{\text{lowMass}}}{N_{\text{loose}}^{\text{lowMass}}} \tag{IX.1}$$

$$n_{\text{non-QCD}} = \frac{N_{\text{EW}}^{\text{lowMass}}}{N_{\text{EW MC}}^{\text{lowMass}}} = \frac{N_{\text{EW}}^{\text{lowMass}}}{L \cdot \sigma \cdot \epsilon^{\text{lowMass}}} \tag{IX.2}$$

$N_{\text{loose}}^{\text{lowMass}}$ is the observed number of events in the loose only low invariant mass region in data, while $N_{\text{EW MC}}^{\text{lowMass}}$ is the sum of the EW MC events in the low invariant mass region normalized to the integrated luminosity. L, σ and $\epsilon^{\text{lowMass}}$ are the integrated luminosity, the weighted average cross section of EW events and the weighted average acceptance of EW events in the low invariant mass region. Note that due to statistical fluctuations in the finite MC sample and due to maximizing the likelihood during the fit, these equations are not exact, but they are well approximated.

Since the probability for an event to have a specific MET value is non-zero and constant[1], the observed number of events in a particular MET range follow a binomial distribution. The binomial distribution can be approximated by the Poisson distribution, since the number of trials is very large and the probability for a specific MET value in the low invariant mass region is very small. In addition, the expectation value is of intermediate magnitude.

In order to find the two parameters n_{QCD} and $n_{\text{non-QCD}}$ of the fitting function $y(x_i) = y(x_i; n_{\text{QCD}}, n_{\text{non-QCD}})$ from observations using the maximum-likelihood method, a normalized probability density function is defined for each bin. Using the assumption of a Poisson distribution, the probability P_i of the observation in

[1]The probability is assumed to be uncorrelated with previous or subsequent events.

the MET bin of value x_i can be calculated [117]:

$$P_i = P(x_i; n_{\text{QCD}}, n_{\text{non-QCD}}) \tag{IX.3}$$

The probability depends directly on the normalization factors n_{QCD} and $n_{\text{non-QCD}}$ in combination with the fixed QCD and non-QCD MET distributions. Together, they determine the mean of the Poisson distribution of observed events in each bin. A likelihood function $\mathscr{L}$ is defined as the product of all individual probabilities:

$$\mathscr{L}(n_{\text{QCD}}, n_{\text{non-QCD}}) = \prod_{i=1}^{n} P_i \tag{IX.4}$$

Maximizing $\mathscr{L}(n_{\text{QCD}}, n_{\text{non-QCD}})$ for variations of the normalization factors n_{QCD} and $n_{\text{non-QCD}}$ gives the maximum-likelihood values of the parameters, which are used to normalize the QCD and non-QCD contribution throughout the analysis. The result of the maximum-likelihood method can be seen in table 9.1. Figures 9.2.(c) and 9.2.(d) show the resulting distributions of the fit.

region	QCD norm.	non-QCD norm.	χ^2/NDF	NDF
low mass region	0.115 ± 0.004	0.97 ± 0.03	2.5	73
low photon mass region	0.38 ± 0.01	0.87 ± 0.03	2.3	73

Table 9.1. Results of the low invariant mass fit. The normalization factors are derived from the MET fit in the low invariant mass control region. Note that the QCD and non-QCD normalization factors are not expected to match due to different number of events in the loose only electron and photon low invariant mass region. The value for χ^2/NDF assumes a Gaussian distribution in all bins. This is an imprecise approximation for bins at high MET with only a few events.

To check the validity of this method, different variables are shown in figures 9.1., 9.2. and 9.3. for the low invariant mass region. The non-QCD shape is

retrieved from MC samples, while the shape from QCD contributions is measured in the low loose only electron p_T control region. Both distributions are normalized using the normalization factors found in the fit. The derived distributions show very good agreement with observations for a number of variables in the low invariant mass region, which gives confidence in using the described method of estimating the background.

Alternative QCD/Non-QCD Separation Technique

As an alternative method to estimate the QCD contribution, the QCD MET shape is not retrieved by inverting the electron ID requirement, but instead by selecting loose photons with p_T above 85 GeV. All other selections (p_T of the jet, $\Delta\phi$, $\Delta\eta$, isolation and invariant mass) remain unchanged. The sample is expected to be dominated by QCD events and should therefore give a similar MET distribution as observed in the low loose only invariant mass region. The overlap between the low invariant mass regions of loose only electrons with those of loose photons is very small with only 275 events, which represents 1.3% of the low loose only invariant mass region and 5.0% of the low photon invariant mass region. Figure 9.4. shows a comparison of the MET distribution for the two alternatives, both normalized to one. The peak of the distribution is slightly shifted, but the overall distribution is very similar. Table 9.1. gives the resulting normalization factors, while figure 9.5. shows the fit results for the distributions

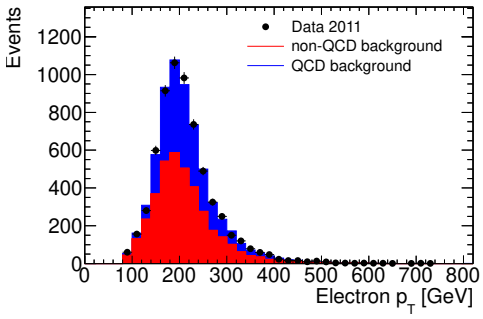

(a) leading electron p_T

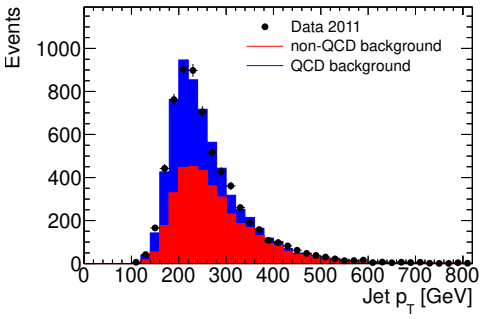

(b) leading jet p_T

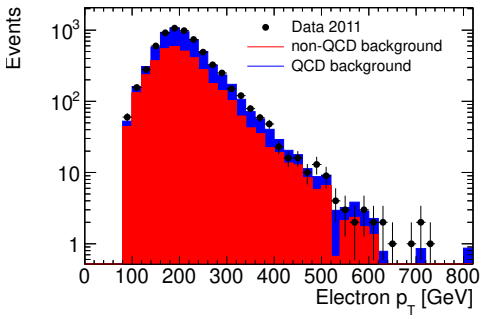

(c) leading electron p_T

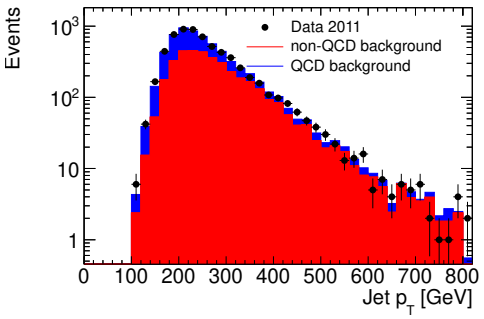

(d) leading jet p_T

Figure 9.1. Validation of QCD background (1). Distributions estimated for QCD and non-QCD are compared to data for electron and jet p_T in the low invariant mass region. The top plots are using a linear scale while the bottom plots are shown in log scale.

of MET and invariant mass. This alternative technique is used to estimate the systematic uncertainty of the expected QCD background.

The results of all methods and the goodness of the fits are summarized in table 9.1.

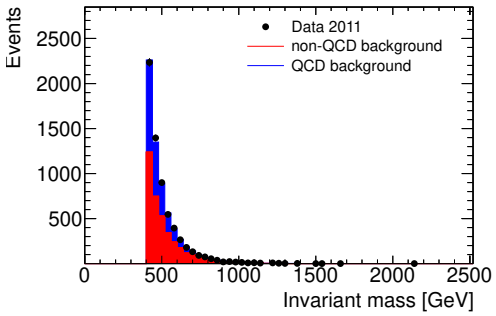

(a) invariant mass of electron/jet

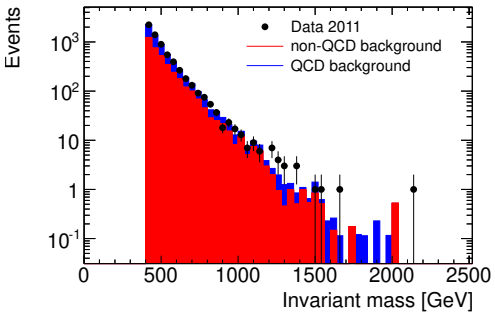

(b) invariant mass of electron/jet (log-scale)

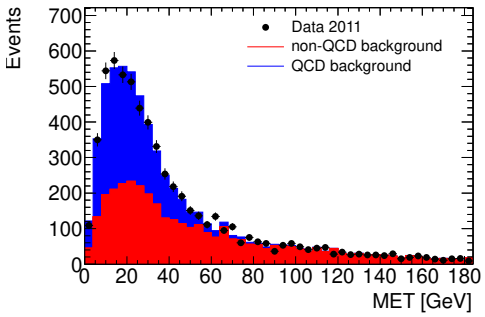

(c) missing transverse energy

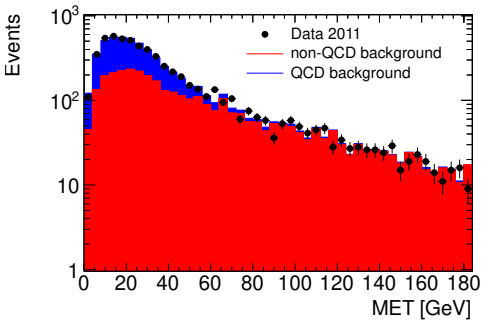

(d) missing transverse energy (log-scale)

Figure 9.2. Validation of QCD background (2). Distributions estimated for QCD and non-QCD are compared to data for invariant mass and MET in the low invariant mass region in both linear and log scale.

Non-QCD Background Estimation

The number of non-QCD background events passing the signal selection are derived from MC simulation, which are normalized using the factor derived in the low invariant mass control region (n_{QCD}). The cross sections used are given in

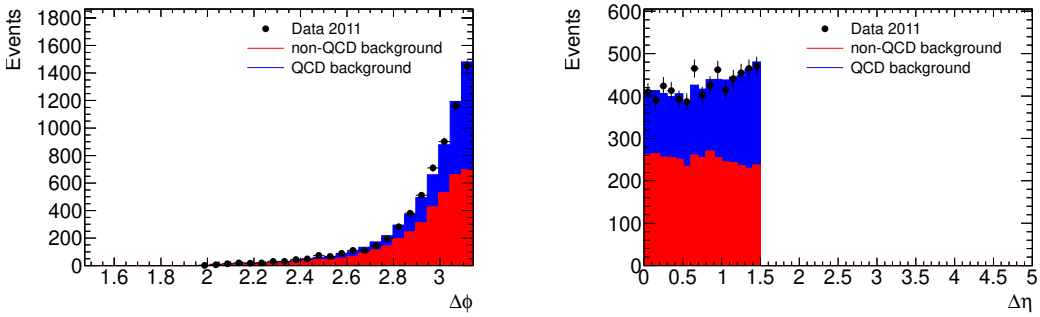

(a) $\Delta\phi$ between leading electron/jet (b) $\Delta\eta$ between leading electron/jet

Figure 9.3. Validation of QCD background (3). $\Delta\eta$ and $\Delta\phi$ distributions estimated for QCD and non-QCD are compared to data in the low invariant mass region. Note that a selection on $\Delta\eta$ and $\Delta\phi$ is applied in the low invariant mass region.

appendix A. Hence, the number of non-QCD events in the signal region ($N^{signal}_{non-QCD}$) is:

$$N^{\text{signal}}_{\text{non-QCD}} = N_{\text{EW MC}} \cdot n_{\text{non-QCD}} = \frac{N^{\text{lowMass}}_{\text{EW}} \cdot \epsilon^{\text{signal}}}{\epsilon^{\text{lowMass}}} \tag{IX.5}$$

where ϵ^{signal} is the weighted average acceptance of EW MC samples in the signal region.

QCD Background Estimation

The contribution to the signal region from QCD events is estimated using the loose only signal region. The number of events passing the loose only signal selection requirements are recorded and normalized with the QCD normalization

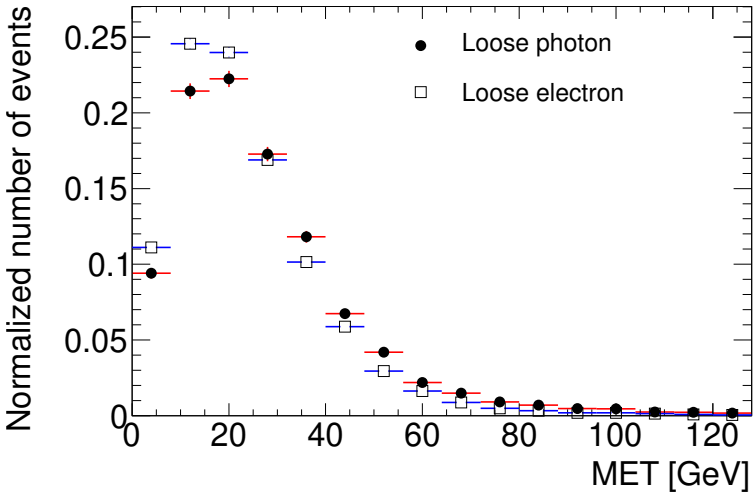

Figure 9.4. MET for loose only electron and photon events. The MET distribution for events in low loose only invariant mass region and low loose photon invariant mass region are compared.

factor ($n_{non-QCD}$) derived from the fit in the low invariant mass control region. The total number of QCD background events in the signal region is

$$N_{\mathrm{QCD}}^{\mathrm{signal}} = N_{\mathrm{loose}}^{\mathrm{signal}} \cdot n_{\mathrm{QCD}} = \frac{N_{\mathrm{loose}}^{\mathrm{signal}} \cdot N_{\mathrm{QCD}}^{\mathrm{lowMass}}}{N_{\mathrm{loose}}^{\mathrm{lowMass}}} \tag{IX.6}$$

$N_{\mathrm{loose}}^{\mathrm{signal}}$ is the number of events in the loose only signal region.

Signal Region Plots

Figures 9.6. - 9.9. show a comparison between expected and observed distributions of various variables in the signal region with a minimum mass cut of 1.35 TeV corresponding to M_{TH} of 1.5 TeV. For comparison a MC signal plot

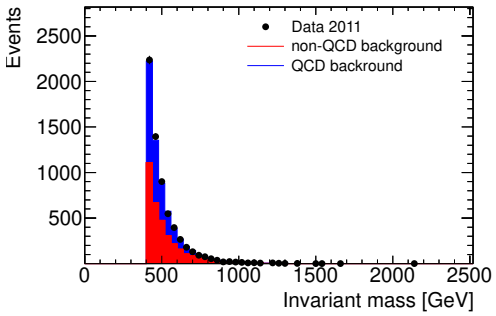

(a) invariant mass of electron/jet

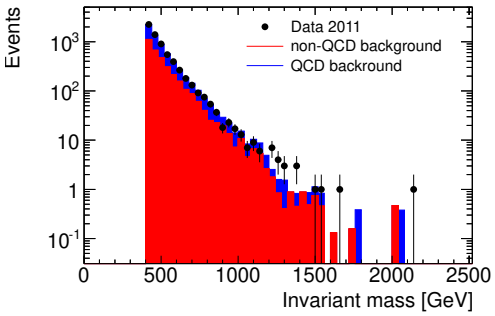

(b) invariant mass of electron/jet (log-scale)

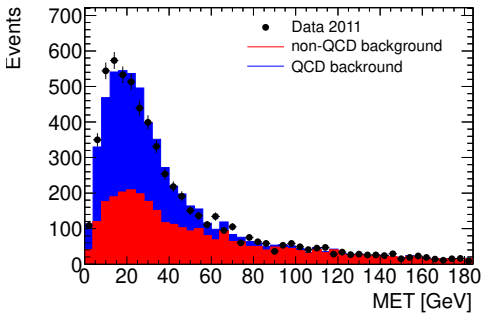

(c) missing transverse energy

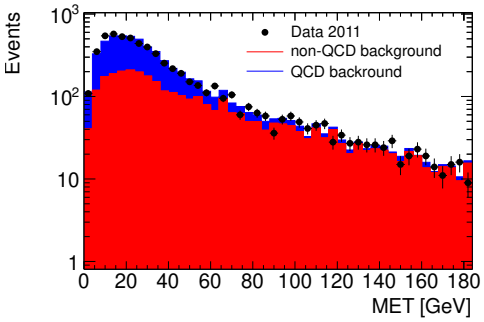

(d) missing transverse energy (log-scale)

Figure 9.5. Validation of photon-based QCD background estimation method in the low invariant mass region using loose photons instead of loose only electrons. Distributions estimated for QCD and non-QCD are compared to data for invariant mass and MET. The MET distribution is shown both with linear and log scale.

has been overlaid. The non-QCD contribution is estimated from MC, normalized with the fit result, while for the QCD contribution, the loose only signal region is used, normalized with the factor derived from the MET fit. Further signal region plots with minimum mass cuts of 900 GeV and 1.8 TeV corresponding to M_{TH} of 1.0 TeV and 2.0 TeV are shown in appendix C.

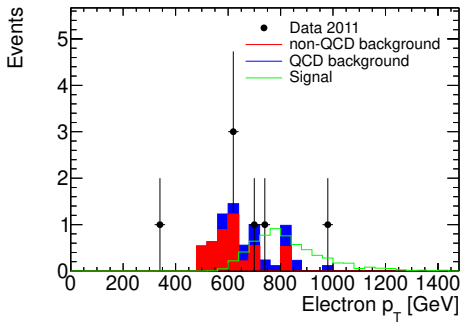

(a) Leading electron p_T

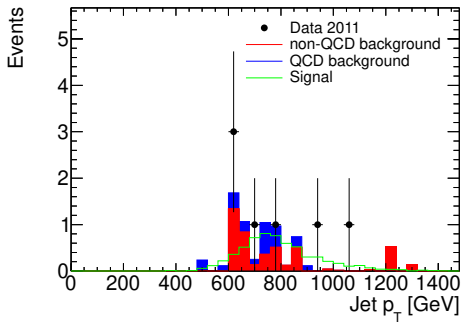

(b) Leading jet p_T

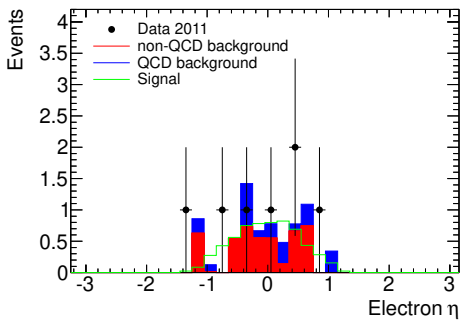

(c) Leading electron η

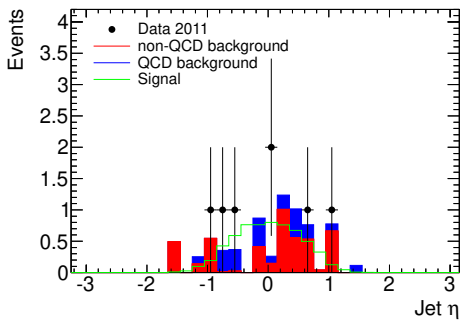

(d) Leading jet η

Figure 9.6. Distributions in signal region ($M_{TH} = 1.5\,\text{TeV}$) (1). Various distributions in the signal region are given for the expected background and observation. The QCD contribution has been estimated from data using loose only electrons and non-QCD contribution from MC. Both are normalized using the normalization factor from the fit in the low invariant mass region. The minimum invariant mass requirement is 1.35 TeV. A signal sample is overlaid for comparison, normalized to $\sigma = 5\,fb$.

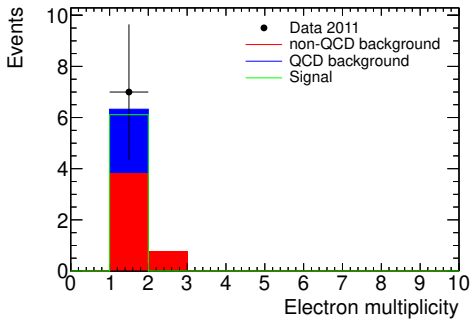

(a) Lepton multiplicity

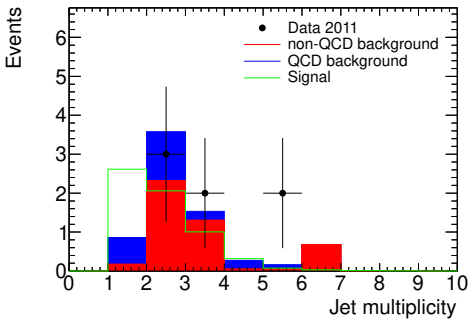

(b) Jet multiplicity

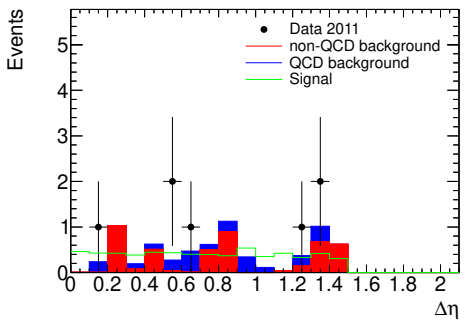

(c) $\Delta\eta$ between electron and jet

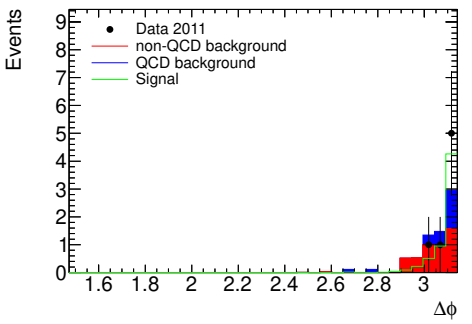

(d) $\Delta\phi$ between electron and jet

Figure 9.7. Distributions in signal region ($M_{TH} = 1.5\,\text{TeV}$) (2). Various distributions in the signal region are shown for the expected background and observation. The QCD contribution has been estimated from data using loose only electrons and non-QCD contribution from MC. Both are normalized using the normalization factor from the fit in the low invariant mass region. The minimum invariant mass requirement is 1.35 TeV. A signal sample is overlaid for comparison, normalized to $\sigma = 5\,fb$.

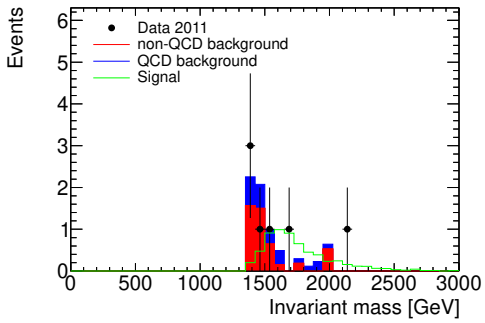

(a) invariant mass of electron/jet

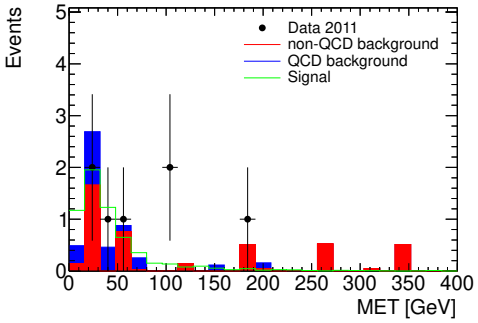

(b) Missing transverse energy

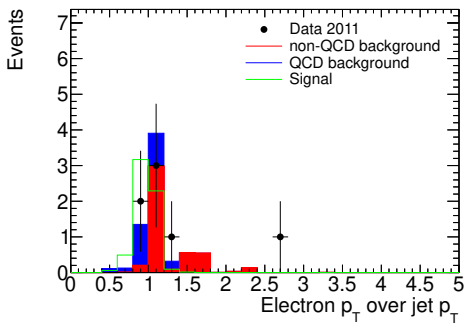

(c) Ratio of electron p_T and jet p_T

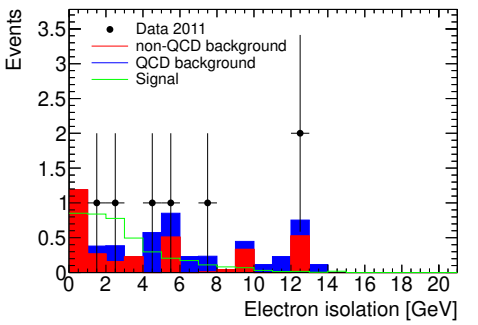

(d) Isolation of leading electron

Figure 9.8. Distributions in signal region ($M_{TH} = 1.5\,\text{TeV}$) (3). Various distributions in the signal region are given for the expected background and observation. The QCD contribution has been estimated from data using loose only electrons and non-QCD contribution from MC. Both are normalized using the normalization factor from the fit in the low invariant mass region. The minimum invariant mass requirement is 1.35 TeV. A signal sample is overlaid for comparison, normalized to $\sigma = 5\,fb$.

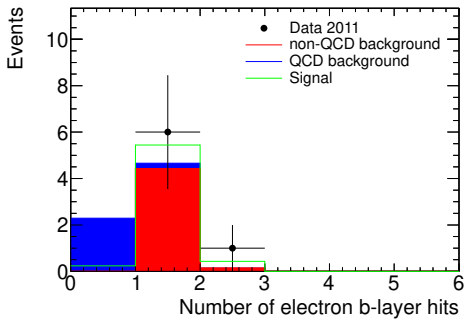

(a) Number of electron b-layer hits

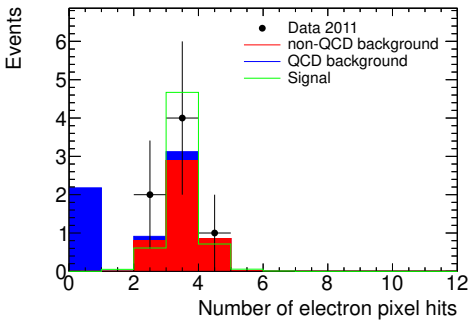

(b) Number of electron pixel hits

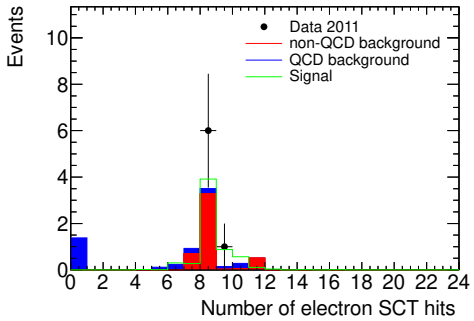

(c) Number of electron SCT hits

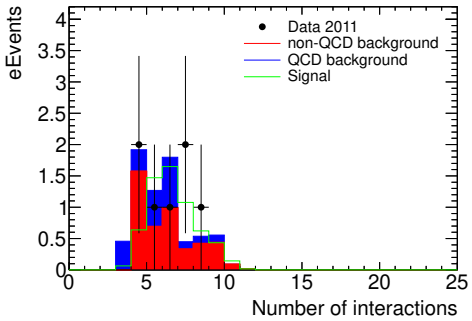

(d) Number of average interactions per bunch crossing

Figure 9.9. Distributions in signal region ($M_{TH} = 1.5\,\text{TeV}$) (4). Various distributions in the signal region are shown for the expected background and observation. The QCD contribution has been estimated from data using loose only electrons and non-QCD contribution from MC. Both are normalized using the normalization factor from the fit in the low invariant mass region. The minimum invariant mass requirement is 1.35 TeV. A signal sample is overlaid for comparison, normalized to $\sigma = 5\,fb$. The number of b-layer, pixel and SCT hits is zero for most of the QCD background (for loose only electrons), since hits are required for the medium selection, but not for loose ID.

CHAPTER X

BACKGROUND PREDICTION AT HIGH INVARIANT MASS

The total number of events in the signal region is recorded as a function of the invariant mass requirement. Each minimum mass selection is optimized for a set of models with a specific M_{TH}. Due to the low number of events in MC samples and in data at high invariant mass and the resulting large associated statistical uncertainty, the background is not calculated directly from the number of observed events above the invariant mass thresholds. Instead, the mass distribution is fitted and the fit is used to estimate the expected background. The original invariant mass distribution without the use of the fit can be seen in figure 10.1. For the QCD background, a power-law is used to fit the invariant mass in a range between 900 GeV and 2.0 TeV (see figure 10.4.(c)):

$$N(M_{inv}) = A \cdot {M_{inv}}^{d} \tag{X.1}$$

where M_{inv} is the combined invariant mass of the lepton and jet and N is the number of events. The non-QCD background is fitted in the same range with the following exponential function:

$$N(M_{inv}) = e^{a+d \cdot M_{inv}} \tag{X.2}$$

Figures 10.2. and 10.3. show the fit function in a range between 500 GeV and 2 TeV for the major non-QCD background contributions. The result for a selection of fits is shown in table 10.1. The slope of the fit of $W \rightarrow e\nu$ and $Z \rightarrow e^+e^-$ are consistent with each other and with other non-QCD background sources. The only fit that results in a different slope is the invariant mass distribution of the $t\bar{t}$ full hadronic and not full hadronic samples. Therefore, the exponential fit is done separately for the sum of both $t\bar{t}$ samples and the sum of all other non-QCD contributions (see figures 10.4.(a) and 10.4.(b)). The sum of both fitted functions is used to estimate the non-QCD background.

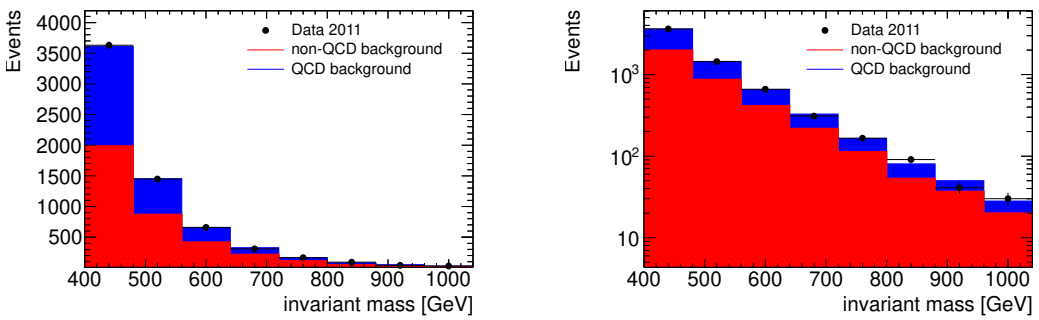

(a) invariant mass of electron/jet

(b) invariant mass of electron/jet (log-scale)

Figure 10.1. Original invariant mass distribution of electron plus jet events after all signal region selections with the exception of invariant mass, which has been lowered to 400 GeV. The QCD contribution has been estimated from data using loose only electrons and non-QCD contribution from MC. Both are normalized with the normalization factor from the fit in the low invariant mass region. Due to the large statistical fluctuations at high invariant mass, the expected background is not retrieved from this distribution, but instead from the fits of different background types.

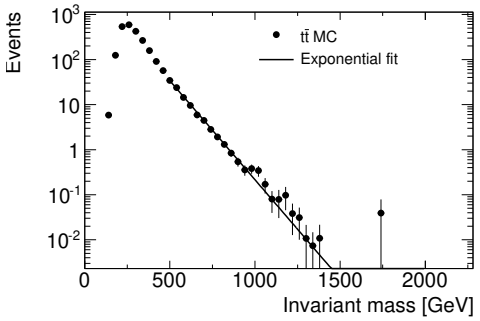

(a) $t\bar{t}$

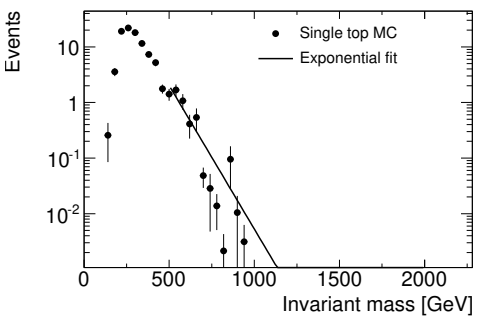

(b) single top

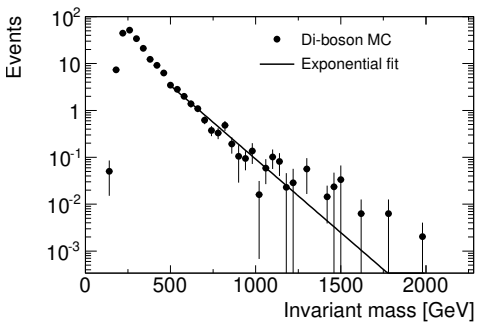

(c) di-boson

Figure 10.2. Fit to invariant mass of non-QCD MC samples (1). Invariant mass distribution for major non-QCD background sources are shown in the signal region with the invariant mass selection. An exponential fit produced in an invariant mass range of 500 GeV and 2 TeV is shown.

The fit functions do not have a physical interpretation. They are approximations of the behavior of the different backgrounds in the fitted mass region only. Above the collision energy of 7 TeV, the value of the fit functions is non-zero, which is in disagreement with the law of conservation of energy. However, the integral of the

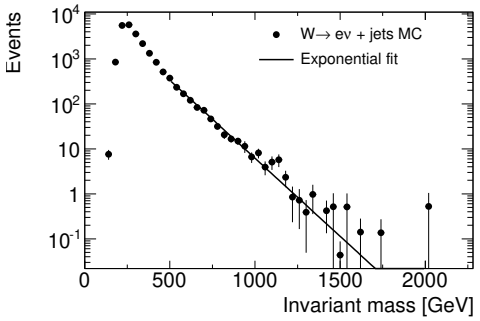

(a) $W \to e\nu$

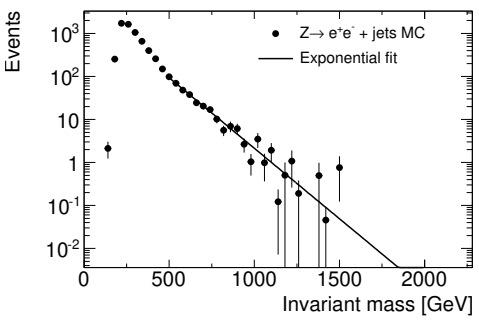

(b) $Z \to e^+e^-$

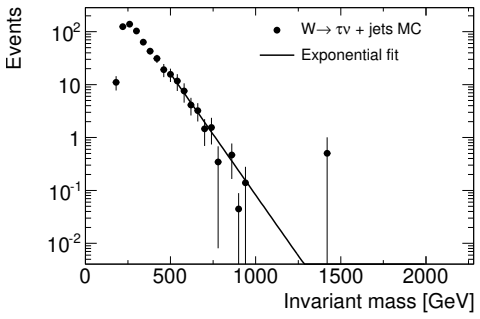

(c) $W \to \tau\nu$

Figure 10.3. Fit to invariant mass of non-QCD MC samples (2). Invariant mass distribution for major non-QCD background sources are displayed in the signal region with the invariant mass selection. An exponential fit produced in an invariant mass range of 500 GeV and 2 TeV is shown.

fits above 7 TeV is 1.8×10^{-3} and 4.2×10^{-29} for QCD and non-QCD, respectively, which is small enough to be neglected.

The functions derived by the fits are integrated from the value of the invariant mass selection to the center-of-mass energy of 7 TeV and normalized with the result from the normalization factors derived by the fit in the low invariant mass region.

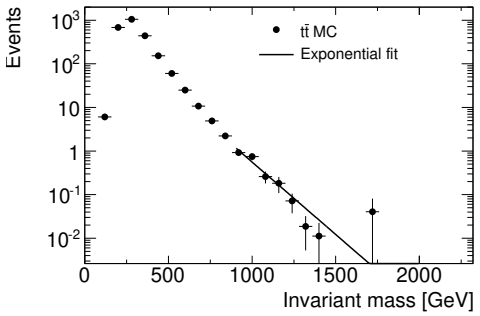

(a) $t\bar{t}$ MC signal region

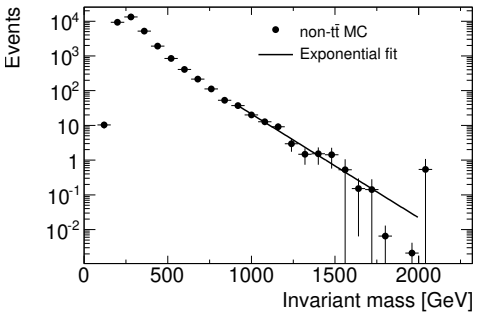

(b) non-$t\bar{t}$ MC signal region

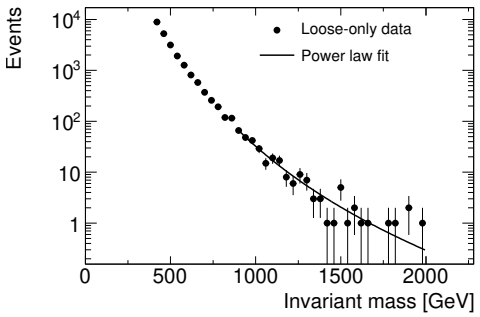

(c) observed loose signal region

Figure 10.4. Invariant mass fit of different background sources in the signal region without applying the invariant mass selection. The distribution and its fit are shown in the loose signal region in data and in the signal region for the sum of $t\bar{t}$ and the sum of non-$t\bar{t}$, non-QCD MCs. The fit in the loose only region is used to estimate the final number of QCD background events, while the non-QCD background is based on the sum of $t\bar{t}$ and non-$t\bar{t}$.

Instead of using the number of events passing the invariant mass cut directly, the normalized result of the fit is used as expected background. A comparison of the two methods is shown in table 10.2. The difference between the two methods is smaller than their statistical uncertainty. The resulting invariant mass distribution

fit region	fit range	A	d	χ^2/DoF	DoF
$t\bar{t}$	500 GeV - 2 TeV	8.58 ± 0.61	-0.0101 ± 0.0010	0.56	36
$W \to e\nu$	500 GeV - 2 TeV	9.81 ± 0.15	-0.0080 ± 0.0002	0.77	36
$Z \to e^+e^-$	500 GeV - 2 TeV	8.31 ± 0.26	-0.0075 ± 0.0004	1.41	36
Di-boson	500 GeV - 2 TeV	4.84 ± 1.27	-0.0072 ± 0.0020	1.21	36
sum of $t\bar{t}$ MC	900 GeV - 2 TeV	7.1 ± 5.7	-0.0077 ± 0.0056	0.89	12
sum of all non-$t\bar{t}$ MC	900 GeV - 2 TeV	9.9 ± 0.8	-0.0069 ± 0.0008	26	12
observed loose signal region	900 GeV - 2 TeV	$(7.5 \pm 7.0) \times 10^{21}$	-6.79 ± 0.13	0.8	26

Table 10.1. Results of the high invariant mass fits in the signal and loose signal regions. The fit is used to determine the expected background by integrating the fit from the invariant mass cut to 7 TeV. The large value of χ^2/DoF for the sum of non-$t\bar{t}$ MC is mainly driven by the few data points above 1.7 TeV. Reducing the upper bound of the fit range to 1.7 TeV decreases χ^2/DoF to 0.61 with 8 degrees of freedom without changing the fit result significantly. Note that the results in the loose signal and non-QCD MC signal region have different meanings due to different fit functions (see equations X.1 and X.2).

is shown in figures 10.5. and 10.6. The number of background, signal and observed events above various invariant mass thresholds can be seen in figure 10.7.

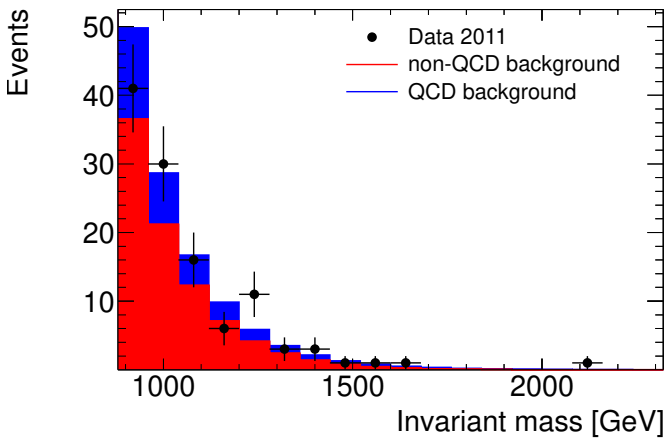

Figure 10.5. Final invariant mass distribution (linear scale). Expected and observed invariant mass distribution in the signal region without the invariant mass selection are shown. The background is estimated using the fit of the QCD and non-QCD background (for both $t\bar{t}$ and non-$t\bar{t}$ sources).

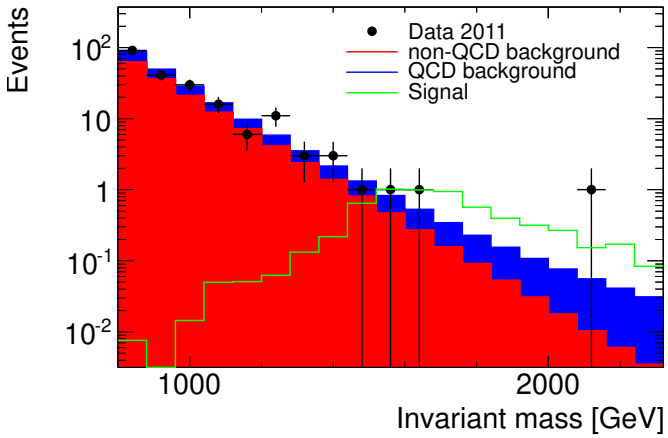

Figure 10.6. Final invariant mass distribution (log scale). Expected and observed invariant mass distribution in the signal region without the invariant mass selection are displayed. The background is estimated using the fit of the QCD and non-QCD background (for both $t\bar{t}$ and non-$t\bar{t}$ sources). The signal is shown for $M_{TH} = 1.5\,\text{TeV}$, normalized to a cross section of 5 fb.

M_{TH} [TeV]	1.00	1.25	1.50
invariant mass cut [TeV]	0.90	1.13	1.35
non-QCD background counts	76 ± 7	17.0 ± 2.9	4.2 ± 1.4
non-QCD background from fit	76 ± 8	16.2 ± 3.5	3.4 ± 1.3
QCD background counts	29 ± 2	7.7 ± 1.0	2.5 ± 0.5
QCD background from fit	29 ± 2	8.1 ± 0.6	2.8 ± 0.2
Total background counts	105 ± 7	24.7 ± 3.0	6.8 ± 1.5
Total background fits	106 ± 8	24.3 ± 3.5	6.2 ± 1.3
M_{TH} [TeV]	1.75	2.00	2.25
invariant mass cut [TeV]	1.58	1.80	2.03
non-QCD background counts	0.86 ± 0.56	0.53 ± 0.53	0
non-QCD background from fit	0.72 ± 0.40	0.15 ± 0.11	0.03 ± 0.03
QCD background counts	0.92 ± 0.33	0.46 ± 0.23	0
QCD background from fit	1.15 ± 0.11	0.53 ± 0.06	0.27 ± 0.03
Total background counts	1.77 ± 0.65	0.98 ± 0.57	0
Total background fits	1.88 ± 0.42	0.69 ± 0.13	0.30 ± 0.05
M_{TH} [TeV]	2.50	2.75	3.00
invariant mass cut [TeV]	2.25	2.48	2.70
non-QCD background counts	0	0	0
non-QCD background from fit	0.007 ± 0.007	0.001 ± 0.002	0.0003 ± 0.0004
QCD background counts	0	0	0
QCD background from fit	0.146 ± 0.020	0.084 ± 0.013	0.0507 ± 0.0082
Total background counts	0	0	0
Total background fits	0.153 ± 0.022	0.086 ± 0.013	0.0511 ± 0.0082
M_{TH} [TeV]	4.00	5.00	
invariant mass cut [TeV]	3.60	4.50	
non-QCD background counts	0	0	
non-QCD background from fit	$(6.3 \pm 13.6)\times10^{-7}$	$(1.3 \pm 3.7)\times10^{-9}$	
QCD background counts	0	0	
QCD background from fit	0.009 ± 0.002	0.0024 ± 0.0005	
Total background counts	0	0	
Total background fits	0.009 ± 0.002	0.0024 ± 0.0005	

Table 10.2. Fitted vs. original expected background. A comparison of expected background from counting events above the invariant mass cut and and from integrating the background fit from the invariant mass cut to 7 TeV are displayed. Only statistical uncertainties are considered.

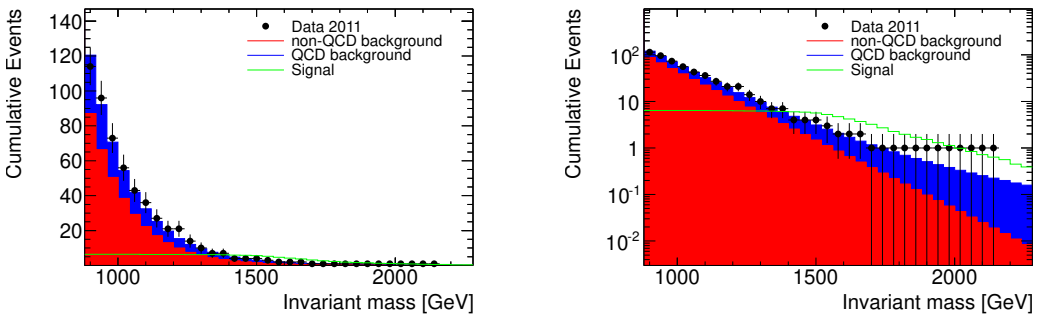

(a) linear scale

(b) log-scale

Figure 10.7. Cumulative final invariant mass distribution. In each bin, the number of background, signal and observed events with invariant mass above the lower edge of the bin is shown. All other signal region cuts have been applied. The signal is shown for $M_{TH} = 1.5\,\text{TeV}$, normalized to a cross section of 5 fb.

CHAPTER XI

SYSTEMATIC UNCERTAINTIES

Several sources of systematic uncertainty on the number of events from signal and expected background (both QCD and non-QCD) are considered. For each source, the effect on the number of events in the signal region has been studied.

Trigger, Reconstruction and Identification Scale Factors

Different efficiencies of the electron trigger, reconstruction and identification algorithms between data and MC have been measured [115]. In order to correct for the difference, scale factors have been derived by the ATLAS experiment as a function of η and p_T for all three algorithms. The scale factors are applied to all MC samples by default. Upward and downward variations of the scale factors by one standard deviation for each of the algorithms have been studied. For the non-QCD background, the contribution is normalized to data in the low invariant mass region, such that only the difference in scale factors between the low mass region and the signal region has an effect on the final event number. It is assumed that the correlation between different η and p_T bins is one. The

analysis is re-run for each scale factor fluctuation separately and the fitting results in the low invariant mass region and the final event numbers are recorded for the non-QCD background and the signal MC samples. The differences to the nominal number of events are used as systematic uncertainties. Due to the normalization of the non-QCD background in the low invariant mass control region, the effect on the final background estimate is expected and observed to be negligible. The QCD contribution is not estimated using MC samples, making the background independent of the scale factor uncertainties.

Jet Energy Scale and Jet Energy Resolution

Uncertainties in the jet energy scale (JES) and the jet energy resolution (JER) result in uncertainties on the number of events in the signal region estimated from MC samples. Uncertainties of the JES and JER have been estimated by the ATLAS experiment as a function of η and p_T [118]. The effect of an upward and a downward fluctuation of the JES on the analysis has been studied for both the expected non-QCD background and the signal MC samples. For the jet energy resolution, the jet p_T of each event is smeared by taking the original p_T value and adding a random number from a Gaussian distribution with a mean of zero and a standard deviation of the resolution uncertainty. The relative uncertainty from the JER is separately taken as positive and negative relative fluctuation. For both variations, the MET

has been recalculated with the new transverse momentum of all jets and the fit in the low invariant mass region has been redone. The difference to the nominal result is the systematic error for both sources.

Due to the normalization of the non-QCD background in the low invariant mass region, the effect of the JES on the MET distribution is an additional error propagator, not only the change in jet p_T or invariant mass. Hence, a variation in the JES not only leads to a change in the number of events in the signal and low invariant mass control region, but also to a shift of the MET distribution. This results in an additional change of the non-QCD normalization factor. Therefore, the relative change of the normalization factor is larger than the relative change of the number of events in the signal region. This shows up in the fact that an increase of the JES results in a decrease of the number of expected non-QCD events, while the number of expected events are hihger for a upward fluctuation of the JES.

Electron Energy Scale and Electron Energy Resolution

The effects of the electron energy scale (EES) uncertainty and the uncertainty of the electron energy resolution (EER) on the background and signal have been studied. Both types of uncertainty have been estimated by the ATLAS experiment [115] as a function of η and p_T. Upward and downward fluctuations of the electron energy scale have been applied for each electron. In addition,

upward fluctuations of the electron energy resolution have been simulated. For both variations, MET has been recalculated with the resulting electrons' transverse momenta and new normalization factors are derived. The difference of expected events in the signal region and the nominal result is taken as systematic error. For the electron energy resolution, the relative effect of the upward fluctuation has also been used as downward fluctuation.

Integrated Luminosity

The uncertainty on the integrated luminosity is not expected to have any effect on the expected background, since both types of background are normalized in the low invariant mass region. In order to confirm this statement, the uncertainty on the luminosity of 3.7% as measured by the ATLAS experiment [86] [83] has been used to fluctuate the luminosity upward and downward. The normalization factors for the background using the fit in the low invariant mass region and the number of events in the signal region have been determined with the varied luminosity. The difference to the default scenario is taken as systematic error for the non-QCD background and signal acceptance. As expected, the observed non-QCD background uncertainty is zero. Since the signal MC is not normalized using the normalization factors of the low invariant mass region, the 3.7% uncertainty of the luminosity translates into a 3.7% uncertainty of the signal.

QCD Background Estimation Technique

The main uncertainty coming from the technique of estimating the QCD background is due to differences between various distributions in the loose only and default low mass region on the one hand and in the loose only and default signal region on the other hand. The uncertainty of this technique is evaluated by varying the distributions of different variables that are used in selecting events in the low mass region and in the signal region. The variation is done by selecting a sample of loose photons instead of loose only electrons which pass the selection requirements for the low invariant mass region (low photon invariant mass control region). The sum of the MET distribution from this sample and from the non-QCD MC have been fitted to data as described above. The normalization factor from the fit is used to normalize the number of events in the signal region using loose photons which pass the signal selection instead of medium electrons. The difference between this technique and the nominal one is taken as systematic error for the QCD background.

$\Delta\phi$, $\Delta\eta$ and Electron Isolation Selection

In order to estimate the uncertainty due to the acceptance uncertainty in MC of the $\Delta\phi$, $\Delta\eta$ and electron isolation selection, a sample containing events with a

Z-boson decaying to two electrons plus one jet with a transvers momentum above 100 GeV has been selected (see $Z \rightarrow e^+e^-$ region in table 7.2.). The sample is assumed to have a very low background, so that the difference in acceptance between data and MC is taken as systematic uncertainty.

For the non-QCD background, the samples with the dominating contributions ($W \rightarrow e\nu$ + jets and $Z \rightarrow e^+e^-$ + jets) are generated using Alpgen. Hence, the comparison between MC and data in the $Z \rightarrow e^+e^-$ region is done using the samples of $Z \rightarrow e^+e^-$ + jet events generated with Alpgen. The comparison of the three main selection variables are shown in figure 11.1. The normalization fit in the low invariant mass control region is redone for each of the three variables separately, using the relative error in acceptance as an additional overall normalization to the MC samples before the fit. Hence, the uncertainty on the final non-QCD background is negligible.

The signal MC samples have been generated using QBH in combination with Pythia. Hence, an inclusive Pythia sample of $Z \rightarrow e^+e^-$ events is used to compare the selection variables to data (see figure 11.2.). Because the production of additional gluons is better described in Alpgen than in Pythia, the uncertainty in the $\Delta\phi$ acceptance is much larger for Pythia-based signal samples than for MC events produced by Alpgen. For the signal acceptance the normalization factors from the low invariant mass control region are not used, resulting in a non-zero uncertainty on the acceptance. However, due to the loose selections, the systematic

uncertainties of the acceptance from the selection variables are small compared to other sources of uncertainty.

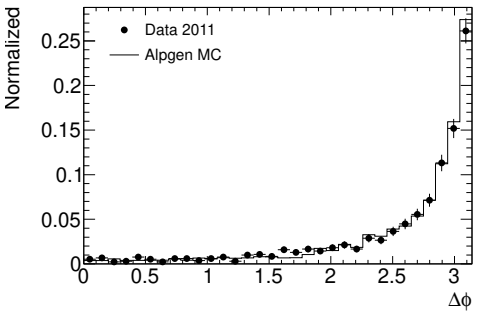

(a) $\Delta\phi$

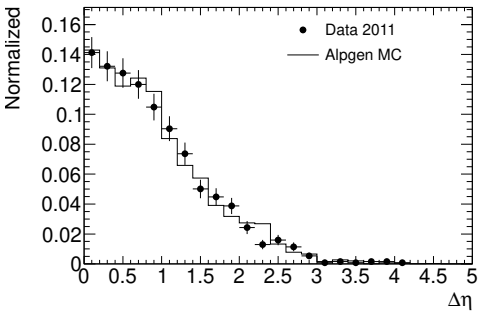

(b) $\Delta\eta$

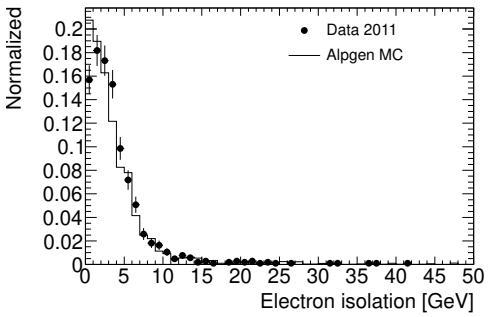

(c) Electron isolation

Figure 11.1. Alpgen/Data comparison. The distributions of $\Delta\phi$, $\Delta\eta$ and electron isolation are compared between data and Alpgen MC in $Z \to e^+e^-$ region with at least one additional high p_T jet (p_T above 100 GeV). $\Delta\phi$ and $\Delta\eta$ are calculated between the reconstructed Z-boson and the additional leading jet. For the electron isolation, the leading electron of the Z-boson decay has been selected. All distributions are normalized to one.

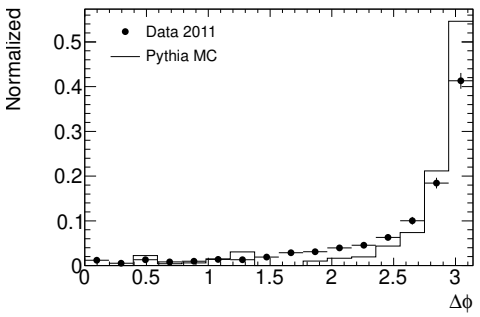

(a) $\Delta\phi$

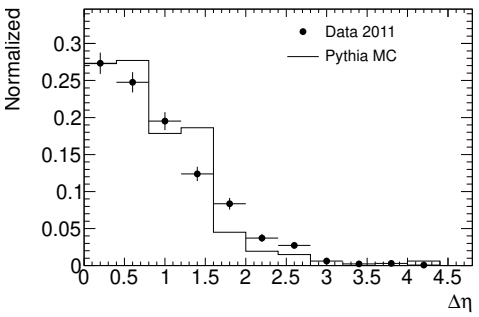

(b) $\Delta\eta$

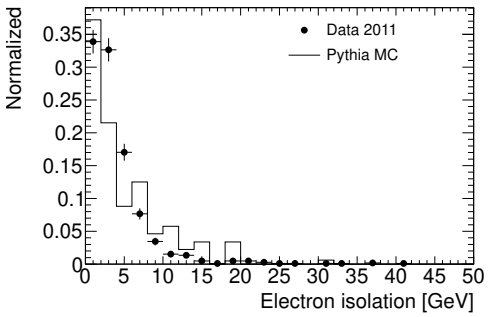

(c) Electron isolation

Figure 11.2. Pythia/Data comparison. The distributions of $\Delta\phi$, $\Delta\eta$ and electron isolation are compared between data and Pythia MC in $Z \to e^+e^-$ region with at least one additional high p_T jet (p_T above 100 GeV). $\Delta\phi$ and $\Delta\eta$ are calculated between the reconstructed Z-boson and the additional leading jet. For the electron isolation, the leading electron of the Z-boson decay has been selected. All distributions are normalized to one.

Parton Distribution Function

The systematic uncertainty due to the PDF uncertainty in MC has been estimated by evaluating the differences of each of the 20 upward and downward

errors to the nominal numbers for the PDF CTEQ6.6 [18]. For each of the upward and downward fluctuations, the normalization factors have been derived and the events in the signal region calculated. In order to avoid the production of MC samples for each PDF, different event weights are applied to the nominal samples as a function of momentum transfer and type of the colliding partons. This procedure corrects for the difference in propability of occurrance of collisions involving specific partons with a given momentum transfer between the PDFs. The difference to the nominal value is taken as uncertainty. The quadratic sum of all errors is the total systematic uncertainty from the PDF uncertainty. Due to the dependence on the energy scale, this source of uncertainty is estimated at each mass point individually. For mass points where no events are available, the PDF uncertainty for the next higher mass point is used. If there is no higher mass point for which the PDF uncertainty is available, the uncertainty of the next lower mass point is assumed.

Background Fit

The background is fitted with a power-law (for QCD) or an exponential function (non-QCD). The systematic uncertainty of the fit is estimated by varying the boundaries of the fit by 100 GeV. Since the uncertainty increases with invariant

mass, the uncertainty due to the background fit has been estimated at each mass point individually (see table 11.2. for results).

Summary

Due to a lack of statistics at high invariant mass requirements, the relative systematic errors are evaluated with an invariant mass selection of 900 GeV corresponding to quantum BH models with M_{TH} of 1 TeV (see table 11.1.). They are then applied to the number of expected events for all invariant mass selections. The only two sources of uncertainty which are expected to change significantly as a function of invariant mass are the uncertainties of the PDF and the uncertainty of the background fit. Both sources are therefore estimated for each mass point individually. Table 11.2. shows the PDF and fit uncertainty for each mass point and the resulting total systematic uncertainty. Above 2 TeV, where no MC background events are available, the PDF uncertainty is taken to be the same relative uncertainty as for $M_{TH} = 2.0$ TeV.

In table 11.3., the number of background events and their statistical and systematic uncertainties are shown together with the number of observed events and the corresponding p-value of the background only hypothesis. There is no indication of disagreement between the expected background and observation.

Source of uncertainty	non-QCD [%]		QCD [%]		signal [%]	
Direction of fluctuation	up	down	up	down	up	down
Trigger efficiency	0.0	0.0			0.4	-0.4
Reconstruction efficiency	-0.0	0.0			0.7	-0.7
Identification efficiency	-0.0	0.0			0.7	-0.7
Jet Energy Scale	-7.2	2.3			0.6	-0.5
Electron Energy Scale	1.1	-1.1			0.1	-0.1
Electron Energy Resolution	0.3	-0.8			-0.2	-0.0
Jet Energy Resolution	3.5	-4.5			0.2	-0.1
Luminosity	0.0	0.0			3.7	-3.7
Parton Distribution Functions	5.5	-4.5			15.3	-18.9
$\Delta\phi$ selection	0.0	0.0			1.7	-1.7
$\Delta\eta$ selection	0.0	0.0			0.1	-0.1
Electron isolation requirement	0.0	0.0			0.2	-0.2
Invariant mass fit	3.5	-3.5	2.3	-2.3		
QCD estimation technique			47.3	-47.3		
Total without PDF & fit uncert.	4.3	-8.6	47.3	-47.3	4.3	-4.3
Total	7.8	-10.3	47.4	-47.4	15.9	-19.4

Table 11.1. Overview of sources of systematic uncertainties. "Up" and "Down" refers to the upward fluctuation or downward fluctuation of the error source, respectively. Since both upward and downward fluctuations can result in an increase or decrease of the final event count, the sign for both fluctuations can be the same or reversed. The last two lines give the total upward and downward error, where only positive and negative contributions have been considered.

M_{TH} [TeV]	1.00	1.25	1.50	1.75	2.00	2.25
invariant mass cut [TeV]	0.90	1.13	1.35	1.58	1.80	2.03
			Non-QCD background			
PDF Uncertainty [%]	+5.5/-4.5	+6.9/-5.3	+12/-9	+33/-23	+26/-20	+26/-20
Fit Uncertainty [%]	3.5	5.3	15	26	38	51
Total Sys. Uncertainty [%]	+7.8/-10.3	+9.7/-11.4	+20/-19	+42/-36	+46/-44	+57/-55
			QCD background			
Fit Uncertainty [%]	2.3	0.5	2.8	4.7	6.3	7.7
Total Sys. Uncertainty [%]	47	47	47	48	48	48
			Signal MC acceptance			
PDF Uncertainty [%]	+15/-19	+15/-19	+15/-19	+25/-29	+25/-29	+25/-29
Total Sys. Uncertainty [%]	+16/-19	+16/-19	+16/-19	+25/-29	+25/-29	+25/-29
M_{TH} [TeV]	2.50	2.75	3.00	4.00	5.00	
invariant mass cut [TeV]	2.25	2.48	2.70	3.60	4.50	
			Non-QCD background			
PDF Uncertainty [%]	+26/-20	+26/-20	+26/-20	+26/-20	+26/-20	
Fit Uncertainty [%]	66	81	99	187	314	
Total Sys. Uncertainty [%]	+71/-69	+85/-84	+102/-101	+189/-188	± 315	
			QCD background			
Fit Uncertainty [%]	8.9	10	11	14	16	
Total Sys. Uncertainty [%]	48	48	48	49	50	
			Signal MC acceptance			
PDF Uncertainty [%]	+65/-59	+65/-59	+65/-59	+154/-100	+380/-152	
Total Sys. Uncertainty [%]	+65/-59	+65/-59	+65/-59	+154/-100	+380/-152	

Table 11.2. Systematic uncertainties as a function of M_{TH} from sources that are not estimated at 900 GeV for all mass selections, but which are determined for each mass point. Due to a lack of statistics, the PDF uncertainty can not be determined for M_{TH} above 2.5 GeV. For these mass points, the uncertainties are estimated using the relative uncertainty as derived for $M_{TH} = 2.25$ TeV. The resulting total systematic uncertainty including sources measured at 900 GeV is given.

M_{TH} [TeV]	1.00	1.25	1.50	1.75	2.00	2.25
invariant mass cut [TeV]	0.90	1.13	1.35	1.58	1.80	2.03
non-QCD background	77	16.2	3.4	0.7	0.2	0.03
Stat. Error	8	3.5	1.3	0.4	0.1	0.03
Syst. Error	+6/-8	+1.6/-1.8	0.7	0.3	0.1	0.02
QCD background	29	8.1	2.8	1.2	0.5	0.27
Stat. Error	2	0.6	0.2	0.1	0.1	0.03
Syst. Error	14	3.8	1.3	0.6	0.3	0.013
Total Background	106	24.3	6.2	1.9	0.7	0.30
Stat. Error	8	3.5	1.3	0.4	0.1	0.04
Syst. Error	+15/-16	+4.1/-4.2	1.5	0.6	0.3	0.13
Observed	102	26	7	2	1	1
Stat. Error	10	5.1	2.7	1.4	1.0	1.00
p-value, background only	0.58	0.42	0.42	0.54	0.47	0.26
Signal acceptance [%]	51	51	51	51	51	51
Stat. Error [pp]	1	1	1	1	1	1
Syst. Error without PDF [pp]	2	2	2	2	2	2
Syst. Error with PDF [pp]	+8/-10	+8/-10	+8/-10	+13/-15	+13/-15	+13/-15

M_{TH} [TeV]	2.50	2.75	3.00	4.00	5.00
invariant mass cut [TeV]	2.25	2.48	2.70	3.60	4.50
non-QCD background	0.007	0.002	0.0003	6.3×10^{-7}	1.3×10^{-9}
Stat. Error	0.008	0.002	0.0004	13.6×10^{-7}	3.7×10^{-9}
Syst. Error	0.005	0.001	0.0003	11.8×10^{-7}	4.0×10^{-9}
QCD background	0.146	0.084	0.051	0.009	0.0024
Stat. Error	0.021	0.013	0.008	0.002	0.0005
Syst. Error	0.070	0.040	0.024	0.005	0.0012
Total Background	0.153	0.086	0.051	0.009	0.0024
Stat. Error	0.022	0.013	0.008	0.002	0.0005
Syst. Error	0.070	0.040	0.024	0.005	0.0012
Observed	0	0	0	0	0
Stat. Error	0	0	0	0	0
p-value, background only	1.0	1.0	1.0	1.0	1.0
Signal acceptance [%]	51	51	51	51	51
Stat. Error [pp]	1	1	1	1	1
Syst. Error without PDF [pp]	2	2	2	2	2
Syst. Error with PDF [pp]	+33/-30	+33/-30	+33/-30	+79/-51	+194/-51

Table 11.3. Final number of expected and observed events in the signal region are shown including the derived p-value for the background only hypothesis. In addition, the signal acceptance is shown. The uncertainty of the signal acceptance is given in percentage points.

CHAPTER XII

OBSERVED AND EXPECTED CROSS SECTION LIMITS

Following the CLs method [119], an upper limit is set on the cross section times branching fraction for different invariant mass cuts corresponding to models with different minimum BH masses. The first step is a definition of a likelihood function $\mathscr{L}$:

$$\mathscr{L}(s,\delta) = \text{Pois}(n|(1+\eta_s\delta_s)s+\sum_{i=0}^{1}((1+\eta_{b_i}\delta_i)b_i))\times\text{Gaus}(m_s|\delta_s,1)\times\prod_{i=0}^{1}\text{Gaus}(m_i|\delta_i,1) \tag{XII.1}$$

where

- n is the number of observed events,
- s and b_i are the number of events from signal and background of type i, respectively,
- η_s and η_{b_i} are the uncertainty of the signal and the background of type i, respectively,
- δ_s is the signal efficiency nuisance parameter and δ_i is the nuisance parameter of the background of type i,

- m_s is the sideband efficiency measurement and m_i is the auxiliary measurements of the background uncertainties.

The Poisson distribution describes the distribution of the number of events assuming a mean of the sum of the signal and all expected backgrounds. The remaining factors represent the constraints on the systematic uncertainties, which are assumed to follow a Gaussian probability distribution. From the likelihood function, the one sided version of the test statistics q_s is defined as

$$q_s = \begin{cases} -2\ln\dfrac{\mathscr{L}(s,\hat{\hat{\delta}})}{\mathscr{L}(\hat{s},\hat{\delta})} & \text{if } \hat{s} < s, \\ 0 & \text{if } \hat{s} > s. \end{cases}$$

where $\hat{s}$ and $\hat{\delta}$ are the unconditional maximum-likelihood estimator (maximizing $\mathscr{L}(s,\delta)$ globally) and $\hat{\hat{\delta}}$ the conditional maximum-likelihood estimator (maximizing $\mathscr{L}(s,\delta)$ for a given signal strength s).

Using the test statistic q_s a large number of signal strengths are tested by varying the number of expected signal events s. For each tested value of s, the following steps have been performed. First, the test statistics $q_{s,obs}$ for the signal strength s is found, assuming the observed number of events. Second, 10000 MC pseudo-experiments are run in order to construct a distribution of the test statistics $f(q_s|s)$. The p-value of the signal+background hypothesis is retrieved from the distribution of $f(q_s|s)$:

$$p_s = \int_{q_{s,obs}}^{\infty} f(q_s|s)dq_s \qquad \text{(XII.2)}$$

The p-value of the background only hypothesis is calculated as:

$$p_b = 1 - \int_{q_{s,obs}}^{\infty} f(q_s|0)dq_s \tag{XII.3}$$

Using these p-values, CLs for each signal strength s is defined as:

$$CL_s = \frac{p_s}{1 - p_b} \tag{XII.4}$$

By iteration, the highest signal strength is found for which $CL_s \geq 5\%$. This is considered to be the upper limit of the signal strength. Dividing p_s by $(1 - p_b)$ prevents the exclusion of models to which the test has little sensitivity. Otherwise, in experiments where the number of observed events is much lower than predicted by the background, a large range of signal cross sections could be excluded, even though the test lacks the power to differentiate between the signal+background and the background only hypothesis. Using the acceptance as derived earlier and the measured luminosity, the upper limit of the signal strength can be transformed into an upper limit on the signal cross section.

For the expected limit with bands, the distribution of upper limits on the background-only hypothesis needs to be obtained. This is done by repeating the previous procedure for various background only pseudo-experiments. The median value of the distribution of upper limits is the expected cross section limit and the 68% and 95% bands of the distribution are the $\pm 1\,\sigma$ and $\pm 2\,\sigma$ expected bands of the cross section limits.

In order to allow the calculations of limits on models which are not considered explicitly in this analysis, but for which the cross section is known, the cross section limits are given without including the signal PDF uncertainty. However, the PDF uncertainties are considered for the calculation of the predicted cross section by various models. All other signal and background uncertainties discussed above are considered for the final cross section limits. The result for each mass threshold is shown in table 12.1. Figure 12.1. shows the expected and observed upper limit together with the cross section as predicted by the generator QBH [105] for different values of M_{TH}, M_{Pl} and different type and number of extra dimensions. For a Planck mass of 2 TeV, the theoretical predictions for different type and number of extra dimensions are shown in figure 12.2. together with the observed and expected upper limit. For the calculation of the theoretical signal cross section, only BHs of electric charge 1/3 and 4/3 produced in interactions between two quarks (q-q) have been included. As discussed above, BHs of charge 1/3 produced by the interaction of a quark and a gluon (q-g) can not decay to an electron and a quark without violating Lorentz invariance.

Figure 12.3. shows the parameter space in M_{PL} and M_{TH} that can be excluded based on the observed limits on the cross section of electron plus jet events.

M_{TH} [TeV]	1.00	1.25	1.50	1.75	2.00	2.25
Invariant mass cut [TeV]	0.90	1.13	1.35	1.58	1.80	2.03
Observed upper limit [fb]	42.14	18.05	8.26	4.33	3.39	3.39
Expected upper limit [fb]						
-2 sigma	25.76	9.54	4.99	2.26	1.68	1.84
-1 sigma	31.69	12.61	5.98	3.31	2.41	2.25
median	43.34	16.75	7.80	4.07	2.96	2.49
+1 sigma	56.49	22.40	10.43	5.79	4.05	3.37
+2 sigma	73.04	30.09	14.34	8.09	5.74	4.63
M_{TH} [TeV]	2.50	2.75	3.00	4.00	5.00	
Invariant mass cut [TeV]	2.25	2.48	2.70	3.60	4.50	
Observed upper limit [fb]	2.52	2.56	2.53	2.57	2.55	
Expected upper limit [fb]						
-2 sigma	2.16	2.30	2.38	2.34	2.21	
-1 sigma	2.41	2.50	2.48	2.51	2.50	
median	2.59	2.56	2.56	2.57	2.56	
+1 sigma	2.66	2.65	2.63	2.62	2.62	
+2 sigma	3.97	3.89	3.82	3.46	3.25	

Table 12.1. Observed and expected upper limits of cross section×branching-ratio of electron plus jet events as a function of M_{TH}.

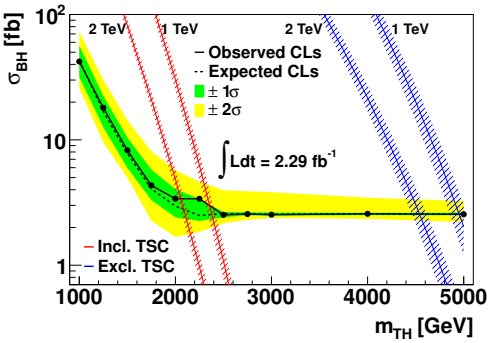

(a) 6 ADD-type extra dimensions

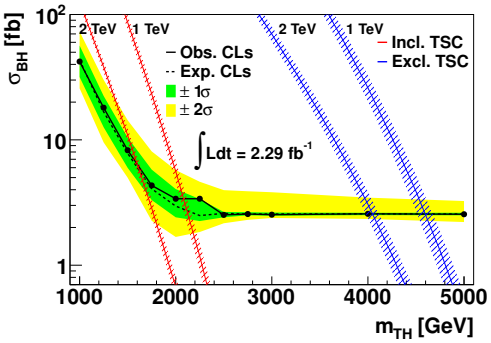

(b) 2 ADD-type extra dimensions

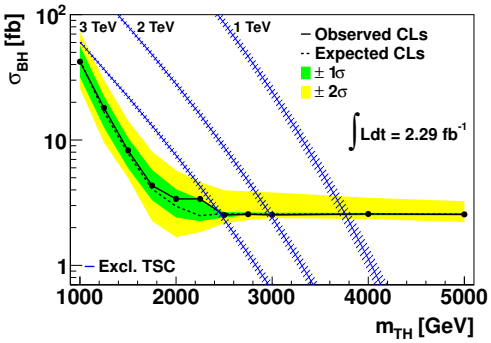

(c) RS-type extra dimension

Figure 12.1. Upper limits on cross section (1). Expected and observed upper limit of the cross section of lepton plus jet events without consideration of signal PDF uncertainty are given. As comparison, different predicted cross sections are shown for models with six and two ADD-type extra dimensions and for models assuming an RS-type extra dimension. The cross sections are given as a function of the minimum BH mass M_{TH} for different values of M_{PL} (as shown in the upper part of the diagrams). The hatched areas show the theoretical cross section uncertainty due to the CTEQ6.6 PDF uncertainties. For two and six extra ADD-type dimensions, cross-sections are shown with and without trapped surface calculations (TSC). For the calculation of the theoretical signal cross section, only BHs of charge 1/3 and 4/3 produced in interactions between two quarks (q-q) have been included. Some of the points may be unphysical, since M_{TH} is smaller then $x_{min} \times M_{Pl}$ with $x_{min} \geq 1$.

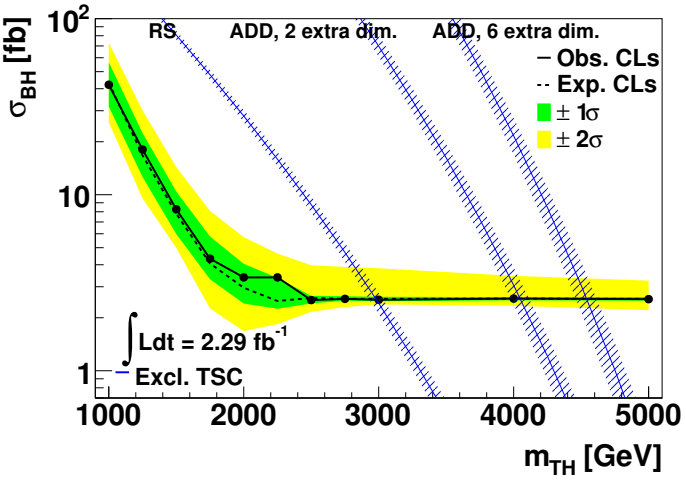

Figure 12.2. Upper limits on cross section (2). Expected and observed upper limit of the cross section of lepton plus jet events are displayed without consideration of signal PDF uncertainty. As comparison, different predicted cross sections are shown for models with a Planck mass of 2 TeV. The cross sections are given as a function of the minimum BH mass M_{TH} for different type and number of extra dimensions. The hatched area shows the theoretical cross section uncertainty due to the PDF uncertainties. CTEQ6.6 is used as PDF and the uncertainties are derived by considering its 44 PDF eigenvectors. All cross sections are shown for models without considering trapped surface calculations. For the calculation of the theoretical signal cross section, only BHs of charge 1/3 and 4/3 produced in interactions between two quarks (q-q) have been included. Some of the points may be unphysical, since M_{TH} is smaller then $x_{min} \times M_{Pl}$ with $x_{min} \geq 1$.

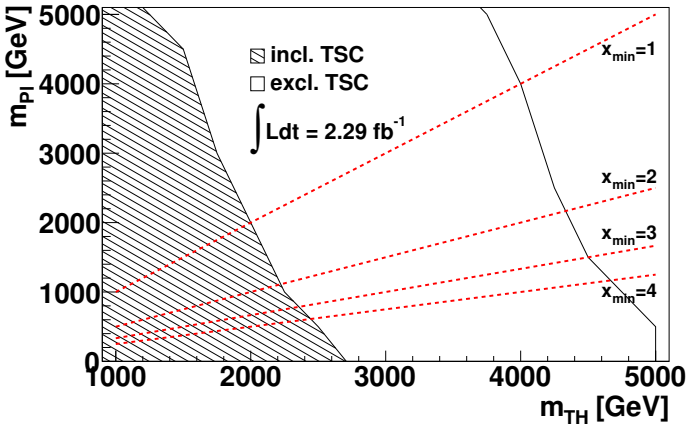

(a) 6 ADD-type EDs

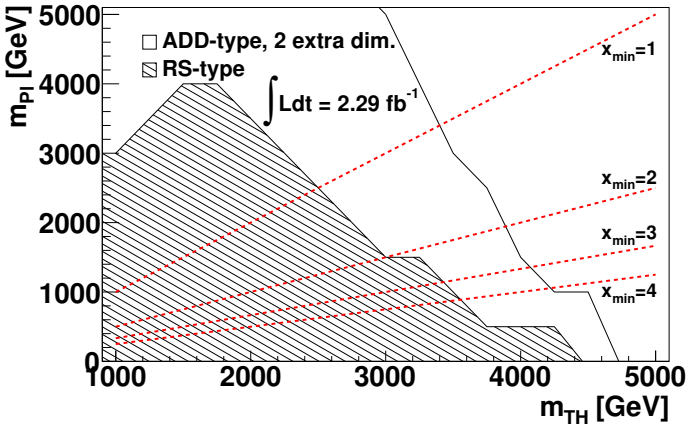

(b) 2 ADD-type EDs and RS-type ED

Figure 12.3. Excluded parameter space in M_{PL} and M_{TH} based on the observed upper limit on the cross section as a function of M_{TH}. The one sigma downward fluctuation of the cross section for each combination of parameters is used to exclude different models. Combinations of M_{Pl} and M_{TH} for different values of x_{min} are shown. Depending on the assumption of x_{min}, only points below the corresponding line are physical.

CHAPTER XIII

SUMMARY AND CONCLUSION

A search for events with one electron and one jet at high invariant mass has been conducted using data corresponding to $2.29\,\mathrm{fb}^{-1}$ at the ATLAS experiment. No excess over the expected Standard Model (SM) background has been observed. The largest discrepancy has been seen in events with an invariant mass selection of 2.03 TeV, corresponding to models with M_{TH} of 2.25 TeV. In this mass region, the expected background is 0.30 ± 0.04 (stat.) $\pm$ 0.13 (syst.), while 1 event has been observed. However, with a p-value of 0.26, the background-only hypothesis can not be rejected.

Limits have been set on the cross section of black holes decaying to lepton plus jet as function of invariant mass (see figure 12.1.). BH models with a minimum mass larger than or equal to 2.5 TeV and a cross section times branching fraction above 2.6 fb for the BH decaying to one electron and one jet are excluded at the 95% confidence level.

Recommended Future Work

This analysis can be extended to the full 2011 data recorded by the ATLAS experiment. This will add data corresponding to up to $5.25\,\mathrm{fb}^{-1}$ to be analyzed. In addition, the 2012 data, which are being recorded of the time of this writing, is expected to correspond to $16\,\mathrm{fb}^{-1}$ with a center-of-mass energy of 8 TeV. Using the same method described herein will improve the upper limits significantly. At 7 TeV, assuming that data will be recorded corresponding to $16\,\mathrm{fb}^{-1}$, the expected number of events in the signal region above 2.75 TeV from background only contributions is zero. This results in an upper limit of the number of signal events of about three events. Assuming a signal acceptance of 51%, three events corresponds to an upper limit on the cross section times branching fraction of $0.37\,\mathrm{fb}^{-1}$, improving the limit of this analysis by a factor of 7. An increase of the center-of-mass energy to 8 TeV will slightly worsen this limit. However, the predicted theoretical cross section is significantly higher as for 7 TeV, improving the potential exclusion range significantly.

Another way to improve the cross section limits of quantum BHs decaying to lepton-jet final states is the study of the muon+jet and hadronically decaying tau+jet decay channel. Tau+jet events are expected to have a large QCD background, due to the high probability of QCD jets to fake hadronically decaying taus. However, for the muon-jet final state, the background is expected to be

much smaller. In combination with the electron+jet analysis, this can potentially improve the limit on quantum black holes decaying to lepton+jet by a factor of two.

APPENDIX A

DESCRIPTION OF DATASETS

2011 Data

The recorded data has been reconstructed with release 16.6. of the ATLAS ATHENA framework. The detailed list of all data samples is shown in table A.1.

sample name
data11_7TeV.periodB.NoGRL.physics_Egamma.NTUP_SMWZ.p605
data11_7TeV.periodD.NoGRL.physics_Egamma.NTUP_SMWZ.p605
data11_7TeV.periodE.NoGRL.physics_Egamma.NTUP_SMWZ.p605
data11_7TeV.periodF.NoGRL.physics_Egamma.NTUP_SMWZ.p605
data11_7TeV.periodG.NoGRL.physics_Egamma.NTUP_SMWZ.p605
data11_7TeV.periodH.NoGRL.physics_Egamma.NTUP_SMWZ.p605
data11_7TeV.periodI.NoGRL.physics_Egamma.NTUP_SMWZ.p605
data11_7TeV.periodJ.NoGRL.physics_Egamma.NTUP_SMWZ.p605
data11_7TeV.periodK.NoGRL.physics_Egamma.NTUP_SMWZ.p605

Table A.1. List of data samples used in this analysis.

Monte Carlo Samples

The list of MC datasets that were used in this analysis are shown in table A.2. The samples are generated in release 15 of the ATLAS ATHENA framework. The detector response is simulated using Geant4 [101] in release 16.6. The same release is used for event reconstruction and object identification.

MC sample	Number of events	cross section [nb]	generator efficiency
Pythia QCD events, reconstructed jet p_T >240 GeV	997097	6.27	4.3295×10^{-1}
MC@NLO $t\bar{t}$, not full hadronic decay	14957047	1.44×10^{-1}	5.56×10^{-1}
MC@NLO $t\bar{t}$, full hadronic decay	1198875	1.44×10^{-1}	4.45×10^{-1}
MC@NLO single top, t-channel	299897	7.12×10^{-3}	1.0
MC@NLO single top, s-channel	299831	4.69×10^{-4}	1.0
Pythia $Z \to e^+e^-$, inclusive	299958	8.55×10^{-1}	9.74×10^{-1}
Alpgen $Z \to e^+e^-$ + 0 jets	6612265	6.70×10^{-1}	1.0
Alpgen $Z \to e^+e^-$ + 1 jet	1333745	1.34×10^{-1}	1.0
Alpgen $Z \to e^+e^-$ + 2 jets	404873	4.07×10^{-2}	1.0
Alpgen $Z \to e^+e^-$ + 3 jets	109942	1.13×10^{-2}	1.0
Alpgen $Z \to e^+e^-$ + 4 jets	29992	2.86×10^{-3}	1.0
Alpgen $Z \to e^+e^-$ + $\geq$5 jets	8992	7.59×10^{-4}	1.0
Alpgen $W \to e\nu$ + 0 jets	3455037	6.92	1.0
Alpgen $W \to e\nu$ + 1 jet	2499513	1.30	1.0
Alpgen $W \to e\nu$ + 2 jets	3768265	3.78×10^{-1}	1.0
Alpgen $W \to e\nu$ + 3 jets	1009641	1.02×10^{-1}	1.0
Alpgen $W \to e\nu$ + 4 jets	249869	2.57×10^{-2}	1.0
Alpgen $W \to e\nu$ + $\geq$5 jets	69953	7.02×10^{-3}	1.0
Alpgen $W \to \tau\nu$ + 0 jets	3416438	6.92	1.0
Alpgen $W \to \tau\nu$ + 1 jet	2499223	1.30	1.0
Alpgen $W \to \tau\nu$ + 2 jets	3768750	3.78×10^{-1}	1.0
Alpgen $W \to \tau\nu$ + 3 jets	1009548	1.02×10^{-1}	1.0
Alpgen $W \to \tau\nu$ + 4 jets	249853	2.57×10^{-1}	1.0
Alpgen $W \to \tau\nu$ + $\geq$5 jets	63692	6.99×10^{-3}	1.0
Alpgen $Z \to \tau^+\tau^-$ + 0 jets	6618801	6.7×10^{-1}	1.0
Alpgen $Z \to \tau^+\tau^-$ + 1 jet	1334664	1.35×10^{-1}	1.0
Alpgen $Z \to \tau^+\tau^-$ + 2 jets	404853	4.08×10^{-2}	1.0
Alpgen $Z \to \tau^+\tau^-$ + 3 jets	109944	1.13×10^{-2}	1.0
Alpgen $Z \to \tau^+\tau^-$ + 4 jets	29982	2.84×10^{-3}	1.0
Alpgen $Z \to \tau^+\tau^-$ + $\geq$5 jets	9993	7.61×10^{-4}	1.0
Herwig WZ di-boson	249923	1.12×10^{-2}	3.08×10^{-1}
Herwig WW di-boson	2495756	2.96×10^{-2}	3.88×10^{-1}
Herwig ZZ di-boson	249906	4.60×10^{-3}	2.12×10^{-1}
Pythia $b\bar{b}$, reconstructed electron with $p_T > 15$ GeV	4473875	7.74×10^{1}	0.9
Pythia $c\bar{c}$, reconstructed electron with $p_T > 15$ GeV	1494552	2.77×10^{1}	0.9

Table A.2. List of background MC samples used in the analysis.

APPENDIX B

DETAILED CUT FLOW

In the following, the number of events passing each selection requirement is shown for data and all MC samples individually. Table B.1. shows the number of events passing each signal selection requirement for each MC sample individually. The number of events passing the various invariant mass requirements, after all other signal selections are made, is shown in table B.2. for each MC sample. For the low invariant mass regions, the number of MC simulated events and observed events are shown in table B.3. All numbers are normalized to the integrated luminosity.

MC sample	Basic selection	Electron p_T	Jet p_T	$\Delta\phi$	$\Delta\eta$	isolation
$t\bar{t}$, not all hadronic	9.1e+03	5.8e+03	3.6e+03	3.2e+03	2.5e+03	2.4e+03
$t\bar{t}$, full hadronic	5.7e+02	42	29	27	20	9.3
single top, s-channel	5.5e+02	3.1e+02	1.4e+02	1.3e+02	84	81
single top, t-channel	50	27	16	15	14	13
$W \to e\nu$ + 0 jets	3.9e+03	1.8e+03	0	0	0	0
$W \to e\nu$ + 1 jets	4.7e+04	2.2e+04	1.0e+04	1.0e+04	8.9e+03	8.9e+03
$W \to e\nu$ + 2 jets	3.7e+04	1.9e+04	9.0e+03	9.0e+03	7.4e+03	7.3e+03
$W \to e\nu$ + 3 jets	1.7e+04	9e+03	4.9e+03	4.8e+03	3.9e+03	3.8e+03
$W \to e\nu$ + 4 jets	5.8e+03	3.1e+03	1.9e+03	1.9e+03	1.4e+03	1.4e+03
$W \to e\nu$ + $>$ 4 jets	1.9e+03	1.0e+03	7.4e+02	6.9e+02	5.2e+02	4.8e+02
$Z \to e^+e^-$ + 0 jets	1.6e+03	8.3e+02	7.6e+02	7.6e+02	6.7e+02	6.7e+02
$Z \to e^+e^-$ + 1 jet	1.4e+04	6.3e+03	2.9e+03	2.8e+03	2.5e+03	2.5e+03
$Z \to e^+e^-$ + 2 jets	1.1e+04	5.2e+03	2.4e+03	2.4e+03	2e+03	1.9e+03
$Z \to e^+e^-$ + 3 jets	4.7e+03	2.4e+03	1.3e+03	1.2e+03	1.0e+03	9.6e+02
$Z \to e^+e^-$ + 4 jets	1.6e+03	8.2e+02	5.0e+02	4.6e+02	3.6e+02	3.4e+02
$Z \to e^+e^-$ + $>$ 4 jets	5.3e+02	2.6e+02	1.8e+02	1.6e+02	1.2e+02	1.1e+02
$W \to \tau\nu$ + 0 jets	1.6e+02	24	0	0	0	0
$W \to \tau\nu$ + 1 jets	1.6e+03	3.3e+02	2.3e+02	2.3e+02	2.0e+02	2.0e+02
$W \to \tau\nu$ + 2 jets	1.7e+03	3.6e+02	2.4e+02	2.4e+02	2.0e+02	1.9e+02
$W \to \tau\nu$ + 3 jets	1.0e+03	2.2e+02	1.7e+02	1.7e+02	1.3e+02	1.2e+02
$W \to \tau\nu$ + 4 jets	4.5e+02	93	69	69	54	50
$W \to \tau\nu$ + $>$ 4 jets	1.7e+02	37	31	30	25	21
$Z \to \tau^+\tau^-$ + 0 jets	72	19	8.2	8.2	6.8	6.8
$Z \to \tau^+\tau^-$ + 1 jet	4.1e+02	95	65	65	57	55
$Z \to \tau^+\tau^-$ + 2 jets	4.3e+02	1.1e+02	80	80	67	64
$Z \to \tau^+\tau^-$ + 3 jets	2.3e+02	50	40	40	33	30
$Z \to \tau^+\tau^-$ + 4 jets	97	20	17	17	14	13
$Z \to \tau^+\tau^-$ + $>$ 4 jets	33	12	8.8	8.8	7.1	6.5
WZ	3.2e+02	1.8e+02	68	65	43	42
WW	8.7e+02	4.7e+02	1.9e+02	1.8e+02	1.4e+02	1.4e+02
ZZ	1.3e+02	72	29	27	21	20
$b\bar{b}$	2.7e+04	3.6e+03	2.3e+03	2.3e+03	1.9e+03	7.3e+02
$c\bar{c}$	2.3e+04	2.5e+03	1.8e+03	1.8e+03	8.8e+02	2.9e+02

Table B.1. Cut flow for non-QCD MC. The number of events after each signal region selection, with the exception of the invariant mass cut, are shown for each MC sample normalized to the integrated luminosity. The cuts shown are cumulative: For each column, all selections to the left are applied. For the number of events after the invariant mass selections, see table B.2.

M_{TH} [TeV]	1.00	1.25	1.50	1.75	2.00	2.25	2.50	2.75	3.00	4.00	5.00
invariant mass cut [TeV]	0.90	1.13	1.35	1.58	1.80	2.03	2.25	2.48	2.70	3.60	4.50
$t\bar{t}$, not all hadronic	1.8	0.27	0.058	0.039	0	0	0	0	0	0	0
$t\bar{t}$, full hadronic	0	0	0	0	0	0	0	0	0	0	0
single top, s-channel	0	0	0	0	0	0	0	0	0	0	0
single top, t-channel	0.0031	0	0	0	0	0	0	0	0	0	0
$W \to e\nu$ + 0 jets	0	0	0	0	0	0	0	0	0	0	0
$W \to e\nu$ + 1 jets	4.8	1.1	0	0	0	0	0	0	0	0	0
$W \to e\nu$ + 2 jets	19	5.1	1.1	0.14	0	0	0	0	0	0	0
$W \to e\nu$ + 3 jets	20	3.2	0.52	0	0	0	0	0	0	0	0
$W \to e\nu$ + 4 jets	10	2.8	0.67	0.67	0.52	0	0	0	0	0	0
$W \to e\nu$ + $>$ 4 jets	1.9	0.67	0	0	0	0	0	0	0	0	0
$Z \to e^+e^-$ + 0 jets	0.33	0.15	0.14	0	0	0	0	0	0	0	0
$Z \to e^+e^-$ + 1 jet	4.0	0.82	0.49	0	0	0	0	0	0	0	0
$Z \to e^+e^-$ + 2 jets	5.8	0.5	0.00025	0	0	0	0	0	0	0	0
$Z \to e^+e^-$ + 3 jets	2.9	0.79	0.045	0	0	0	0	0	0	0	0
$Z \to e^+e^-$ + 4 jets	1.9	0.19	0	0	0	0	0	0	0	0	0
$Z \to e^+e^-$ + $>$ 4 jets	1.4	0.74	0.62	0	0	0	0	0	0	0	0
$W \to \tau\nu$ + 0 jets	0	0	0	0	0	0	0	0	0	0	0
$W \to \tau\nu$ + 1 jets	0	0	0	0	0	0	0	0	0	0	0
$W \to \tau\nu$ + 2 jets	0	0	0	0	0	0	0	0	0	0	0
$W \to \tau\nu$ + 3 jets	0.50	0.50	0.50	0	0	0	0	0	0	0	0
$W \to \tau\nu$ + 4 jets	0.14	0	0	0	0	0	0	0	0	0	0
$W \to \tau\nu$ + $>$ 4 jets	0	0	0	0	0	0	0	0	0	0	0
$Z \to \tau^+\tau^-$ + 0 jets	0	0	0	0	0	0	0	0	0	0	0
$Z \to \tau^+\tau^-$ + 1 jet	0.50	0	0	0	0	0	0	0	0	0	0
$Z \to \tau^+\tau^-$ + 2 jets	0	0	0	0	0	0	0	0	0	0	0
$Z \to \tau^+\tau^-$ + 3 jets	0	0	0	0	0	0	0	0	0	0	0
$Z \to \tau^+\tau^-$ + 4 jets	0.0071	0	0	0	0	0	0	0	0	0	0
$Z \to \tau^+\tau^-$ + $>$ 4 jets	0.25	0	0	0	0	0	0	0	0	0	0
WZ	0.19	0.028	0	0	0	0	0	0	0	0	0
WW	0.48	0.15	0.081	0.015	0.002	0	0	0	0	0	0
ZZ	0.09	0.063	0.0053	0	0	0	0	0	0	0	0
$b\bar{b}$	0	0	0	0	0	0	0	0	0	0	0
$c\bar{c}$	0	0	0	0	0	0	0	0	0	0	0

Table B.2. Number of MC events in signal regions with different minimum mass thresholds for each MC sample (normalized to integrated luminosity).

Source	medium electron	loose only electron	photons
$t\bar{t}$, not all hadronic	3.0	0.17	0.21
$t\bar{t}$, full hadronic	0.061	0.36	0.33
single top, s-channel	0.57	0.038	0.067
single top, t-channel	0.0067	0.00016	0.00042
$W \to e\nu$ + 0 jets	0	0	0
$W \to e\nu$ + 1 jets	7.8e+02	15	24
$W \to e\nu$ + 2 jets	2.1e+02	8.0	8.6
$W \to e\nu$ + 3 jets	1.5e+02	5.8	8.7
$W \to e\nu$ + 4 jets	66	2.7	3.7
$W \to e\nu$ + $>$ 4 jets	27	1.2	1.3
$Z \to e^+e^-$ + 0 jets	14	1.2	1.0
$Z \to e^+e^-$ + 1 jet	48	2.3	2.3
$Z \to e^+e^-$ + 2 jets	57	2.4	2.4
$Z \to e^+e^-$ + 3 jets	34	1.4	1.4
$Z \to e^+e^-$ + 4 jets	16	0.90	0.34
$Z \to e^+e^-$ + $>$ 4 jets	5.0	0.39	0.47
$W \to \tau\nu$ + 0 jets	0	0	0
$W \to \tau\nu$ + 1 jets	39	13	16
$W \to \tau\nu$ + 2 jets	5.8	3.1	3.6
$W \to \tau\nu$ + 3 jets	5.9	2.4	2.5
$W \to \tau\nu$ + 4 jets	2.1	0.93	0.98
$W \to \tau\nu$ + $>$ 4 jets	1.2	0.53	0.51
$Z \to \tau^+\tau^-$ + 0 jets	0.079	0.086	0
$Z \to \tau^+\tau^-$ + 1 jet	1.3	0.63	0.53
$Z \to \tau^+\tau^-$ + 2 jets	2.1	0.81	0.85
$Z \to \tau^+\tau^-$ + 3 jets	1.3	0.13	0.37
$Z \to \tau^+\tau^-$ + 4 jets	0.76	0.34	0.58
$Z \to \tau^+\tau^-$ + $>$ 4 jets	0.19	0.068	0.12
WZ	0.22	0.0067	0.0081
WW	0.2	0.0080	0.0076
ZZ	0.024	0.00092	0.0015
$b\bar{b}$	0	1.4e+03	0
$c\bar{c}$	0	1.6e+04	49
Observed	6.2e+03	2.2e+04	7.7e+03

Table B.3. Number of events in the low invariant mass regions from various MC samples normalized to the integrated luminosity.

APPENDIX C

SIGNAL REGION PLOTS FOR DIFFERENT INVARIANT MASS SELECTIONS

In figures C.1.-C.4. and figures C.5.-C.8., the signal region distributions are shown for a minimum mass requirement of 0.9 TeV and 1.8 TeV, respectively, corresponding to M_{TH} of 1 TeV and 2.0 TeV. In all figures showing the signal region only in this section, the signal is normalized to a cross section of 5 fb.

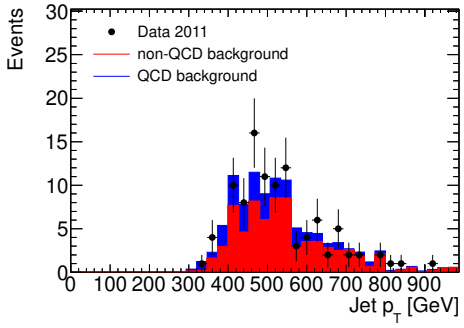

(a) Leading jet p_T

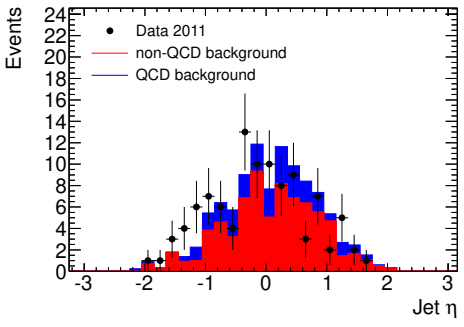

(b) Leading jet η

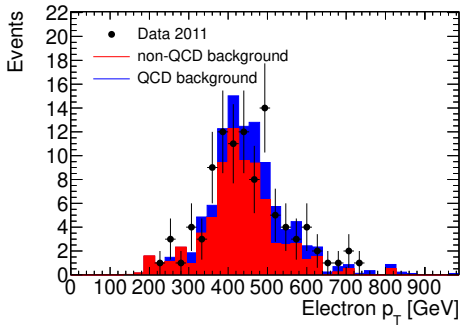

(c) Leading electron p_T

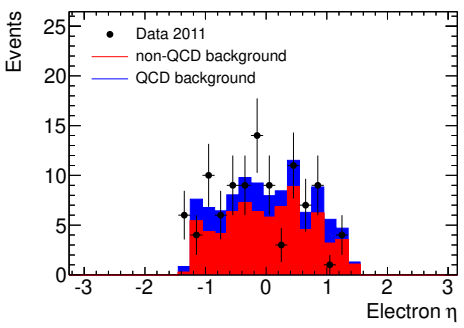

(d) Leading electron η

Figure C.1. Distributions in signal region ($M_{TH} = 1\,\text{TeV}$) (1). Various distributions in the signal region are shown for the expected background and observation. The QCD contribution has been estimated from data using loose only electrons and non-QCD contribution from MC. Both are normalized using the normalization factor from the fit in the low invariant mass region. The minimum invariant mass requirement is 0.9 TeV.

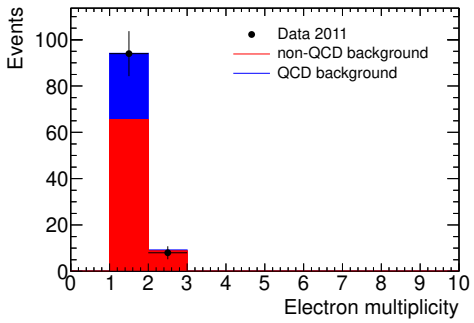

(a) Lepton multiplicity

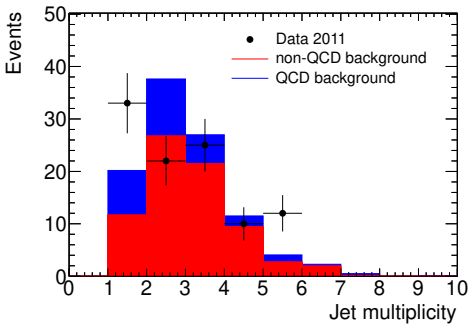

(b) Jet multiplicity

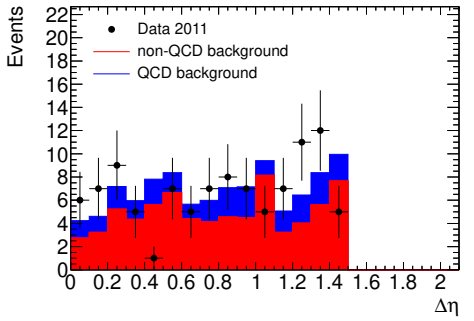

(c) $\Delta\eta$ between electron and jet

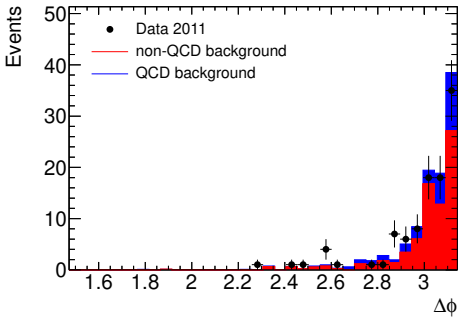

(d) $\Delta\phi$ between electron and jet

Figure C.2. Distributions in signal region ($M_{TH} = 1\,\text{TeV}$) (2). Various distributions in the signal region are shown for the expected background and observation. The QCD contribution has been estimated from data using loose only electrons and non-QCD contribution from MC. Both are normalized using the normalization factor from the fit in the low invariant mass region. The minimum invariant mass requirement is 0.9 TeV.

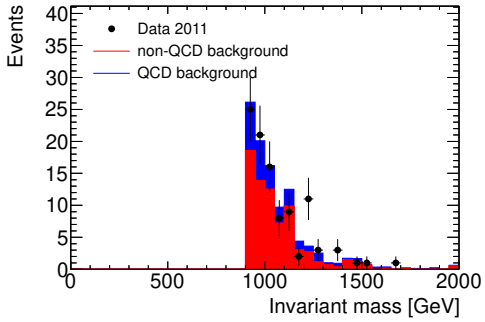

(a) invariant mass of electron/jet

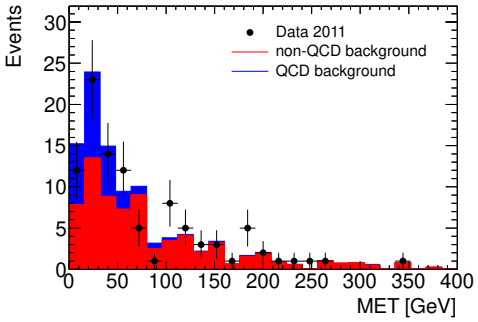

(b) Missing transverse energy

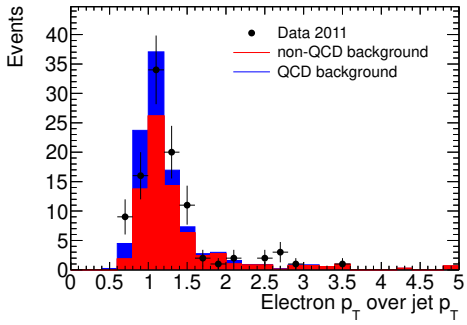

(c) Ratio of electron p_T and jet p_T

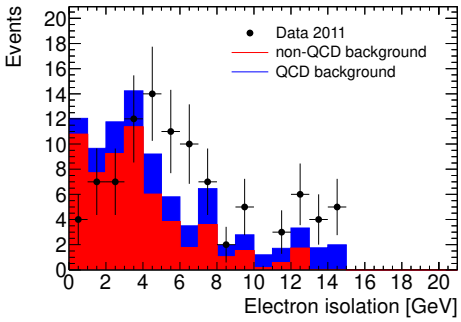

(d) Isolation of leading electron

Figure C.3. Distributions in signal region (M_{TH} = 1 TeV) (3). Various distributions in the signal region are shwon for the expected background and observation. The QCD contribution has been estimated from data using loose only electrons and non-QCD contribution from MC. Both are normalized using the normalization factor from the fit in the low invariant mass region. The minimum invariant mass requirement is 0.9 TeV.

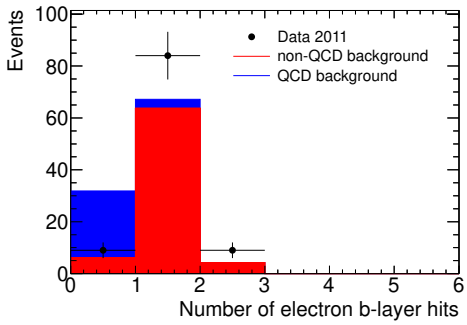

(a) Number of electron b-layer hits

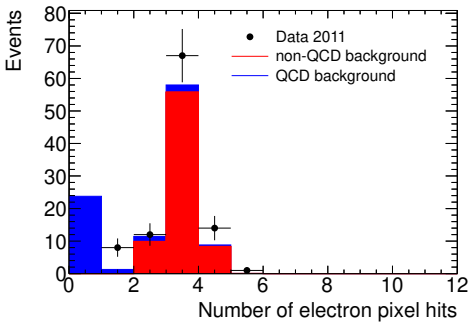

(b) Number of electron pixel hits

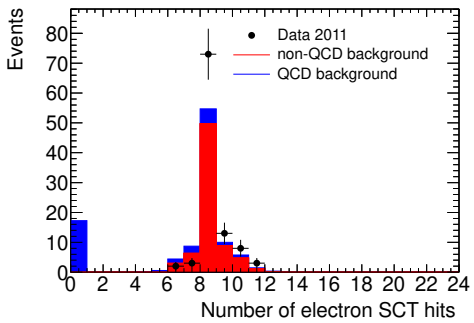

(c) Number of electron SCT hits

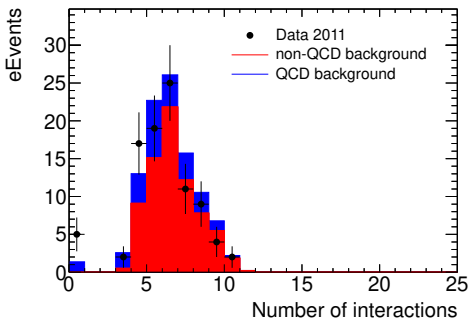

(d) Number of average interactions per bunch crossing

Figure C.4. Distributions in signal region ($M_{TH} = 1\,\text{TeV}$) (4). Various distributions in the signal region are shown for the expected background and observation. The QCD contribution has been estimated from data using loose only electrons and non-QCD contribution from MC. Both are normalized using the normalization factor from the fit in the low invariant mass region. The minimum invariant mass requirement is 0.9 TeV. The number of b-layer, pixel and SCT hits is zero for most of the QCD background (for loose only electrons), since hits are required for the medium selection, but not for loose ID.

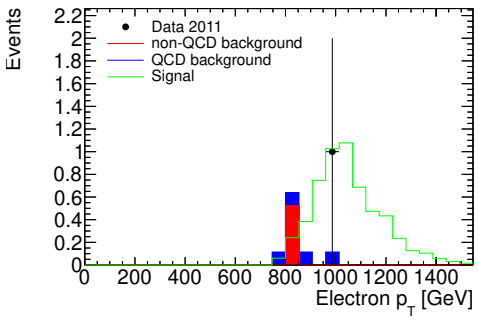

(a) Leading electron p_T

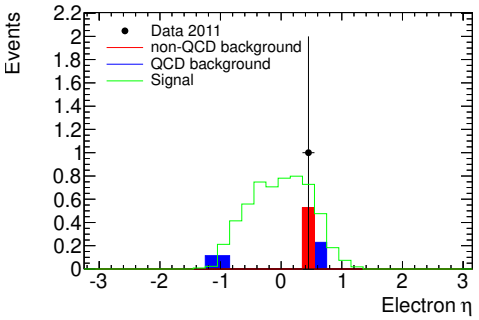

(b) Leading electron η

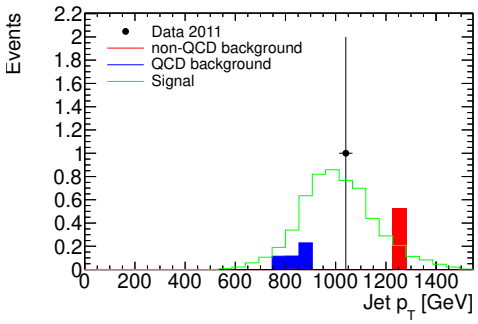

(c) Leading jet p_T

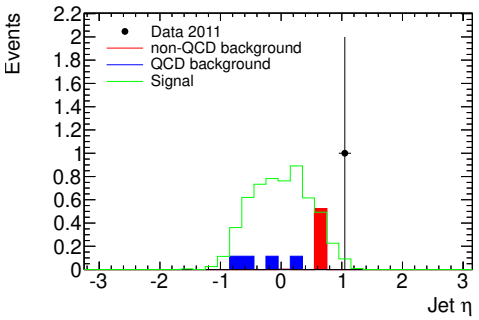

(d) Leading jet η

Figure C.5. Distributions in signal region ($M_{TH} = 2\,\text{TeV}$) (1). Various distributions in the signal region are shown for the expected background and observation. The QCD contribution has been estimated from data using loose only electrons and non-QCD contribution from MC. Both are normalized using the normalization factor from the fit in the low invariant mass region. The minimum invariant mass requirement is 1.8 TeV. A signal sample is overlaid for comparison, normalized to $\sigma = 5\,\text{fb}$.

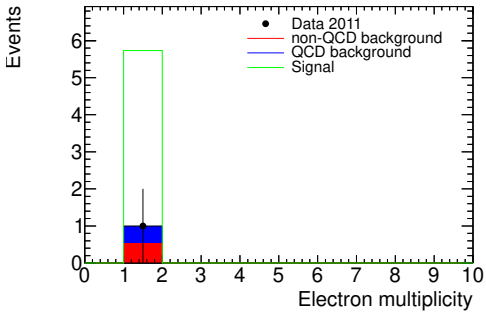

(a) Lepton multiplicity

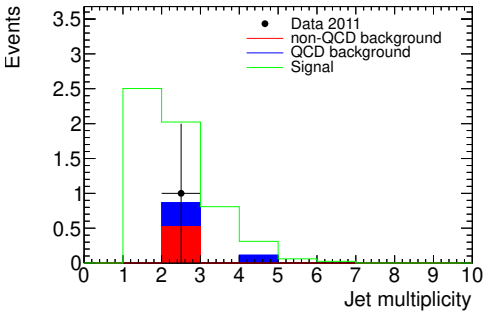

(b) Jet multiplicity

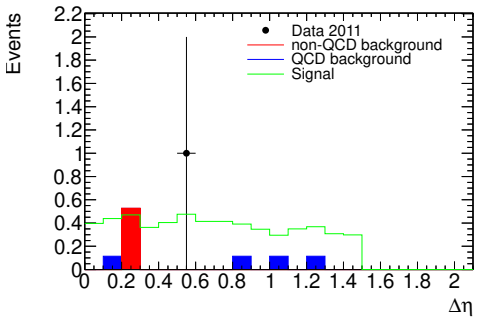

(c) $\Delta\eta$ between electron and jet

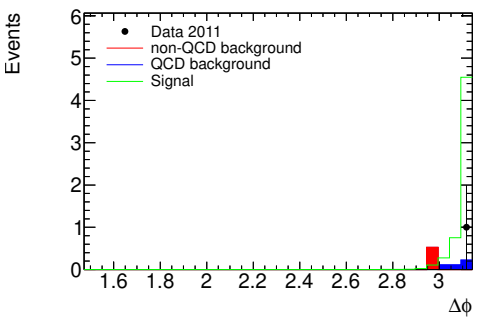

(d) $\Delta\phi$ between electron and jet

Figure C.6. Distributions in signal region ($M_{TH} = 2\,\text{TeV}$) (2). Various distributions in the signal region are shown for the expected background and observation. The QCD contribution has been estimated from data using loose only electrons and non-QCD contribution from MC. Both are normalized using the normalization factor from the fit in the low invariant mass region. The minimum invariant mass requirement is 1.8 TeV. A signal sample is overlaid for comparison, normalized to $\sigma = 5\,\text{fb}$.

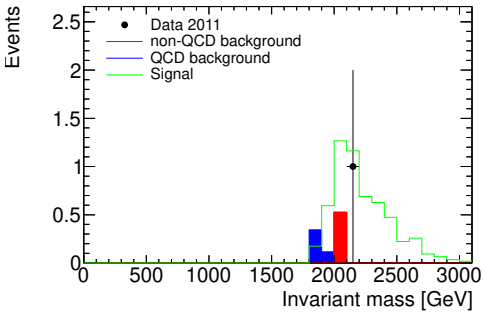

(a) invariant mass of electron/jet

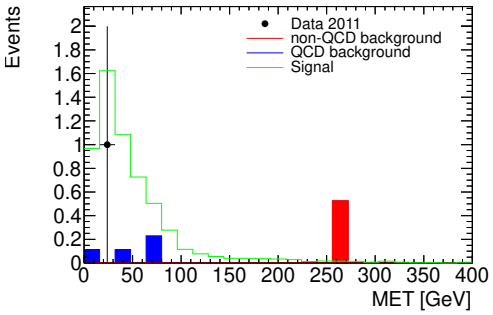

(b) Missing transverse energy

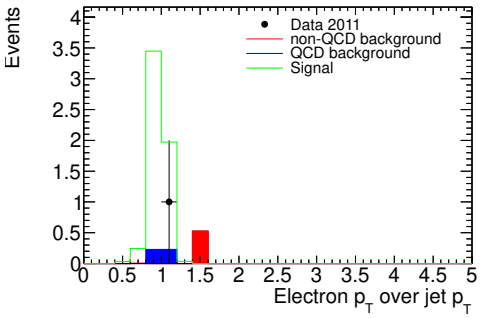

(c) Ratio of electron p_T and jet p_T

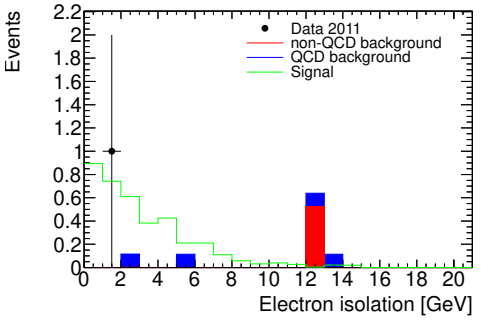

(d) Isolation of leading electron

Figure C.7. Distributions in signal region ($M_{TH} = 2\,\text{TeV}$) (3). Various distributions in the signal region are shown for the expected background and observation. The QCD contribution has been estimated from data using loose only electrons and non-QCD contribution from MC. Both are normalized using the normalization factor from the fit in the low invariant mass region. The minimum invariant mass requirement is 1.8 TeV. A signal sample is overlaid for comparison, normalized to $\sigma = 5\,\text{fb}$.

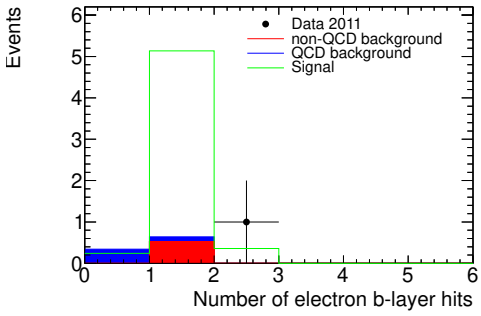

(a) Number of electron b-layer hits

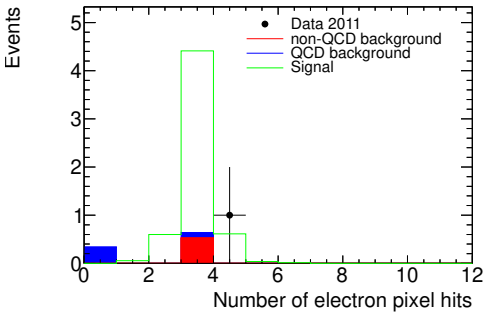

(b) Number of electron pixel hits

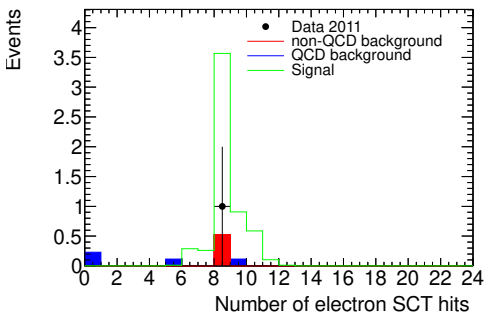

(c) Number of electron SCT hits

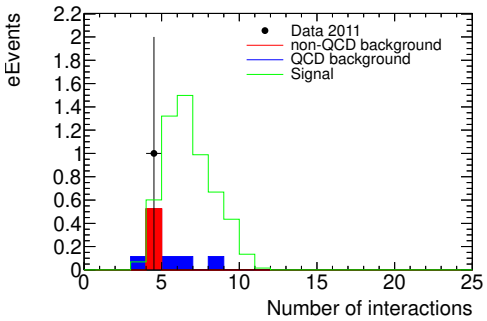

(d) Number of average interactions per bunch crossing

Figure C.8. Distributions in signal region ($M_{TH} = 2\,\text{TeV}$) (4). Various distributions in the signal region are shown for the expected background and observation. The QCD contribution has been estimated from data using loose only electrons and non-QCD contribution from MC. Both are normalized using the normalization factor from the fit in the low invariant mass region. The minimum invariant mass requirement is 1.8 TeV. A signal sample is overlaid for comparison, normalized to $\sigma = 5\,\text{fb}$. The number of b-layer, pixel and SCT hits is zero for most of the QCD background (for loose only electrons), since hits are required for the medium selection, but not for loose ID.

APPENDIX D

DETAILS OF OBSERVED EVENTS IN THE SIGNAL REGION

There are a total of seven observed events with an invariant mass of 1.35 TeV or higher. Their details are listed below:

- Run number: 182486, Event number: 41226166, BH mass point studied: 1.5e+06 GeV, BH mass threshold: 1.35e+06 GeV.

  Leading lepton: p_T: 6.9e+02 GeV, η: 0.82, ϕ: -1.4 , Electron isolation: 4.7 GeV, number of electron b-layer hits expected: 1, number of electron b-layer hits observed: 1 , Lepton passes tight ID: 1

  Leading jet: p_T: 6.2e+02 GeV, η: -0.58, ϕ: 1.8 , EMfrac: 0.63, p_T at EM scale: 5.0e+02, η at EM scale: -0.58 , Timing: 0.14, LAr quality: 0.076, sumPtTrk: 4.6e+05, HEC quality: 0, negative energy: 0, fracSamplingMax: 0.4 , hecf: 0, isBadLoose: 0

  Event info: Invariant mass: 1.7e+03 GeV, transverse mass: 4.9e+02 GeV, $\Delta\phi$: 3.1, $\Delta\eta$ 1.4 , MET: 56 GeV, ϕ of MET: -1.5

  Other info:

  Second leading jet: p_T: 1.4e+02 GeV, η: -1.4, ϕ: 1.1

Third leading jet: p_T: 34 GeV, η: -0.15, ϕ: -0.83

- Run number: 183780, Event number: 97982668, BH mass point studied: 1.5e+06 GeV, BH mass threshold: 1.4e+06 GeV.

  Leading lepton: p_T: 9.9e+02 GeV, η: 0.52, ϕ: -0.17 , Electron isolation: 1.2 GeV, number of electron b-layer hits expected: 1, number of electron b-layer hits observed: 2 , Lepton passes tight ID: 0

  Leading jet: p_T: 1.1e+03 GeV, η: 1.1, ϕ: 3.0 , EMfrac: 0.73, p_T at EM scale: 9.2e+02, η at EM scale: 1.1 , Timing: 0.54, LAr quality: 0.16, sumPtTrk: 3.7e+05, HEC quality: 0, negative energy: 0, fracSamplingMax: 0.52 , hecf: 0, isBadLoose: 0

  Event info: Invariant mass: 2.2e+03 GeV, transverse mass: 75 GeV, $\Delta\phi$: 3.1, $\Delta\eta$ 0.59 , MET: 22 GeV, ϕ of MET: 0.069

  Other info:

  Second leading jet: p_T: 27 GeV, η: -1.2, ϕ: -1

- Run number: 185649, Event number: 9069621, BH mass point studied: 1.5e+06 GeV, BH mass threshold: 1.4e+06 GeV.

  Leading lepton: p_T: 3.5e+02 GeV, η: 0.48, ϕ: 1.1 , Electron isolation: 7.4 GeV, number of electron b-layer hits expected: 1, number of electron b-layer hits observed: 1 , Lepton passes tight ID: 1

Leading jet: p_T: 9.2e+02 GeV, η: -0.76, ϕ: -2.1 , EMfrac: 0.79, p_T at EM scale: 7.5e+02, η at EM scale: -0.75 , Timing: 0.00033, LAr quality: 0.087, sumPtTrk: 1e+06, HEC quality: 0, negative energy: 0, fracSamplingMax: 0.48 , hecf: 0, isBadLoose: 0

Event info: Invariant mass: 1.4e+03 GeV, transverse mass: 9.4e+02 GeV, $\Delta\phi$: 3.1, $\Delta\eta$ 1.2 , MET: 1.8e+02 GeV, ϕ of MET: 1.3

Other info:

Second leading jet: p_T: 4.8e+02 GeV, η: -0.18, ϕ: 0.91

Third leading jet: p_T: 30 GeV, η: -1.6, ϕ: 2.1

- Run number: 186456, Event number: 33241133, BH mass point studied: 1.5e+06 GeV, BH mass threshold: 1.4e+06 GeV.

  Leading lepton: p_T: 6.1e+02 GeV, η: -0.43, ϕ: 3 , Electron isolation: 2.4 GeV, number of electron b-layer hits expected: 1, number of electron b-layer hits observed: 1 , Lepton passes tight ID: 1

  Leading jet: p_T: 7.1e+02 GeV, η: 0.14, ϕ: -0.14 , EMfrac: 0.28, p_T at EM scale: 5.8e+02, η at EM scale: 0.14 , Timing: 0.63, LAr quality: 0.12, sumPtTrk: 1.8e+05, HEC quality: 0, negative energy: 0, fracSamplingMax: 0.39 , hecf: 0, isBadLoose: 0

  Event info: Invariant mass: 1.4e+03 GeV, transverse mass: 7e+02 GeV, $\Delta\phi$: 3.1, $\Delta\eta$ 0.57 , MET: 1e+02 GeV, ϕ of MET: -0.96

Other info:

Second leading jet: p_T: 1.4e+02 GeV, η: -0.14, ϕ: 2.2

- Run number: 186216, Event number: 5438312, BH mass point studied: 1.5e+06 GeV, BH mass threshold: 1.4e+06 GeV.

  Leading lepton: p_T: 7.4e+02 GeV, η: -0.83, ϕ: 0.50 , Electron isolation: 5 GeV, number of electron b-layer hits expected: 1, number of electron b-layer hits observed: 1 , Lepton passes tight ID: 1

  Leading jet: p_T: 6.3e+02 GeV, η: -0.98, ϕ: -2.7 , EMfrac: 0.89, p_T at EM scale: 5.1e+02, η at EM scale: -1 , Timing: -0.14, LAr quality: 0.39, sumPtTrk: 3e+05, HEC quality: 0, negative energy: 0, fracSamplingMax: 0.63 , hecf: 0, isBadLoose: 0

  Event info: Invariant mass: 1.4e+03 GeV, transverse mass: 1e+02 GeV, $\Delta\phi$: 3.1, $\Delta\eta$ 0.15 , MET: 45 GeV, ϕ of MET: -2.5

  Other info:

  Second leading jet: p_T: 50 GeV, η: 0.043, ϕ: -2.3

  Third leading jet: p_T: 44 GeV, η: -1.4, ϕ: 0.33

- Run number: 186216, Event number: 43539228, BH mass point studied: 1.5e+06 GeV, BH mass threshold: 1.4e+06 GeV.

  Leading lepton: p_T: 6.2e+02 GeV, η: -0.0091, ϕ: 0.25 , Electron isolation:

12 GeV, number of electron b-layer hits expected: 1, number of electron b-layer hits observed: 1 , Lepton passes tight ID: 1

Leading jet: p_T: 7.9e+02 GeV, η: 0.66, ϕ: -2.9 , EMfrac: 0.70, p_T at EM scale: 6.5e+02, η at EM scale: 0.65 , Timing: 0.36, LAr quality: 0.11, sumPtTrk: 6.2e+05, HEC quality: 0, negative energy: 0, fracSamplingMax: 0.44 , hecf: 0, isBadLoose: 0

Event info: Invariant mass: 1.5e+03 GeV, transverse mass: 4.2e+02 GeV, $\Delta\phi$: 3.1, $\Delta\eta$ 0.67 , MET: 99 GeV, ϕ of MET: 0.27

Other info:

Second leading jet: p_T: 78 GeV, η: -0.63, ϕ: -0.46

Third leading jet: p_T: 69 GeV, η: -1.8, ϕ: 1.4

- Run number: 187219, Event number: 62399660, BH mass point studied: 1.5e+06 GeV, BH mass threshold: 1.4e+06 GeV.

  Leading lepton: p_T: 6e+02 GeV, η: -1.3, ϕ: 0.74 , Electron isolation: 13 GeV, number of electron b-layer hits expected: 1, number of electron b-layer hits observed: 1 , Lepton passes tight ID: 1

  Leading jet: p_T: 6.3e+02 GeV, η: 0.053, ϕ: -2.5 , EMfrac: 0.43, p_T at EM scale: 5e+02, η at EM scale: 0.062 , Timing: 1.2, LAr quality: 0.13, sumPtTrk: 3.5e+04, HEC quality: 0, negative energy: 0, fracSamplingMax: 0.36 , hecf: 0, isBadLoose: 0

Event info: Invariant mass: 1.5e+03 GeV, transverse mass: 1.0e+02 GeV, $\Delta\phi$: 3.0, $\Delta\eta$ 1.4 , MET: 22 GeV, ϕ of MET: -2.8

Other info:

Second leading jet: p_T: 87 GeV, η: -2.4, ϕ: -0.38

REFERENCES CITED

[1] D. Griffiths, *Introduction to Elementary Particles* (Wiley-VCH, 2008), 2nd ed.

[2] S. W. Herb, D. C. Hom, L. M. Lederman, J. C. Sens, H. D. Snyder, J. K. Yoh, J. A. Appel, B. C. Brown, C. N. Brown, W. R. Innes, et al., Phys. Rev. Lett. **39**, 252 (1977).

[3] F. A. et al. (The CDF Collaboration), Phys. Rev. Lett. **74**, 2626 (1995).

[4] S. Abachi et al. (The D0 Collaboration), Phys. Rev. Lett. **74**, 2422 (1995).

[5] K. Kodama, N. Ushida, C. Andreopoulos, N. Saoulidou, G. Tzanakos, P. Yager, B. Baller, D. Boehnlein, W. Freeman, B. Lundberg, et al., Physics Letters B **504**, 218 (2001).

[6] O. S. Brning, P. Collier, P. Lebrun, S. Myers, R. Ostojic, J. Poole, and P. Proudlock, *LHC Design Report* (CERN, Geneva, 2004).

[7] Tevatron I Group, *Design Report Tevatron 1 Project* (Batavia, Illinois, 1984).

[8] M. Srednicki, *Quantum Field Theory* (Cambridge University Press, 2007), 1st ed.

[9] R. P. Feynman, Phys. Rev. **76**, 769 (1949).

[10] Committee on Elementary-Particle Physics, National Research Council, *Elementary-Particle Physics: Revealing the Secrets of Energy and Matter* (The National Academies Press, 1998), ISBN 9780309060370.

[11] A. Barabash, Foundations of Physics **40**, 703 (2010).

[12] K. Nakamura and P. D. Group, J. Phys. G Nucl. Partic. **37**, 075021 (2010).

[13] G. Aad et al. (The ATLAS Collaboration), Phys. Lett. B **710**, 49 (2012), 1202.1408.

[14] S. Chatrchyan et al. (The CMS Collaboration) (2012), submitted to Physics Letters B, 1202.1488.

[15] T. Hnsch, J. Alnis, P. Fendel, M. Fischer, C. Gohle, M. Herrmann, R. Holzwarth, N. Kolachevsky, T. Udem, and M. Zimmermann, Philos. T. Roy. Soc. A **363**, 2155 (2005).

[16] I. W. Stewart, F. J. Tackmann, and W. J. Waalewijn, Phys. Rev. D **81**, 094035 (2010), 0910.0467.

[17] J. Pumplin, D. Stump, J. Huston, H. Lai, P. M. Nadolsky, et al., JHEP **0207**, 012 (2002), hep-ph/0201195.

[18] P. M. Nadolsky et al., Phys. Rev. D **78**, 013004 (2008), 0802.0007.

[19] A. Einstein, Ann. Phys. **49**, 769 (1916).

[20] S. Carroll, *Spacetime and Geometry: An Introduction to General Relativity* (Benjamin Cummings, 2003), ISBN 0805387323.

[21] G. Lepage (1989), hep-ph/0506330.

[22] S. P. Martin (1997), hep-ph/9709356.

[23] N. Arkani-Hamed, S. Dimopoulos, and G. R. Dvali, Phys. Lett. B **429**, 263 (1998), hep-ph/9803315.

[24] J. Einasto (2009), 0901.0632.

[25] A. H. Peter (2012), 1201.3942.

[26] G. Jungman, M. Kamionkowski, and K. Griest, Phys. Rept. **267**, 195 (1996), hep-ph/9506380.

[27] A. H. Peter (2012), submitted proceedings for the Frank N. Bash Symposium, October 9-11, 2011, 1201.3942.

[28] G. Bertone, Nature **468**, 389 (2010), 1011.3532.

[29] J. Frieman, M. Turner, and D. Huterer, Ann. Rev. Astron. Astrophys. **46**, 385 (2008), 0803.0982.

[30] R. N. Cahn, Rev. Mod. Phys. **68**, 951 (1996).

[31] S. I. Newton and E. Halley, *Philosophiae Naturalis Principia Mathematica, 1st ed.* (Jussu Societatis Regiae ac typis Josephi Streater, prostant venales apud Sam. Smith, London, UK, 1687).

[32] D. Kapner, T. Cook, E. Adelberger, J. Gundlach, B. R. Heckel, et al., Phys. Rev. Lett. **98**, 021101 (2007), hep-ph/0611184.

[33] N. Arkani-Hamed, S. Dimopoulos, and G. R. Dvali, Phys. Lett. B **429**, 263 (1998), hep-ph/9803315.

[34] L. Randall and R. Sundrum, Phys. Rev. Lett. **83**, 3370 (1999), hep-ph/9905221.

[35] X. Calmet, S. D. Hsu, and D. Reeb, Phys. Rev. D **77**, 125015 (2008), 0803.1836.

[36] I. Antoniadis, N. Arkani-Hamed, S. Dimopoulos, and G. R. Dvali, Phys. Lett. B **436**, 257 (1998), hep-ph/9804398.

[37] N. Arkani-Hamed, S. Dimopoulos, and G. R. Dvali, Phys. Rev. D **59**, 086004 (1999), hep-ph/9807344.

[38] J. D. Jackson, *Classical electrodynamics* (Wiley, New York, NY, 1999), 3rd ed., ISBN 9780471309321.

[39] L. J. Hall and D. Tucker-Smith, Phys. Rev. D **60**, 085008 (1999), hep-ph/9904267.

[40] S. Cullen and M. Perelstein, Phys. Rev. Lett. **83**, 268 (1999), hep-ph/9903422.

[41] V. D. Barger, T. Han, C. Kao, and R.-J. Zhang, Phys. Lett. B **461**, 34 (1999), hep-ph/9905474.

[42] C. Hanhart, D. R. Phillips, S. Reddy, and M. J. Savage, Nucl. Phys. B **595**, 335 (2001), nucl-th/0007016.

[43] C. Hanhart, J. A. Pons, D. R. Phillips, and S. Reddy, Phys. Lett. B **509**, 1 (2001), astro-ph/0102063.

[44] R. Allahverdi, C. Bird, S. Groot Nibbelink, and M. Pospelov, Phys. Rev. D **69**, 045004 (2004), hep-ph/0305010.

[45] S. Hannestad and G. G. Raffelt, Phys. Rev. Lett. **87**, 051301 (2001).

[46] S. Hannestad, Phys. Rev. D **64**, 023515 (2001).

[47] S. Hannestad and G. G. Raffelt, Phys. Rev. D **67**, 125008 (2003), hep-ph/0304029.

[48] M. Gogberashvili, A. S. Sakharov, and E. K. Sarkisyan, Phys. Lett. B **644**, 179 (2007), hep-ph/0605326.

[49] L. A. Anchordoqui, J. L. Feng, H. Goldberg, and A. D. Shapere, Phys. Rev. D **68**, 104025 (2003).

[50] P. Kanti, in *Physics of Black Holes*, edited by E. Papantonopoulos (Springer Berlin / Heidelberg, 2009), vol. 769 of *Lecture Notes in Physics*, pp. 387–423, ISBN 978-3-540-88459-0.

[51] S. B. Giddings and S. D. Thomas, Phys. Rev. D **65**, 056010 (2002), hep-ph/0106219.

[52] J. C. Baez and S. J. Olson, *Uncertainty in measurements of distance* (2002), gr-qc/0201030.

[53] H. Yoshino and V. S. Rychkov, Phys. Rev. D **71**, 104028 (2005).

[54] P. Meade and L. Randall, J. High Energ. Phys. **2008**, 003 (2008).

[55] R. Placakyte (2011), to appear in the proceedings of XXXI Physics in Collision, Vancouver, BC Canada, 1111.5452.

[56] D. N. Page, Phys. Rev. D **13**, 198 (1976).

[57] S. Dimopoulos and G. L. Landsberg, Phys. Rev. Lett. **87**, 161602 (2001), hep-ph/0106295.

[58] T. Aaltonen et al. (The CDF Collaboration), Phys. Rev. Lett. **101**, 181602 (2008), 0807.3132.

[59] V. Abazov et al. (The D0 Collaboration), Phys. Rev. Lett. **101**, 011601 (2008), 0803.2137.

[60] X. Calmet, W. Gong, and S. D. Hsu, Phys. Lett. B **668**, 20 (2008), 0806.4605.

[61] B. Aubert et al. (BABAR Collaboration), Phys. Rev. Lett. **93**, 191801 (2004), hep-ex/0408023.

[62] L. R. Evans, in *1996 European School of High-Energy Physics: Carry-le-Rouet, France, 1-14 September 1996 : proceedings* (CERN, Geneva, 1996).

[63] S. Chatrchyan et al. (The CMS Collaboration) (2012), submitted to Physics Letters B, 1202.3827.

[64] S. Chatrchyan et al. (The CMS Collaboration) (2011), 1112.0688.

[65] G. Aad et al. (The ATLAS Collaboration), Tech. Rep. ATLAS-CONF-2011-096, CERN, Geneva (2011).

[66] G. Aad et al. (The ATLAS Collaboration), New J. Phys. **13**, 053044 (2011), 1103.3864.

[67] G. Aad et al. (The ATLAS Collaboration) (2011), 1112.3580.

[68] G. Aad et al. (The ATLAS Collaboration), Phys. Lett. B **709**, 322 (2012), 1111.0080.

[69] G. Aad et al. (The ATLAS Collaboration), Journal of Instrumentation **3**, 8003 (2008).

[70] G. L. Bayatian, S. Chatrchyan, G. Hmayakyan, A. M. Sirunyan, W. Adam, T. Bergauer, M. Dragicevic, J. Ero, M. Friedl, R. Fruehwirth, et al. (The CMS Collaboration), *CMS Physics Technical Design Report Volume I: Detector Performance and Software*, Technical Design Report CMS (CERN, Geneva, 2006).

[71] G. Aad et al. (The ATLAS Collaboration), Phys. Lett. B **710**, 538 (2012), 1112.2194.

[72] J.-L. Caron (1998).

[73] M. Bajko, F. Bertinelli, N. Catalan-Lasheras, S. Claudet, P. Cruikshank, K. Dahlerup-Petersen, R. Denz, P. Fessia, C. Garion, J. Jimenez, et al., Tech. Rep. CERN-LHC-PROJECT-Report-1168, CERN, Geneva (2009).

[74] P. J. Lee, in *Wiley Encyclopedia of Electrical and Electronics Engineering*, edited by J. G. Webster (New York: Wiley, 1999), vol. 21, pp. 75–87.

[75] J. Pequenao (2008).

[76] J. Pequenao (2008).

[77] A. Airapetian, V. Cindro, A. Filipčič, G. Kramberger, M. Mikuž, M. Tadel, D. Žontar, et al. (The ATLAS Collaboration), *Inner Detector: Technical Design Report*, ATLAS Technical Design Report (CERN, Geneva, 1997), ISBN 9789290831020.

[78] J. Pequenao (2008).

[79] T. Ince, Ph.D. thesis, University of Victoria, Victoria, Canada (2010).

[80] B. Aubert, B. Beaugiraud, J. Colas, P. Delebecque, L. D. Ciaccio, M. E. Kacimi, P. Ghez, C. Girard, M. Gouanre, D. Goujdami, et al., Nucl. Instrum. Meth. A **558**, 388 (2006), ISSN 0168-9002.

[81] P. Adragna, C. Alexa, K. Anderson, A. Antonaki, A. Arabidze, L. Batkova, V. Batusov, H. P. Beck, P. Bednar, E. Bergeaas Kuutmann, et al., Nucl. Instrum. Meth. A **606**, 362 (2009).

[82] J. Pequenao (2008).

[83] G. Aad et al. (The ATLAS Collaboration), Tech. Rep. ATLAS-CONF-2011-116, CERN, Geneva (2011).

[84] S. van der Meer, *Calibration of the Effective Beam Height in the ISR: PS/6611;ISR-PO/68-31* (CERN, Geneva, 1968).

[85] M. Lamont, R. Alemany-Fernandez, H. Burkhardt, and S. White, in *Particle Accelerator Conference 2009* (Vancouver, BC, Canada, 2009), CERN-ATS-2009-071.

[86] G. Aad et al. (The ATLAS Collaboration), Eur. Phys. J. C **71**, 1630 (2011), 1101.2185.

[87] W. Lampl, S. Laplace, D. Lelas, P. Loch, H. Ma, S. Menke, S. Rajagopalan, D. Rousseau, S. Snyder, and G. Unal, Tech. Rep. ATL-LARG-PUB-2008-002. ATL-COM-LARG-2008-003, CERN, Geneva (2008).

[88] T. Cornelissen, M. Elsing, S. Fleischmann, W. Liebig, E. Moyse, and A. Salzburger, Tech. Rep. ATL-SOFT-PUB-2007-007. ATL-COM-SOFT-2007-002, CERN, Geneva (2007).

[89] R. E. Kalman, Trans. ASME J. Basic. Eng. **82**, 35 (1960).

[90] R. O. Duda and P. E. Hart, Commun. ACM **15**, 11 (1972), ISSN 0001-0782.

[91] O. Arnaez, Tech. Rep. ATL-PHYS-PROC-2009-118, CERN, Geneva (2009).

[92] G. Aad et al. (The ATLAS Collaboration), Phys. Rev. D **83**, 052005 (2011), 1012.4389.

[93] G. Aad et al. (The ATLAS Collaboration), Tech. Rep. ATL-PHYS-PUB-2011-007, CERN, Geneva (2011).

[94] G. P. Salam and G. Soyez, JHEP **0705**, 086 (2007), 0704.0292.

[95] S. D. Ellis and D. E. Soper, Phys. Rev. D **48**, 3160 (1993), hep-ph/9305266.

[96] M. Cacciari, G. P. Salam, and G. Soyez, JHEP **04**, 063 (2008), 0802.1189.

[97] G. Aad et al. (The ATLAS Collaboration), Tech. Rep. ATLAS-CONF-2011-032, CERN, Geneva (2011).

[98] G. Aad et al. (The ATLAS Collaboration), Tech. Rep. ATLAS-CONF-2011-152, CERN, Geneva (2011).

[99] G. Aad and ohters, *Expected performance of the ATLAS experiment: detector, trigger and physics* (CERN, Geneva, 2009).

[100] G. Aad et al. (The ATLAS Collaboration), Eur. Phys. J. CC **70**, 823 (2010), 1005.4568.

[101] S. Agostinelli, J. Allison, K. Amako, J. Apostolakis, H. Araujo, P. Arce, M. Asai, D. Axen, S. Banerjee, G. Barrand, et al., Nucl. Instrum. Meth. A **506**, 250 (2003), ISSN 0168-9002.

[102] T. Sjostrand, S. Mrenna, and P. Z. Skands, JHEP **0605**, 026 (2006), hep-ph/0603175.

[103] G. Corcella, I. Knowles, G. Marchesini, S. Moretti, K. Odagiri, et al. (2002), hep-ph/0210213.

[104] J. Alwall, A. Ballestrero, P. Bartalini, S. Belov, E. Boos, et al., Comput. Phys. Commun. **176**, 300 (2007), hep-ph/0609017.

[105] D. M. Gingrich, Comput. Phys. Commun. **181**, 1917 (2010), ISSN 0010-4655.

[106] T. Sjöstrand (2008), to appear in the proceedings of the HERA and the LHC workshop, 26–30 May 2008, CERN, 0809.0303.

[107] I. Antcheva, M. Ballintijn, B. Bellenot, M. Biskup, 1, R. Brun, N. Buncic, P. Canal, D. Casadei, O. Couet, V. Fine, et al., Comput. Phys. Commun. **180**, 2499 (2009).

[108] A. Sherstnev and R. Thorne, Eur. Phys. J. C **55**, 553 (2008), 0711.2473.

[109] M. L. Mangano, M. Moretti, F. Piccinini, R. Pittau, and A. D. Polosa, JHEP **0307**, 001 (2003), hep-ph/0206293.

[110] J. M. Butterworth, J. R. Forshaw, and M. H. Seymour, Z. Phys. C Part. Fields. **72**, 637 (1996), hep-ph/9601371.

[111] S. Frixione and B. R. Webber, JHEP **06**, 029 (2002), hep-ph/0204244.

[112] S. Frixione and B. R. Webber (2008), 0812.0770.

[113] S. Frixione, E. Laenen, P. Motylinski, and B. R. Webber, JHEP **03**, 092 (2006), hep-ph/0512250.

[114] V. Dao et al. (The ATLAS Collaboration), JPCS **293**, 012027 (2011).

[115] G. Aad et al. (The ATLAS Collaboration), Eur. Phys. J. C **72**, 1909 (2012), 1110.3174.

[116] A. Ahmad, M. Boonekamp, et al. (The ATLAS Collaboration), Tech. Rep. ATL-COM-PHYS-2011-1637, CERN, Geneva (2011).

[117] P. R. Bevington and D. K. Robinson, *Data reduction and error analysis for the physical sciences* (McGraw-Hill, 1992).

[118] G. Aad et al. (The ATLAS Collaboration) (2011), submitted to European Physical Journal C, 1112.6426.

[119] A. L. Read, J. Phys. G Nucl. Partic. **28**, 2693 (2002).